Fundamental Aspects Of Unconfined Explosions

J. A. Nicholls

M. Sichel

R. S. Fry

C. Hu

D. R. Glass

R. De Saro

K. Kearney

FOREWORD

This report covers the progress made during the second year of a research program conducted by the Department of Aerospace Engineering, The University of Michigan, Ann Arbor, Michigan under Contract F08635-71-C-0083 with the Air Force Armament Laboratory, Eglin Air Force Base, Florida. Lieutenant Richard E. Swanson and Captain Harold F. Klaus (DLIF) served as project managers for the Armament Laboratory. The research was directed by Professor J.A. Nicholls. This effort was conducted during the period from January 22, 1972 to January 21, 1973.

This technical report has been reviewed and is approved

F. RAMON BONANNO, Lt Colonel, USAF
Acting Chief, Flame, Incendiary and Explosives Division

ABSTRACT

This report covers progress made in the second year of the research program. The first part of the report is devoted to a generalized analytical prediction of the ground impulse that can be obtained from a blast wave, detonation wave, and an idealized fuel-air explosion. The latter consists of blast wave behavior for radius, r, less than a critical radius, r*, and Chapman-Jouguet detonation for r > r*. In all cases so far, the finite diameter of the cloud with the attendant shock wave propagation beyond the cloud has not been taken into account. The latter part of this report is devoted to the experimental aspects. Improvements in the facility for generating cylindrical shock waves and detonation waves are described. Controlled experiments on cylindrical blast waves with the associated data reduction techniques are discussed. The results are interpreted to yield a calibration on the effective energy release of the initiating charge of Detasheet. Two phase cylindrical detonation experiments were also conducted using a highly refined fraction of kerosene. The results indicate that at small radius blast wave behavior predominated whereas at larger radius a constant velocity detonation was realized when the initiation energy was sufficiently high. The experimentally determined transition radius between the two types of behavior agreed very well with theoretical values. Cylindrical detonations in gaseous MAPP-air mixtures were also studied. The variation in threshold energy required for initiation as well as rich and lean limits were established. The results agree very well with large scale field tests.

(The reverse of this page is blank)

TABLE OF CONTENTS

LIST OF FIGURES

LIST OF FIGURES (CONCLUDED)

LIST OF TABLES

NOMENCLATURE

a	local acoustic speed
C	detonation wave velocity
E	energy release
E_0	total instantaneous energy release per unit area or per unit length respectively for planar or cylindrical blast wave geometry
$\bar{I}$	total impulse imparted to ground
M	Mach number
	molecular weight
p	pressure
P	dimensionless pressure
P_b	universal pressure function
Q	heat release per unit mass of mixture due to chemical reaction
r	linear spatial coordinate-radius
R	dimensionless density, or radius
R	universal gas constant
t	time referenced from the origin on the cylindrical model
T	temperature
T	time
u	fluid velocity
v	fluid velocity
V	dimensionless fluid velocity
z	ratio of dimensionless pressure to dimensionless density

α	blast wave parameter
β	blast wave impulse function
γ	ratio of specific heats
δ	detonation impulse function
η_e	energy efficiency factor
ϵ	error function
λ	dimensionless independent similarity variable
ν	geometric constant equal to 1, 2 or 3 for plane, cylindrical or spherical cloud geometry
ϕ	equivalence ratio
ρ	density
σ_ν	geometric cloud factor

Subscripts

0	stagnation
0	reference
1	static
1	upstream of incident shock
2	downstream of incident shock
3	downstream of C-J plane
BW	blast wave
calc	calculated

CJ	Chapman-Jouguet plane
crit	critical
D	detonation
i	data point $i = 1, 2, 3 \ldots n$
reg	regression
s	shock
s	spherical detonation
th	theoretical
*	critical

SECTION I

INTRODUCTION

The aim of this research program is to gain a better understanding of the unconfined explosion of detonatable clouds. Particular attention is given to the liquid fuel-air explosion. An analytical model of such explosions which would be capable of predicting the pressure and velocity field, impulses generated, and desirable characteristics of the fuel has not been available. Accordingly, one phase of this research has been directed to gaining such an understanding. The progress on this phase is described in the next section.

On the experimental side, controlled studies of cylindrical and/or spherical heterogeneous detonations had not been conducted. Thus, the second phase of this research is concerned with experimental studies on a laboratory model of a fuel-air explosion. This work is described in Section III.

SECTION II
THE GROUND IMPULSE FROM BLAST WAVES, DETONATIONS, AND AN IDEAL FUEL-AIR EXPLOSION

A. INTRODUCTION

In the establishment of a fuel-air explosion (FAE), liquid fuel in an appropriate container is dispersed into the atmosphere as a cloud of fine droplets by the detonation of a primary charge. An appropriately placed and timed secondary explosion is then used to detonate this cloud of fuel droplets. Methods of computing the ground impulse generated by an idealized model of such a FAE are developed in this report.

The shape of the fuel cloud and the distribution of fuel within it which, in turn, will have an important effect on the ground impulse, will generally be quite complex and depend upon the method of fuel dispersal. Here an idealized FAE with cylindrical symmetry and a uniform distribution of fuel is considered. A cylindrical blast wave initiated at the center of the cloud sets off the detonation. This idealized model provides a starting point for the consideration of other FAE phenomena.

At first the idealized FAE behaves like a strong cylindrical blast wave but later the behavior approaches that of a cylindrical Chapman-Jouguet (C-J) detonation. Universal formulas for computing the total ground impulse generated by blast waves and C-J waves are first developed below. Then it is shown how these relations can be combined to compute the ground impulse generated by an ideal FAE. Details of the computations are presented in Appendix I.

2

B. IDEALIZED MODEL OF THE FAE

The model of the FAE considered here consists of a cloud of uniformly distributed fuel droplets or gaseous fuel adjacent to the ground plane, and of sufficient height so that the effect of side relief can be neglected. The secondary blast is initiated by the instantaneous release of explosive along the axis of symmetry of the FAE. The secondary blast wave and the subsequent C-J detonation will thus be cylindrical and will propagate radially outward from the axis of symmetry. The idealized FAE is shown in Figure 1 and is equivalent to a cylindrical FAE of finite height but confined between two non-yielding parallel surfaces. It has been possible to simulate such an idealized FAE in the laboratory (Nicholls et al.[1]).

Blast initiation of a detonation, which corresponds to the initial phase of a FAE, has been considered by Korobeinikov[2] and Bach et al.[3] among others. Initially the flow is dominated by the strong secondary blast wave while the energy released by combustion has a negligible effect. The blast wave decays rapidly, and if the blast energy is large enough, a C-J detonation is established. This transition from blast wave to detonation occurs in the neighborhood of the radius r_* where the blast energy E_o is equal to the combustion energy release within r_*, i.e., in the region $r < r_*$. The radius r_* plays a key role in the blast initiation of detonations and is sometimes referred to as the critical blast wave radius.
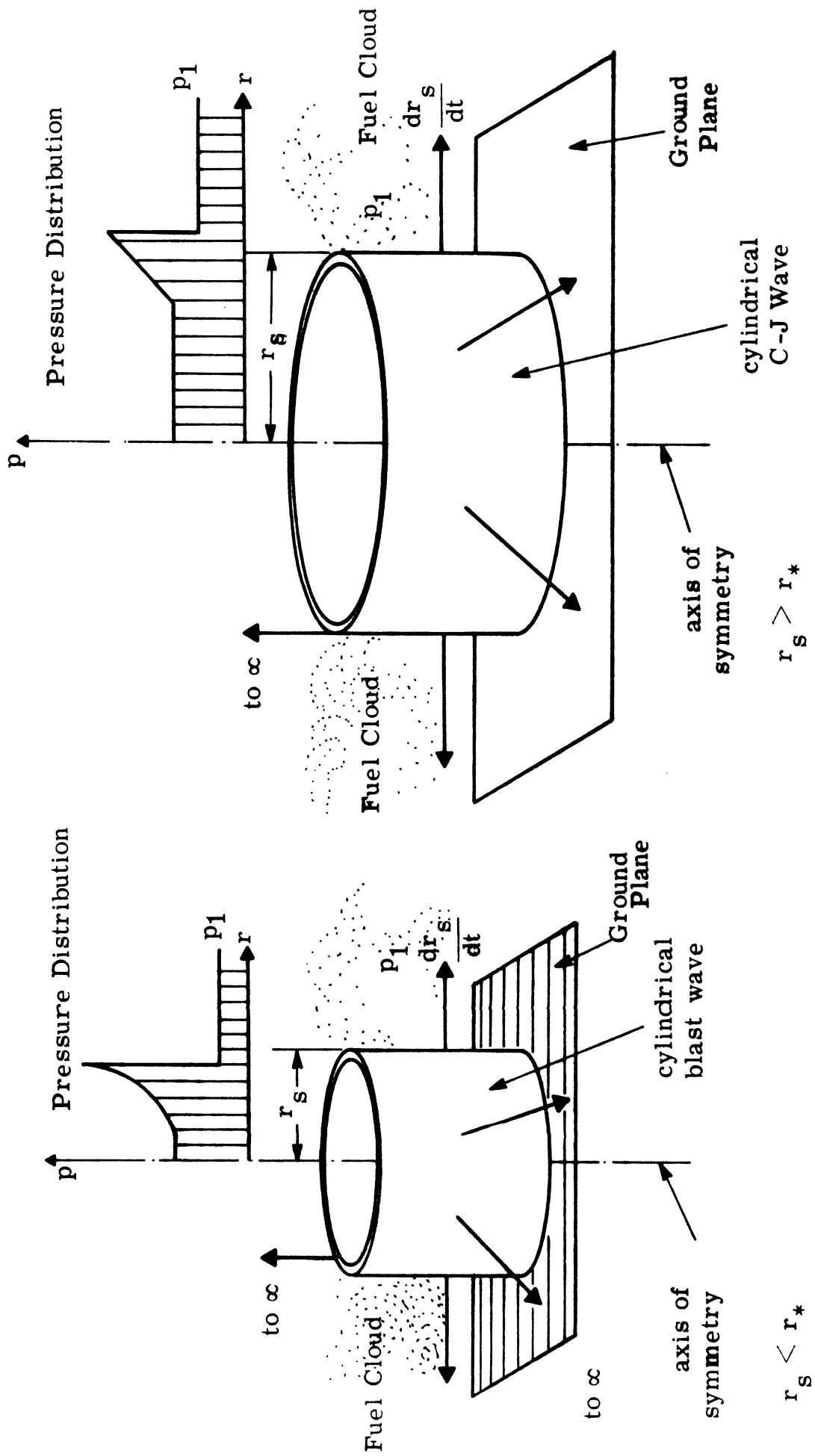
Figure 1. Idealized Fuel-Air Explosion

4

If Q is the combustion energy released in the fuel cloud per unit mass of mixture and if E_o is the secondary blast energy released per unit length on the axis of symmetry, then r_* will be defined by the relation

$$E_o = \pi \, r_*^2 \, \rho_1 \, Q \tag{1}$$

where ρ_1 is the initial density of the fuel cloud. Thus

$$r_* = \left(\frac{E_o}{\pi \, \rho_1 \, Q}\right)^{1/2} \tag{2}$$

for a cylindrical wave. In general, with $\nu = 1$, 2, and 3 for plane, cylindrical, and spherical symmetry

$$r_* = \left(\nu \, E_o / \sigma_\nu \, Q \, \rho_1\right)^{1/\nu} \tag{3}$$

E_o is now the blast energy released per unit area, length, or the total energy released at a point in the spherical $\nu = 3$ case. The geometric factor σ_ν is given by

$$\sigma_\nu = 2(\nu - 1) \, \pi + (\nu - 2)(\nu - 3)$$

and $\sigma_\nu = 2$, 2π, 4π for $\nu = 1$, 2, 3.

Initially when $r_s \ll r_*$, where r_s is the radius of the outward propagating blast or detonation, the FAE is essentially a strong blast wave and can be described by the self-similar solution of Sedov[4] and Taylor[5]. When $r_s \gg r_*$ the FAE becomes a C-J wave which can also be described

5

by a self-similar solution of the conservation equations. In the transitional region $r_s \sim r_*$ neither the blast wave or the C-J similarity solutions will be valid. A semi-empirical theory for flow in this transitional region has been developed by Bach et al[3].

In the idealized model of the FAE the complications which arise in the transitional region are ignored by assuming that the FAE can be described by the self-similar strong blast wave solution when $r_s < r_*$ and by the self-similar solution for a C-J detonation when $r_s > r_*$. This approximation is a key feature of the idealized FAE and leads to great simplification. Experiments[1] indicate that the transition from blast to detonative behavior occurs very rapidly near $r_s \sim r_*$. Thus, neglect of the details of the transition should result in only minor errors in the determination of FAE propagation and impulse.

It can be seen from Equations (2) and (3) that the critical blast wave radius r_* depends on both the secondary blast energy E_0 and the heat release Q of the fuel. Unless E_0 exceeds a certain minimum initiation energy $(E_0)_{crit}$, the secondary blast will decay to an acoustic wave and the fuel cloud will fail to detonate. As indicated in Reference 1, $(E_0)_{crit}$ will depend upon the structure of the detonation wave, and with the present state of knowledge actual values of $(E_0)_{crit}$ can only be determined experimentally. In an actual FAE device $E_0 > (E_0)_{crit}$ in general. Precise determination of Q requires detailed calculation of the equilibrium

composition of the combustion products behind the C-J detonation.

However, as shown in Reference 1, remarkably accurate results can be

obtained for the jump condition across detonations if the perfect gas

equation is used both upstream and downstream of the C-J discontinuity

with, however, different values of molecular weight and the ratio of

specific heats. Then

$$Q \cong \frac{C^2}{2(\gamma_2^2 - 1)} \tag{4}$$

where C is the velocity of propagation and γ_2 is the ratio of specific heats

of the combustion products. With Equation (4) the expression for r_* can also

be written in the form

$$r_* = \left[\frac{2\nu E_0 (\gamma_2^2 - 1)}{\sigma_\nu \rho C^2} \right]^{1/\nu} \tag{5}$$

The self-similar blast wave and C-J solutions are patched together

when $r_s = r_*$ in the idealized FAE model described above. This means

that the entire flow field $r < r_s$ corresponds to that of a blast wave when

$r_s < r_*$ and to that of a C-J detonation when $r_s > r_*$. The pressures

p_2 behind the blast wave and p_{CJ} behind a C-J detonation are not equal

at the point of transition $r_s = r_*$ but are of the same order of magnitude.

From the simple theory for C-J detonations

7

$$\frac{p_{CJ}}{p_1} \cong 2\gamma_1 \left(\frac{\gamma_2 - 1}{\gamma_1 - 1}\right) \frac{Q}{C_{p_1} T_1} \tag{6}$$

i. e., p_{CJ} is independent of radius and depends only on the fuel and the properties of the unburned and burned gases. The blast wave pressure p_2 decreases with increasing shock radius r_s and from the self-similar blast wave theory[1] is given by

$$p_2 = \frac{8\rho_1}{(\nu + 2)(\gamma_1 + 1)} \left[\frac{E_o}{\rho_1 \alpha(\gamma, \nu)}\right] r_s^{-\nu} \tag{7}$$

The parameter $\alpha(\gamma, \nu)$ is a function of γ and ν and is plotted in Figure 2. Letting p^* be the value of p_2 corresponding to $r_s = r_*$ and introducing the expression (3) for r_* in Equation (7) then yields

$$\frac{p_2^*}{p_{CJ}} = \frac{4\sigma_\nu}{(\nu + 2)\nu \, \alpha(\gamma_1 + 1)(\gamma_2 - 1)} \tag{8}$$

Taking $\gamma_1 = 1.4$, $\gamma_2 = 1.2$, $\alpha = 1.0$, Equation (8) yields the following result

ν	1	2	3
p_2^*/p_{CJ}	1.85	1.64	1.39

so that the blast and C-J pressures are indeed of the same order of magnitude when $r_s = r_*$.

In order to determine the ground impulse generated by an ideal FAE, it is necessary to determine the ground impulse of a strong blast wave and of a C-J wave as described below.

8
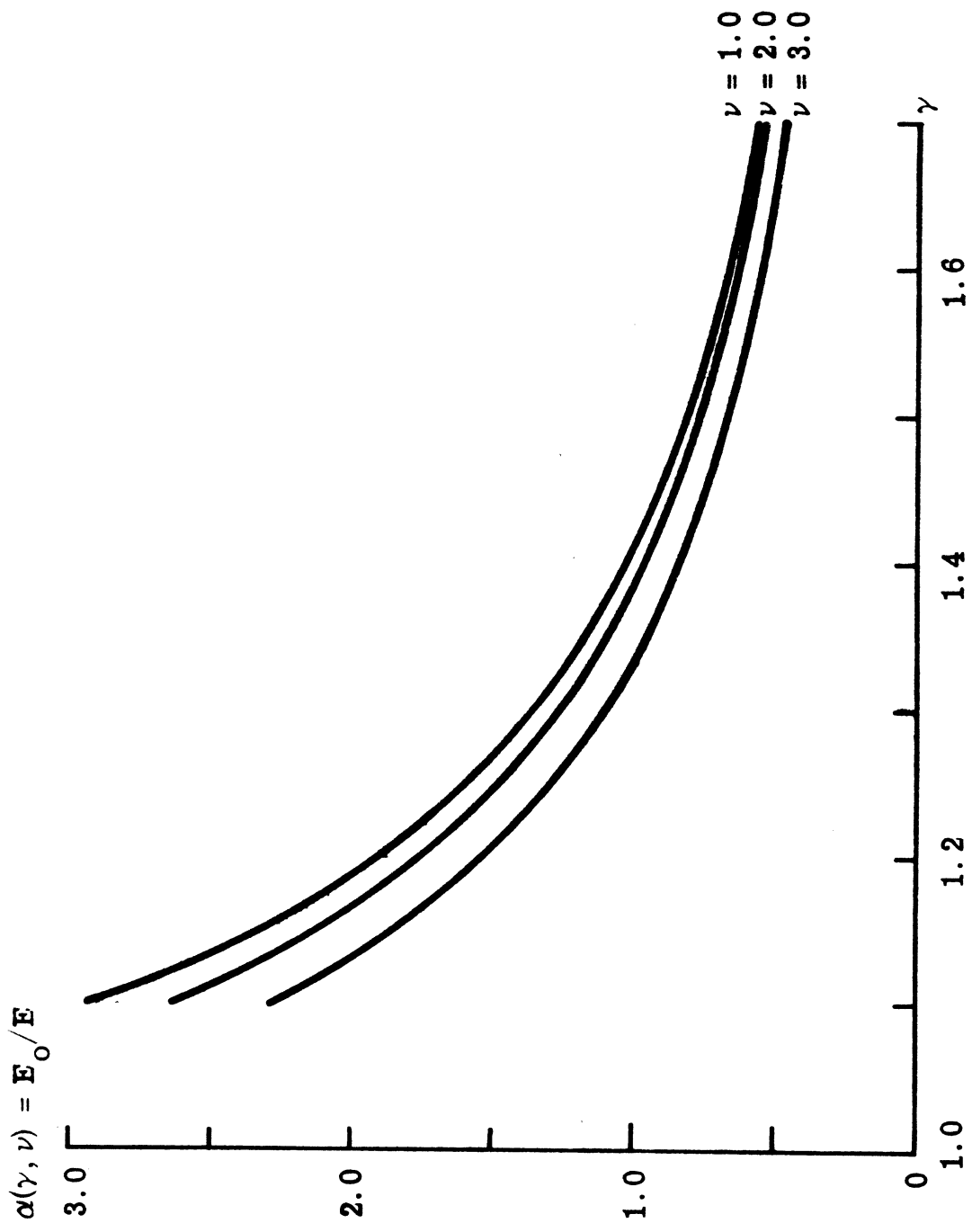
Figure 2. Variation of the Blast Wave Parameter $\alpha(\gamma, \nu)$ with γ

C. TOTAL GROUND IMPULSE

1. Integral for the Impulse

The pressure, p, within the leading shock of a FAE, i.e., in the region $r < r_s$ will be a function of the radial distance r from the blast center and of time t. If p_1 is the ambient pressure ahead of the FAE, then the ground impulse generated by the FAE per unit area at a given point during time interval dt is $(p - p_1)$ dt. The total impulse in the region $r < r_s$ generated during interval dt is given by the integral

$$\left\{ \int_0^{r_s(t)} \left[p(r,t) - p_1 \right] 2\pi r \, dr \right\} dt$$

The upper limit r_s is, as indicated, a function of time. Finally, the total ground impulse, $\bar{I}(t)$, at time t after the initiation of the secondary blast on the axis of symmetry will be

$$\bar{I}(t) = 2\pi \int_0^t \int_0^{r_s(t)} \left[p(r,t) - p_1 \right] r \, dr \, dt \tag{9}$$

It is often also of interest to determine the ground impulse generated by a planar and spherical wave. In the planar case the secondary blast is initiated on the plane $r = 0$ where now r is the distance from blast center. In the planar case, $\nu = 1$, r is a Cartesian Coordinate and can have positive and negative values. As shown in Figure 3, two planar blast

10

Figure 3. Planar FAE

11

or detonation waves then propagate symmetrically in both the + r and - r directions. The planar configuration is typical of that encountered in various bag tests. The total ground impulse generated by a planar wave is given by

$$\bar{I}(t) = 2 \int_0^t \int_0^{r_s(t)} \left[p(r, t) - p_1 \right] dr \, dt \tag{10}$$

The factor of 2 in Equation (10) accounts for the propagation in the + and - r directions.

The pressure generated by a spherical wave with the secondary blast initiated at a point on the ground plane (as shown in Figure 4) still acts on a circular area so that the impulse is still given by Equation (9). Now, however $p(r, t)$ and $r_s(t)$ correspond to a spherical wave.

In general, evaluation of the impulse from Equations (9) and (10) will require extensive numerical computation. However, in the case of strong blast waves and C-J detonations, the integrals (9) and (10) can be reduced to simple expressions for the impulse $\bar{I}(t)$ as shown below.

2. Ground Impulse for a Strong Blast Wave

A detailed discussion of the self-similar solution for a strong blast wave is given in Reference 1. For a strong blast wave the ambient pressure $p_1 \ll p$, and so can be neglected. The pressure p depends on the dimensionless radius $\lambda = r/r_s$ according to
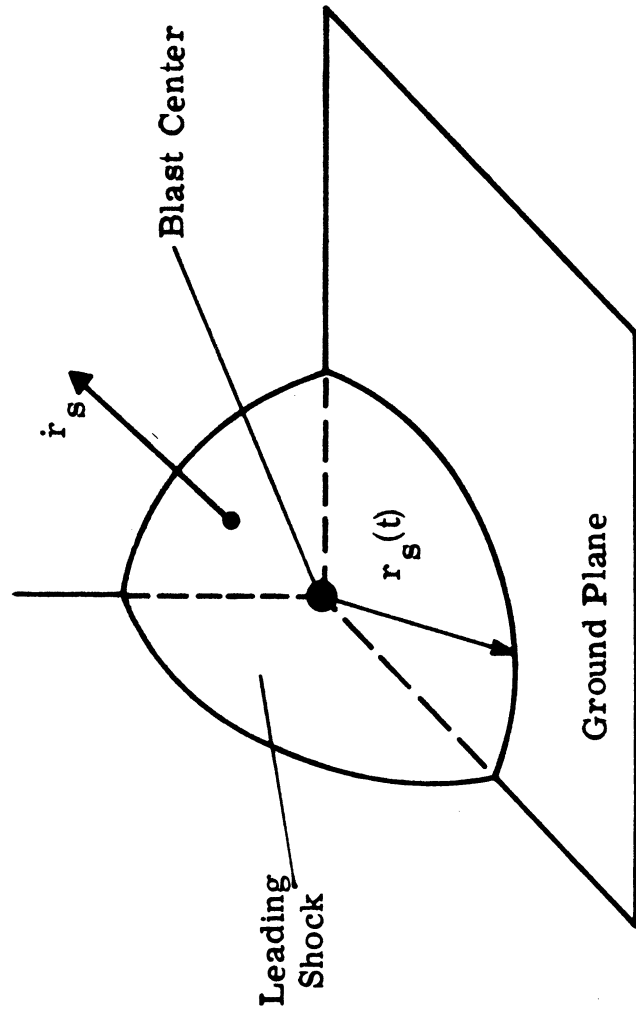
Figure 4. Spherical FAE—Quarter View

13

$$p = \rho_1 \left(\frac{r^2}{t^2} \right) P_b(\lambda, \nu) \tag{11}$$

$P_b(\lambda, \nu)$ is a universal function of λ which depends only on the ratio of

specific heats γ, and on the geometry of the wave, i.e., on ν. The radius

$r_s(t)$ of the shock front is given by

$$r_s(t) = \left[\frac{E_o}{\rho_1 \, \alpha \, (\gamma, \nu)} \right]^{\frac{1}{\nu+2}} t^{\frac{2}{\nu+2}} \qquad \nu = 1, 2, 3 \tag{12}$$

The function $\alpha(\gamma, \nu)$, which also occurs in Equation (7) for p_2, is shown

in Figure 2.

Neglecting p_1 and introducing the variables λ and P the inner inte-

gral in Equations (9) and (10) becomes

$$\sigma_\nu \int_0^{r_s} p \, r^{\nu-1} \, dr = \sigma_\nu \int_0^1 \rho_1 \frac{r_s^2 \lambda^2}{t^2} P_b(\lambda, \nu)(r_s\lambda)^{\nu-1} r_s \, d\lambda \tag{13}$$

where Equation (13) reduces to the planar and cylindrical forms for $\nu = 1, 2$.

Upon introducing Equation (12) for $r_s(t)$, Equation (13) becomes

$$\sigma_\nu \int_0^{r_s} p \, r^{\nu-1} \, dr = \frac{E_o}{\alpha(\gamma, \nu)} \sigma_\nu \int_0^1 P_b(\lambda, \nu) \, \lambda^{\nu+1} \, d\lambda \tag{14}$$

The integral in Equation (14) is a universal function of γ and ν and

can be evaluated from the blast wave solution, as shown in Appendix I.

Integration with respect to time t now yields the following result for

blast wave ground impulse

$$\bar{I}(t) = \sigma_\nu \, E_0 \, \frac{\beta(\gamma, \nu)}{\alpha(\gamma, \nu)} \, t \quad ; \quad \nu = 1, 2 \tag{15}$$

$$\beta(\gamma, \nu) = \int_0^1 P_b(\lambda, \nu) \, \lambda^{\nu+1} \, d\lambda$$

For planar and cylindrical blast waves the ground impulse thus varies

linearly with time and is proportional to the blast energy. The universal

function $\beta(\gamma, \nu)$ is plotted in Figure 5, while Figure 6 shows the varia-

tion of $\sigma_\nu \beta / \alpha$ which is equivalent to a dimensionless impulse $\bar{I}(t) / E_0 t$.

In the planar, $\nu = 1$, case $\bar{I}(t)$ is the impulse on a strip of ground of

unit width. The values of $\alpha(\gamma, \nu)$, $\beta(\gamma, \nu)$, and $\sigma_\nu \beta / \alpha$ are tabulated in

Table I.

For a spherical blast wave which, however, acts on a circular

region of the ground as shown in Figure 4, the results are somewhat

different. Equation (11) relation p to $P_b(\lambda, \nu)$ remains valid. Now,

however, the inner integral of Equation (9) becomes

$$2\pi \int_0^{r_s(t)} pr \, dr = 2\pi \int_0^1 \rho_1 \frac{r_s^2 \lambda^2}{t^2} P_b(\lambda, 3) \, r_s \lambda \, r_s \, d\lambda \tag{16}$$

15
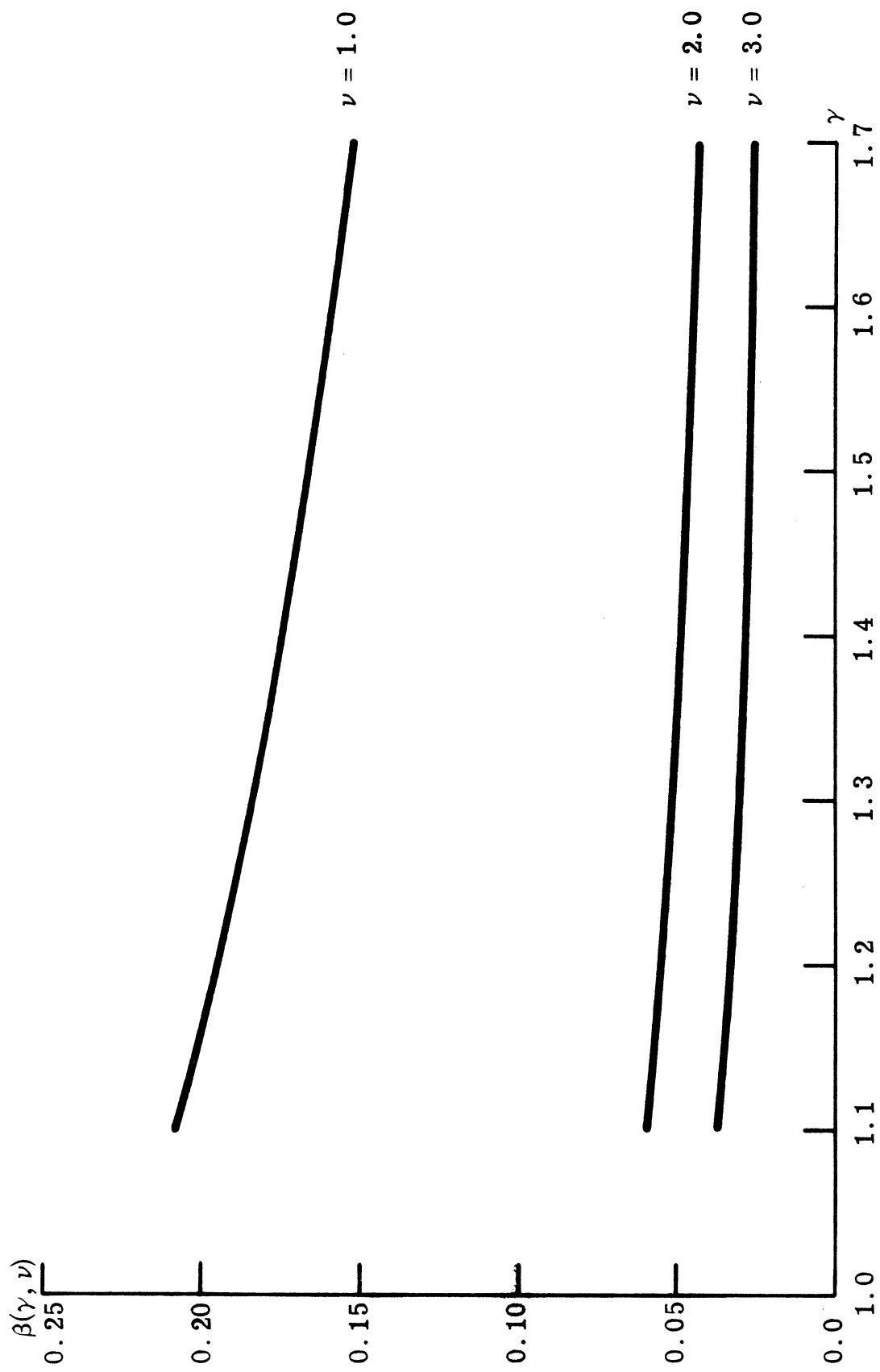
Figure 5. Variation of the Blast Wave Impulse Function $\beta(\gamma, \nu)$ with ν and γ

$\nu = 1.0$
$\nu = 2.0$
$\nu = 3.0$

$$\nu = 3.0 \quad \frac{\overline{I}(t)}{t^{3/5} \, p_1(E_o/\rho_1)^{4/5}} = \frac{10}{3} \, \pi \, \frac{\beta(\gamma, \nu)}{\alpha(\gamma, \nu)^{4/5}}$$

$$\nu = 2.0 \quad \frac{\overline{I}(t)}{E_o t} = \sigma_\nu \frac{\beta(\gamma, \nu)}{\alpha(\gamma, \nu)}$$

$$\nu = 1.0 \quad \frac{\overline{I}(t)}{E_o t} = \sigma_\nu \frac{\beta(\gamma, \nu)}{\alpha(\gamma, \nu)}$$
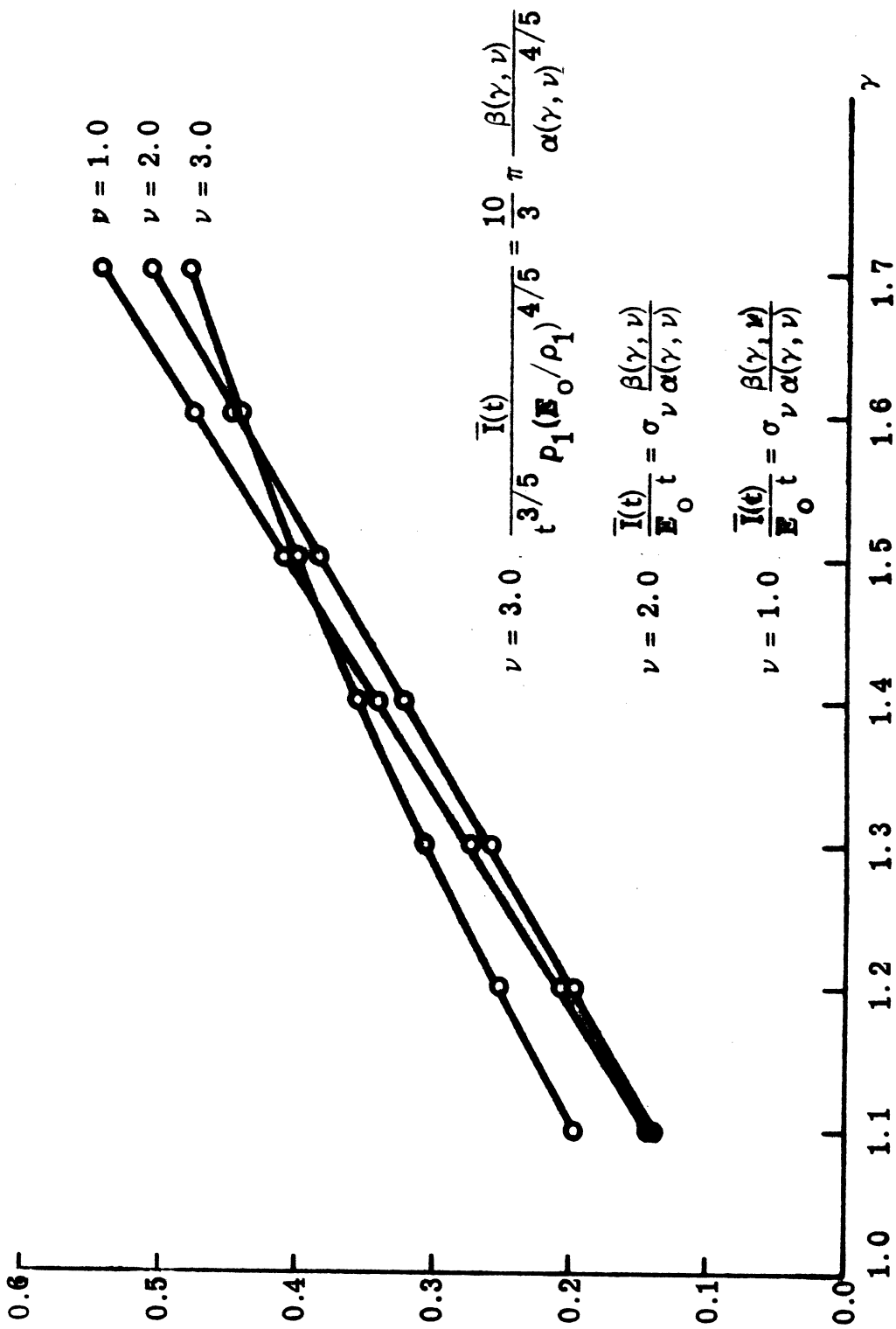
Figure 6. Variation of the Blast Wave Impulse Functions

17

TABLE I. BLAST WAVE

(a) Values of $\alpha(\gamma, \nu)$			
γ	$\nu = 1.0$	$\nu = 2.0$	$\nu = 3.0$
1.1	2.9383	2.6449	2.2997
1.2	1.9114	1.7622	1.5383
1.3	1.3620	1.2661	1.1005
1.4	1.0264	0.9666	0.8428
1.5	0.8163	0.7711	0.6743
1.6	0.6695	0.6346	0.5572
1.7	0.5619	0.5356	0.4716

(b) Values of $\beta(\gamma, \nu)$			
γ	$\nu = 1.0$	$\nu = 2.0$	$\nu = 3.0$
1.1	0.20822	0.05857	0.03669
1.2	0.19613	0.05521	0.03397
1.3	0.18557	0.05230	0.03169
1.4	0.17621	0.04972	0.02973
1.5	0.16784	0.04743	0.02803
1.6	0.16028	0.04536	0.02654
1.7	0.154342	0.04349	0.02522

(c) Values of Dimensionless Impulse Function vs γ			
	$\sigma_\nu \dfrac{\beta(\gamma)}{\alpha(\gamma)}$		$\dfrac{10}{3}\pi \dfrac{\beta(\gamma)}{\alpha(\gamma)^{4/5}}$
γ	$\nu = 1.0$	$\nu = 2.0$	$\nu = 3.0$
1.1	0.14173	0.13914	0.197348
1.2	0.20523	0.19687	0.252606
1.3	0.27250	0.25954	0.307340
1.4	0.34336	0.32322	0.356979
1.5	0.41121	0.38644	0.402344
1.6	0.47884	0.44916	0.443792
1.7	0.54611	0.51020	0.481910

Now, however

$$r_s(t) = \left[\frac{E_o}{\rho_1 \alpha}\right]^{1/5} t^{2/5}$$

so that Equation (16) becomes

$$2\pi \int_0^{r_s(t)} pr \, dr = 2\pi \rho_1 \left(\frac{E_o}{\rho_1 \alpha}\right)^{4/5} t^{-2/5} \int_0^1 P_b(\lambda, 3) \lambda^3 \, d\lambda \qquad (16a)$$

After integration with respect to time the spherical blast wave ground impulse becomes

$$\overline{I}(t) = \frac{10}{3} \pi \rho_1 (E_o/\alpha\rho_1)^{4/5} \beta(\gamma, 3) t^{3/5} \qquad (17)$$

where $\beta(\gamma, 3)$ is again defined by Equation (15), but now $P_b(\lambda, 3)$ corresponds to the spherical blast wave solution. The function $\beta(\gamma, \nu)$ for $\nu = 3$ and the normalized impulse

$$\frac{\overline{I}(t)}{t^{3/5} \rho_1 (E_o/\rho_1)^{4/5}} = \frac{10}{3} \pi \frac{\beta(\gamma, 3)}{\left[\alpha(\gamma, 3)\right]^{4/5}} \qquad (18)$$

are plotted in Figures 5 and 6.

Using Equation (12) for $r_s(t)$ the formulas for $\overline{I}(t)$ may also be expressed in terms of the blast radius r_s, a form more useful in certain applications. Thus, for $\nu = 1, 2$

19

$$\overline{I}(r_s) = \sigma_\nu \left(\frac{E_o \, \rho_1}{\alpha}\right)^{1/2} \beta(\gamma, \nu) \; r_s^{\nu+2/2} \tag{19}$$

while for the spherical case $\nu = 3$

$$\overline{I}(r_s) = \frac{10}{3} \, \pi \, \rho_1 \left(\frac{E_o}{\alpha \rho_1}\right)^{1/2} \beta(\gamma, 3) \; r_s^{3/2} \tag{20}$$

The above relations for computing blast wave ground impulse are summarized in Table II below.

TABLE II. RELATIONS FOR COMPUTING BLAST WAVE GROUND IMPULSE

ν	$\overline{I}(t)$	$\overline{I}(r_s)$
1	$2E_o \dfrac{\beta}{\alpha} t$	$2\left(\dfrac{E_o \, \rho_1}{\alpha}\right)^{1/2} \beta \, r_s^{3/2}$
2	$2\pi \, E_o \dfrac{\beta}{\alpha} t$	$2\pi \left(\dfrac{E_o \, \rho_1}{\alpha}\right)^{1/2} \beta \, r_s^{2}$
3	$\dfrac{10}{3} \, \pi \, \rho_1 \left(\dfrac{E_o}{\rho_1 \alpha}\right)^{4/5} \beta \, t^{3/2}$	$\dfrac{10}{3} \, \pi \left(\dfrac{E_o \, \rho_1}{\alpha}\right)^{1/2} \beta \, r_s^{3/2}$

Knowing α and β from Figures 2 and 5, $\overline{I}(t)$ and $\overline{I}(r_s)$ can now be readily calculated for any E_o and ρ_1.

3. Ground Impulse from a Chapman-Jouguet Detonation

The ground impulse generated by a C-J detonation is also given by Equations (9) and (10). Now, however, the ambient pressure p_1 is no longer negligible compared to the pressure behind the detonation front. The self similar solution for a C-J detonation, which is discussed in detail in Reference 1 can be used to reduce the impulse integral [(Equations (9) and(10))] to a relatively simple form.

As before, a dimensionless pressure $P_d(\lambda, \nu)$ is defined by

$$p = \rho_1 \frac{r^2}{t^2} P_d (\lambda, \nu) \tag{11}$$

where
$$\lambda = r/r_s$$

In contrast to the blast wave, a detonation front propagates with a constant velocity C so that

$$r_s = Ct \tag{21}$$

Introducing the similarity variables the inner integral in Equations (9) and (10) becomes

$$\sigma_\nu \int_0^{r_s} (p - p_1) \, r^{\nu-1} \, dr$$

$$= \sigma_\nu \, \rho_1 \, C^{\nu+2} \, t^\nu \left[\int_0^1 P_d(\lambda, \nu) \, \lambda^{\nu+1} \, d\lambda - \frac{p_1}{\rho_1 \, C^2 \, \nu} \right] \quad , \quad \nu = 1, 2 \qquad (22)$$

The Mach number, M_D of the detonation is given by

$$M_D = \frac{C}{\sqrt{\gamma_1 \, (p_1/\rho_1)}}$$

where γ_1 is the ratio of specific heats of the unburned fuel. Hence, the ground impulse $\bar{I}(t)$ will be given by

$$\bar{I}(t) = \frac{\sigma_\nu \, \rho_1 \, C^{\nu+2} \, t^{\nu+1}}{\nu + 1} \left[\int_0^1 P_d(\lambda, \nu) \, \lambda^{\nu+1} \, d\lambda - \frac{1}{\nu \, \gamma_1 \, M_D^2} \right], \quad \nu = 1, 2 \qquad (23)$$

For a spherical detonation the ground impulse is given by

$$\bar{I}(t) = \frac{2\pi \, \rho_1 \, C^4 \, t^3}{3} \left[\int_0^1 P_d(\lambda, 3) \, \lambda^3 \, d\lambda - \frac{1}{2\gamma_1 \, M_D^2} \right] \qquad (24)$$

The integral which appears in Equations (22) and (23), and which is denoted by

22

$$\delta(\gamma_2, \nu) = \int_0^1 P_d(\lambda, \nu) \, \lambda^{\nu+1} \, d\lambda \qquad \nu = 1, 2$$

(25)

$$\delta(\gamma_2, 3) = \int_0^1 P_d(\lambda, 3) \, \lambda^3 \, d\lambda \qquad \nu = 3$$

depends upon the ratio of specific heats, γ_2, of the combustion products, upon the geometry of the detonation, and, weakly, upon the detonation Mach number, M_D. The computation of $\delta(\gamma_2, \nu)$ is discussed in detail in Appendix II.

The ground impulse also can be expressed as a function of the detonation radius r_s so that

$$\bar{I}(r_s) = \frac{\sigma_\nu \, \rho_1 \, C \, r_s^{\nu+1}}{\nu + 1} \left[\delta(\gamma_2, \nu) - \frac{1}{\nu \, \gamma_1 \, M_D^2} \right] \qquad \nu = 1, 2$$

(26)

and for spherical waves

$$\bar{I}(r_s) = \frac{2\pi \, \rho_1 \, C \, r_s^3}{3} \left[\delta(\gamma_2, 3) - \frac{1}{2\gamma_1 \, M_D^2} \right] \qquad \nu = 3$$

(27)

The expressions for the ground impulse generated by a C-J detonation are summarized in Table III.

The detonation velocity C, Mach number, M_D, ratio of specific heats γ_2, and the jump in pressure, density, and temperature across the detonation are required in order to compute $\delta(\gamma_2, \nu)$ and the ground

23

TABLE III. RELATIONS FOR COMPUTING CHAPMAN-JOUGUET WAVE GROUND IMPULSE

ν	$\bar{I}(t)$	$\bar{I}(r_s)$
1	$\rho_1 C^3 t^2 \left[\delta(\gamma_2, 1) - \dfrac{1}{\gamma_1 M_D^2} \right]$	$\rho_1 C r_s^2 \left[\delta(\gamma_2, 1) - \dfrac{1}{\gamma_1 M_D^2} \right]$
2	$\dfrac{2\pi \rho_1 C^4 t^3}{3} \left[\delta(\gamma_2, 2) - \dfrac{1}{2\gamma_1 M_D^2} \right]$	$\dfrac{2\pi \rho_1 C r_s^3}{3} \left[\delta(\gamma_2, 2) - \dfrac{1}{2\gamma_1 M_D^2} \right]$
3	$\dfrac{2\pi \rho_1 C^4 t^3}{3} \left[\delta(\gamma_2, 3) - \dfrac{1}{2\gamma_1 M_D^2} \right]$	$\dfrac{2\pi \rho_1 C r_s^3}{3} \left[\delta(\gamma_2, 3) - \dfrac{1}{2\gamma_1 M_D^2} \right]$

impulse $\bar{I}(t)$ or $\bar{I}(r_s)$ from the above relations. In other words, the Chapman-Jouguet conditions must be computed and, of course, vary with the fuel used and with the mixture ratio. Precise determination of the C-J conditions is tedious since the equilibrium composition of the combustion products must be determined. Fortunately Gordon and McBride[6] have developed a very efficient computer program for making such calculations, and this program has been used to determine the C-J conditions for gaseous air-MAPP and air-methane mixtures as outlined in Appendix III. These two fuel-air mixtures have been chosen as representative of the hydrocarbon fuel-air mixtures which might be used in FAE's. The detonation parameters for methane and MAPP-air mixtures are shown in Figures 7 and 8 and tabulated in Table IV.

The function $\delta(\gamma_2, \nu)$ has been calculated for both air-methane and air-MAPP mixtures. For the two fuels considered, γ_2 ranges between 1.16 and 1.31 while M_D is between 4.0 and 5.0, and over this range $\delta(\gamma_2, \nu)$ is almost independent of γ_2 and the mixture ratio ϕ. In fact, $\delta(\gamma_2, \nu)$ depends only on ν for CH_4 and MAPP, and the average value of $\delta(\gamma_2, \nu)$ is given in Table V below. The values of γ_2 and M_D are typical of most hydrocarbon air C-J detonations; hence, the values of $\delta(\gamma_2, \nu)$ in Table V can be used to compute the impulse for hydrocarbon-air C-J detonations, in general, with reasonable accuracy.
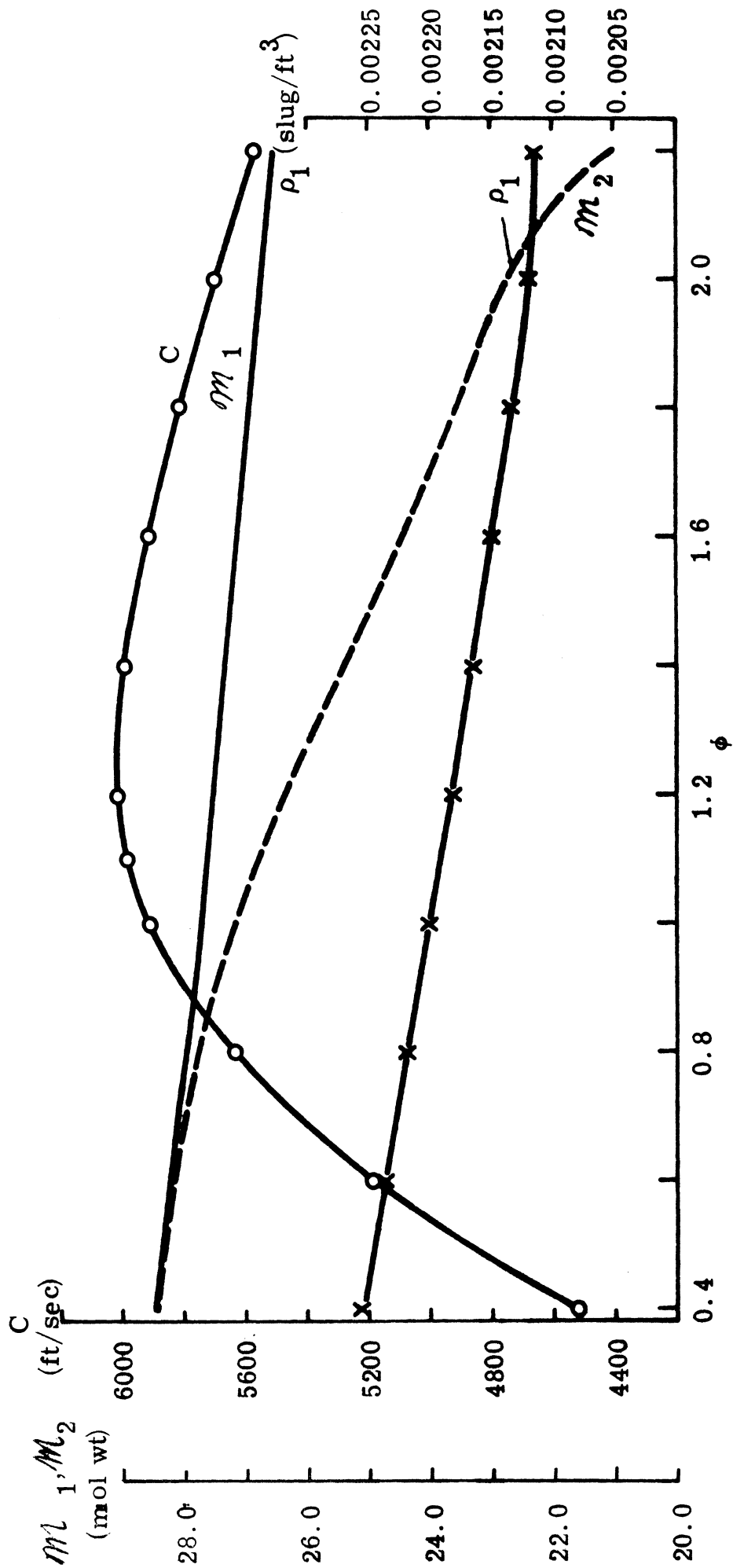
Figure 7(a). Detonation Properties—Methane-Air

26
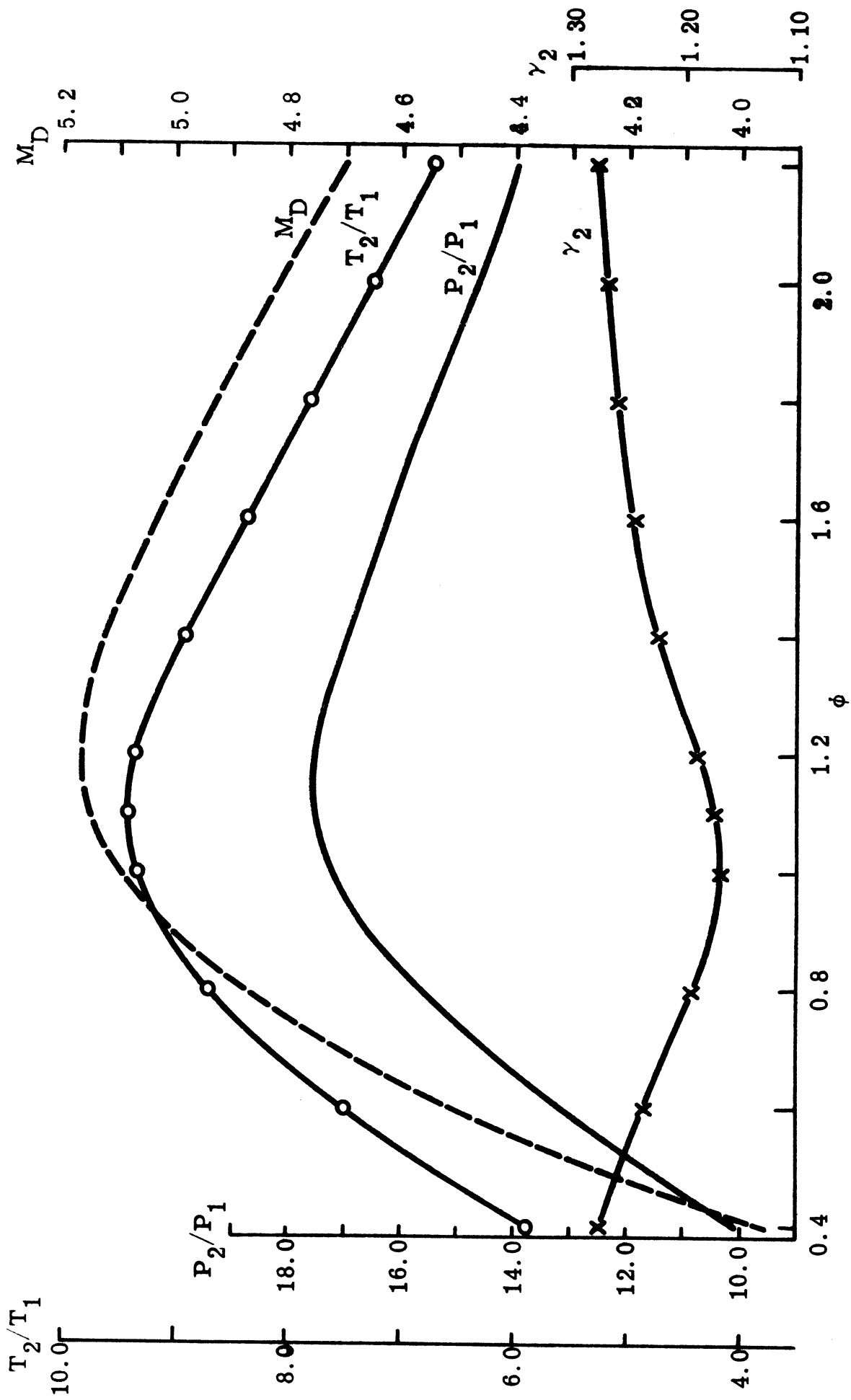
Figure 7(b). Detonation Properties—Methane-Air

27

MAPP:

C_3H_8	18.58% (by vol)	C_3H_4 ($CH_2 = C = CH_2$)	24.48%
C_3H_6	7.29%	C_3H_4 ($CH_3C \equiv CH$)	35.92%
C_4H_{10}	13.74%		

C
(ft/sec)

$\mathcal{M}_1$, $\mathcal{M}_2$
(mol, wt)

ρ_1 (slug/ft^3)

0.002400 0.002350 0.002300

6000

5400

5000

4600

31.0

28.0

26.0

24.0

0.4 0.8 1.0 1.6 2.0

C

$\mathcal{M}_1$

ρ_1

$\mathcal{M}_2$
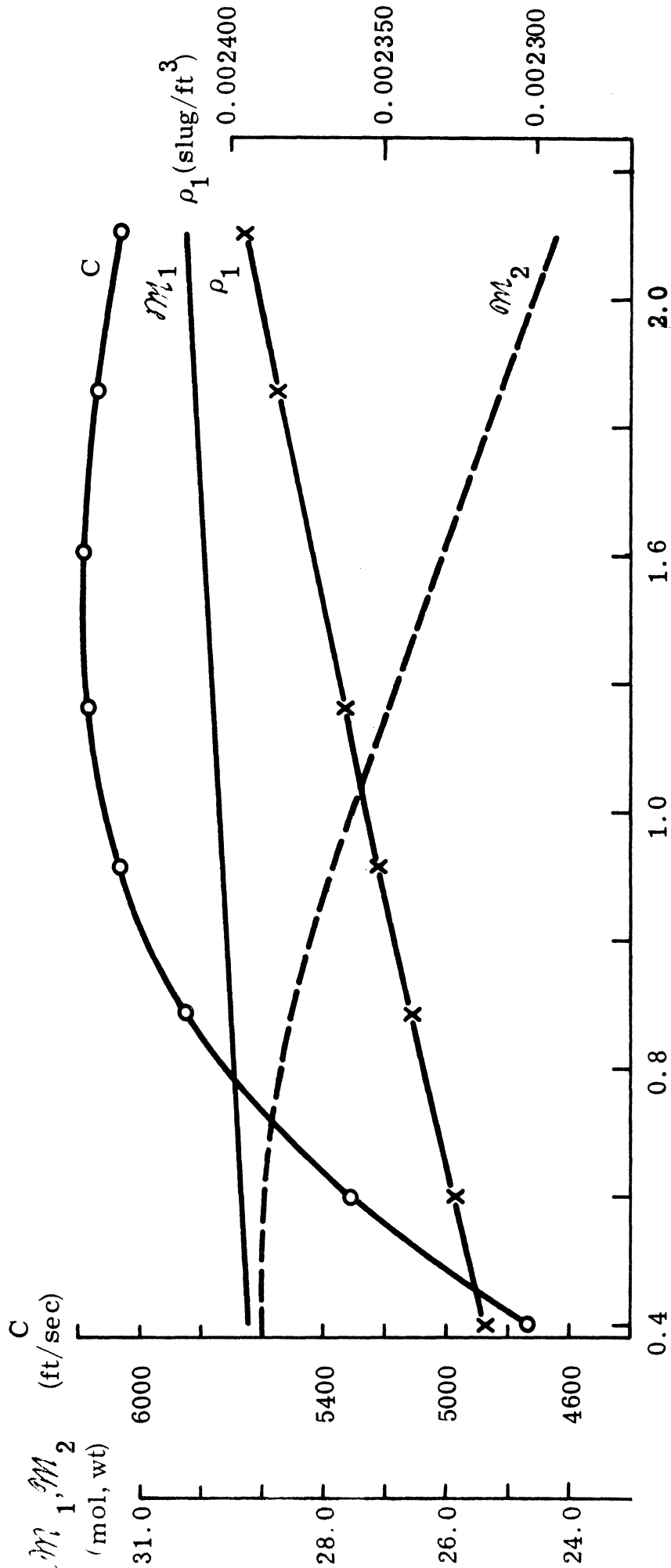
Figure 8(a). Detonation Properties—MAPP-Air

28
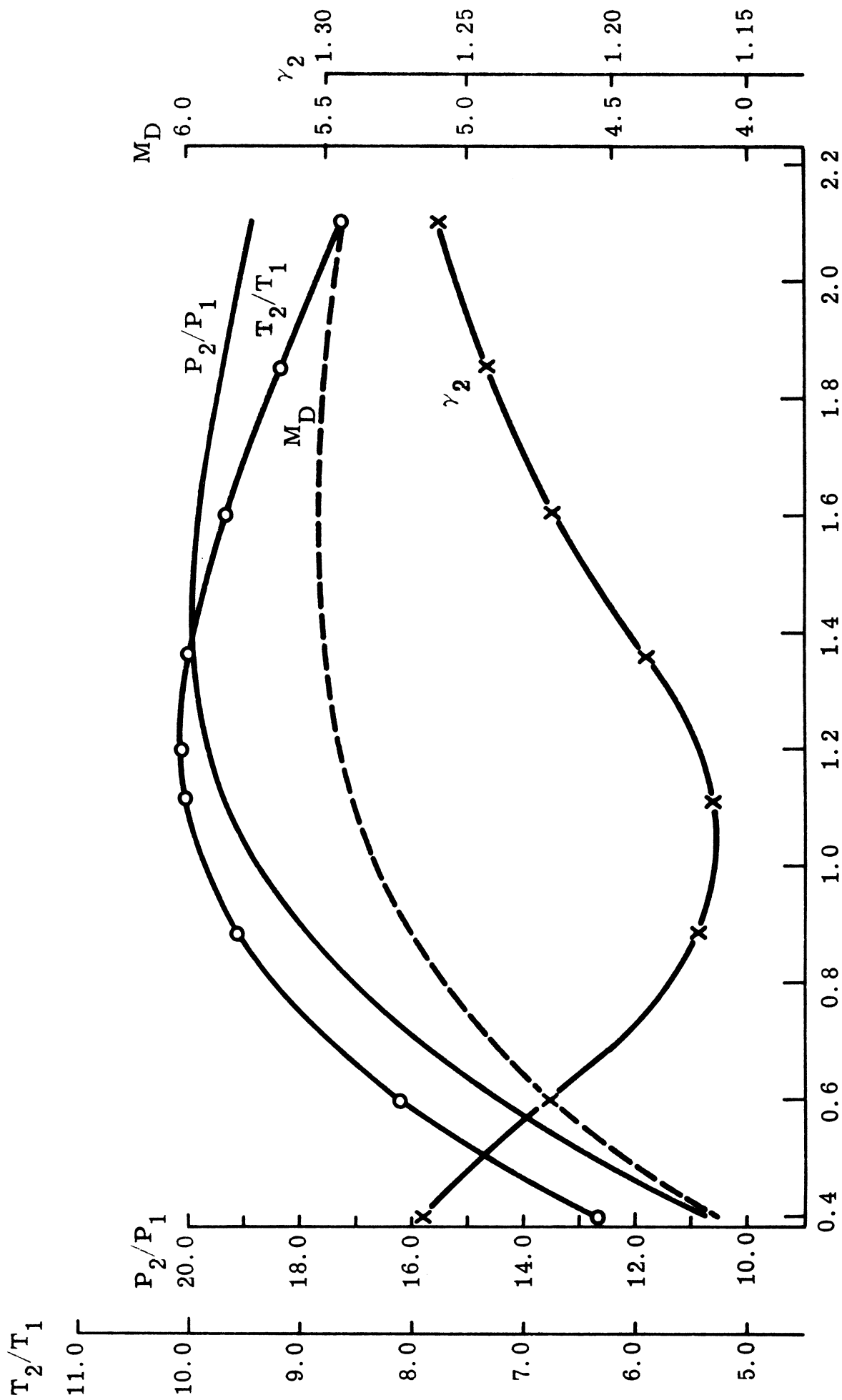
Figure 8(b). Detonation Properties—MAPP Air

TABLE IV(a). PROPERTIES OF METHANE AIR DETONATIONS

Air-CH$_4$

ϕ	1	2	γ_2	P_2/P_1	T_2/T_1	C	M_D	ρ_1
	mole wt					ft/sec		slug/ft^3
0.2	28.701	28.701	1.3167	6.278	3.832	3548.513	3.11	0.0022763
0.4	28.446	28.444	1.2732	10.038	5.879	4523.895	3.95	0.0022561
0.6	28.201	28.171	1.2364	13.13	7.51	5180.055	4.50	0.0022368
0.8	27.966	27.785	1.1944	15.62	8.70	5634.774	4.87	0.0022150
1.0	27.739	27.175	1.1689	17.20	9.33	5910.033	5.09	0.0022001
1.1	27.629	26.780	1.1730	17.52	9.42	5983.851	5.15	0.0021868
1.2	27.521	26.335	1.1889	17.51	9.35	6016.003	5.16	0.0021828
1.4	27.311	25.375	1.2244	16.96	8.91	5990.413	5.12	0.0021662
1.6	27.109	24.439	1.2453	16.26	8.36	5911.017	5.03	0.0021501
1.8	26.914	23.570	1.2588	15.52	7.80	5810.297	4.93	0.0021346
2.0	26.725	22.769	1.2694	14.76	7.25	5695.469	4.82	0.0021196
2.2	26.543	22.033	1.2786	13.98	6.72	5568.502	4.70	0.0021052
2.4	26.367	21.355	1.2869	13.18	6.21	5430.052	4.56	0.0020912
2.8	26.032	20.152	1.3025	11.54	5.25	5118.376	4.27	0.0020647
3.0	25.873	19.620	1.3088	10.70	4.80	4945.150	4.12	0.0020520

TABLE IV(b). PROPERTIES OF MAPP-AIR DETONATIONS

Air-Mapp

φ	mole wt 1	mole wt 2	γ_2	P_2/P_1	T_2/T_1	C ft/sec	M_D	ρ_1 slug/ft^2
0.2	29.092	28.993	1.3115	6.769	4.089	3665.310	3.23	0.0023073
0.4	29.218	29.018	1.2661	10.693	6.338	4666.282	4.13	0.0023173
0.6	29.342	28.981	1.2218	14.450	8.101	5318.504	4.71	0.0023272
0.6595	29.378	28.932	1.2068	15.344	8.515	5463.188	4.845	0.0023301
0.8885	29.516	28.510	1.1668	17.934	9.515	5850.323	5.201	0.0023411
1.1223	29.654	27.814	1.1632	19.372	10.009	6066.855	5.406	0.0023519
1.3610	29.792	26.960	1.1868	19.888	9.997	6168.888	5.510	0.0023630
1.6049	29.930	26.027	1.2196	19.744	9.654	6178.413	5.531	0.0023739
1.8542	30.067	25.101	1.2434	19.365	9.167	6135.752	5.505	0.0023848
2.1089	30.207	24.225	1.2603	18.875	8.643	6066.527	5.456	0.0023957
2.3692	30.345	23.405	1.2744	18.319	8.112	5979.586	5.390	0.0024068
2.6350	30.483	22.641	1.2872	17.690	7.582	5876.897	5.309	0.0024177
2.9076	30.621	21.984	1.2972	16.944	7.051	5748.29	5.205	0.0024286
3.1860	30.759	21.847	1.2620	16.900	6.877	5682.674	5.157	0.0024395

TABLE V. AVERAGE VALUE OF

$$\delta(\gamma_2, \nu)$$

ν	$\delta(\gamma_2, \nu)_{avg}$
1	0.190
2	0.138
3	0.135

The quantities $\overline{I}(t)/t^{\nu+1}$ for $\nu = 1, 2$ and $\overline{I}(t)/t^3$ for $\nu = 3$ depend upon

ρ_1, C, and M_D [(Equations (23), (24))] and so vary appreciably with the equiv-

lence ratio ϕ. With these impulse functions, which are plotted in Figures 9

and 10, $\overline{I}(t)$ is readily determined for C-J waves in air methane and air-

MAPP mixtures. It is of interest to note that the peak values of $\overline{I}(t)$ seem

to occur for rich mixtures with an equivalence ratio of $\phi \approx 1.2$ for air

methane and $\phi \approx 1.5$ for air-MAPP.

Since $r_s = Ct$ it follows that

$$\frac{\overline{I}(r_s)}{r_s^{\nu+1}} = \frac{\overline{I}(t)}{t^{\nu+1}}\left(\frac{1}{C^{\nu+1}}\right) \qquad \nu = 1, 2 \qquad (28)$$

and

$$\frac{\overline{I}(r_s)}{r_s^3} = \frac{\overline{I}(t)}{t^3}\frac{1}{C^3} \qquad \nu = 3 \qquad (29)$$

32
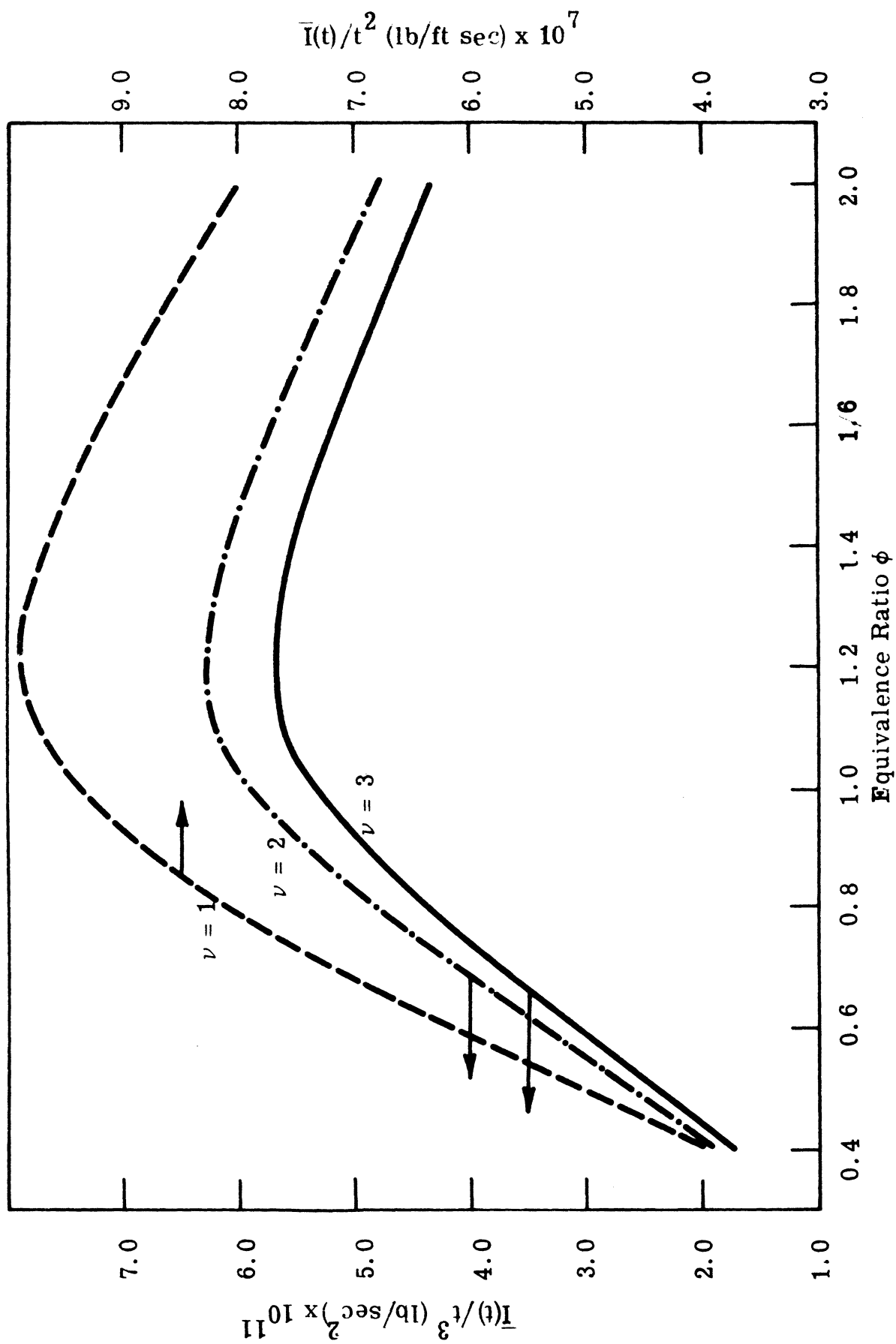
Figure 9. Total Ground Impulse CH_4-Air
$p_1 = 1$ atm, $T_1 = 298.16^{O}K$
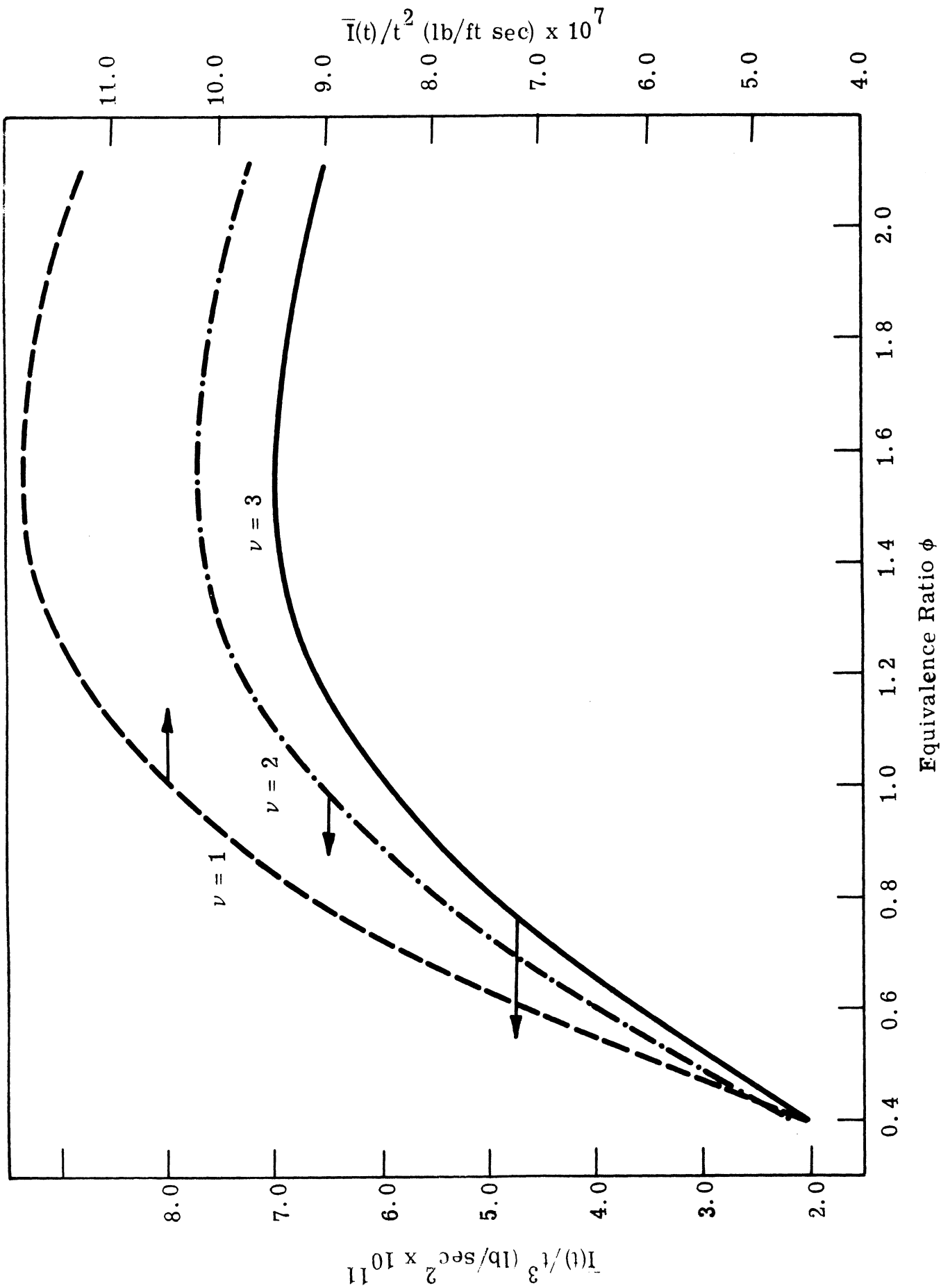
Figure 10. Total Ground Impulse Mapp-Air

$p_1 = 1$ atm, $T_1 = 298.16^O$K

4. Ground Impulse from Ideal Fuel-Air Explosion

As indicated in subsection B, above, the ideal model of a FAE behaves as a blast wave for $r_s < r_*$ and as a Chapman-Jouguet Detonation for $r_s > r_*$. The ground impulse generated by this ideal FAE is determined below.

A wave with cylindrical symmetry, $\nu = 2$, is considered. Then for $r_s < r_*$ the impulse is simply that due to a blast wave and is given by Equation (19)

$$\bar{I}(r_s) = 2\pi \left(\frac{E_o \rho_1}{\alpha}\right)^{1/2} \beta \, r_s^{\,2} \tag{19}$$

When $r_s > r_*$, the entire FAE flow field is replaced by that due to a Chapman-Jouguet detonation. Hence the ground impulse is approximated by

$$\bar{I}(r_s) = \bar{I}_{CJ}(r_s) - \bar{I}_{CJ}(r_*) + \bar{I}_{BW}(r_*) \tag{30}$$

Thus when $r_s = r_*$, $I(r_s)$ corresponds to the blast wave ground impulse, while with $r_s > r_*$, $\bar{I}(r_s)$ is the ground impulse generated by the blast wave up to $r_s = r_*$ plus the ground impulse generated by the C-J detonation for $r_s > r_*$. Subscripts CJ and BW refer to the detonation and blast wave, respectively.

Using the relations for blast wave and C-J wave impulse Equation (30) becomes

$$\bar{I}(r_s) = \frac{2\pi \rho_1 C}{3} \left[\delta(\gamma_2, 2) - \frac{1}{2\gamma_1 M_D^2} \right] (r_s^3 - r_*^3)$$

$$+ 2\pi \left(\frac{E_0 \rho_1}{\alpha} \right)^{1/2} \beta(\gamma_1, 2) \, r_*^2 \qquad (31)$$

with

$$r_* = \left(\frac{E_0}{\pi Q \rho_1} \right)^{1/2}$$

It is assumed that the blast wave propagates through the unburned gas

so that $\beta(\gamma, 2)$ is evaluated for $\gamma = \gamma_1$. Using Equation (5) the expression for

r_* can also be written in the form

$$r_*^2 = \frac{2E_0 (\gamma_2^2 - 1)}{\pi \gamma_1 p_1 M_D^2} \qquad (32)$$

The results above can also be expressed in terms of the time t from

the initiation of the secondary blast. Thus, for

$$t < t_* \quad ; \quad \bar{I}(t) = 2\pi E_0 (\beta/\alpha) t \qquad (33)$$

where t_* corresponds to the time at which the blast wave radius reaches

the critical value r_*. Thus

$$t_* = r_*^2 \left(\frac{\alpha \rho_1}{E_0} \right)^{1/2} \qquad (34)$$

36

For $t > t_*$

$$\bar{I}(t) = \frac{2\pi \, \rho_1 \, C^4}{3} \left[\delta(\gamma_2, 2) - \frac{1}{2\gamma_1 \, M_D^2} \right] (t^3 - t_*^3)$$

$$+ \, 2\pi \, E_0 \, (\beta/\alpha) \, t_* \tag{35}$$

5. Sample Computation

At this point it is useful to carry out a sample computation. Experiments in the segmented test section described in Reference 1, indicated that the critical value of E_0 to initiate a C-J detonation in an air-MAPP mixture with equivalence ratio $\phi = 0.563$ is

$$E_0 = 4.38 \times 10^5 \text{ (ft-lb)/ft}$$

which is equivalent to 150 gm of Detasheet per foot (using an energy release of 2911 ft-lb of energy release per gm of Detasheet[1]. For the above air-MAPP mixture

$$M_D = 4.69 \qquad\qquad \rho_1 = 2.29 \times 10^{-3} \text{ slug/ft}^3$$

$$\gamma_1 = 1.30 \qquad\qquad C = 5320 \text{ ft/sec}$$

$$\gamma_2 = 1.23$$

Then with $p_1 = 14.7$ psia, i.e., the sea level atmospheric pressure

$$r_* = \left[\frac{2(4.38) \times 10^5 \text{ lb } (1.51 - 1)}{3.14(1.30)(14.7)(144)(\text{lb/ft}^2)(21.9)} \right]^{1/2}$$

$$= 1.54 \text{ ft}$$

37

From Figure 4 $\alpha\,(\gamma_1,\ 2) = 1.22$ where γ_1 is the ratio of specific

heats of the unburned fuel-air mixture.

From Figure 5 $\beta(\gamma, \nu) = \beta(1.3, 2) = 0.052$. Then with $r < r_*$ the

blast wave impulse from Equation (19) becomes

$$\bar{I}(r_s) = 2\pi\left(\frac{E_o\rho_1}{\alpha}\right)^{1/2} \beta\, r_s^{\,2}$$

$$= 6.28\left(\frac{4.38 \times 10^5 \times 2.29 \times 10^{-3}}{1.22}\right)^{1/2} (0.052)\, r_s^{\,2}$$

$$= 9.36\, r_s^{\,2}\ \text{lb sec} \qquad\qquad r_s\ \text{in ft}$$

At the critical radius r_*

$$I_{BW}(r_*) = 9.36\, r_*^{\,2} = 9.36(1.54)^2 = 22.2\ \text{lb sec}$$

The next step is to compute the impulse $\bar{I}_{CJ}(r_s)$ generated by the

detonation through the air-MAPP mixture. $\bar{I}_{CJ}(r_s)$ is given by

$$\bar{I}_{CJ}(r_s) = \frac{2\pi\,\rho_1\, C\, r_s^{\,3}}{3}\left[\delta(\gamma_2, 2) - \frac{1}{2\gamma_1\, M_D^{\,2}}\right] \qquad (26)$$

As indicated in the discussion above, $\delta(\gamma_2, \nu)$ is essentially independent

of γ_2 so that the average value $\delta(\gamma_2, 2) = 0.138$ can be used. Then

38

$$\bar{I}_{CJ}(r_s) = \frac{6.28(2.29)(10^{-3})(5.32)(10^3)}{3.0} \left[0.138 - \frac{1}{2.0(1.30)(4.69)^2} \right] r_s^3$$

$$= 3.06 \, r_s^3 \text{ lb sec} \quad r_s \text{ in ft}$$

At the critical radius r_*

$$\bar{I}_{CJ}(r_*) = 11.19 \text{ lb sec}$$

Using Equations (19) and (30) the ground impulse of an ideal FAE

in air-MAPP with $\phi = 0.563$ will be

$$\bar{I}(r_s) = 9.36 \, r_s^2 \text{ lb sec} \quad ; \, r_s < r_*$$

$$\bar{I}(r_s = 3.06 \, r_s^3 - 11.19 + 22.3$$

$$= (3.06 \, r_s^3 + 11.1 \text{ lb sec} \quad ; \, r_s > r_*$$

The variation of $I(r_s)$ with r_s for the ideal FAE considered here is

shown in Figure 11.

From Equations (33) and (35) the impulse expressed as a function

of time becomes

$$\bar{I}(t) = (1.17 \times 10^5 \, t) \text{ lb sec} \quad ; \, t < 1.88 \times 10^{-4} \text{ sec}$$

$$I(t) = (4.60 \times 10^{11} \, t^3 + 19.3) \text{ lb sec} \quad ; \, t > 1.88 \times 10^{-4} \text{ sec}$$

The variation of $I(t)$ with t is shown in Figure 12.
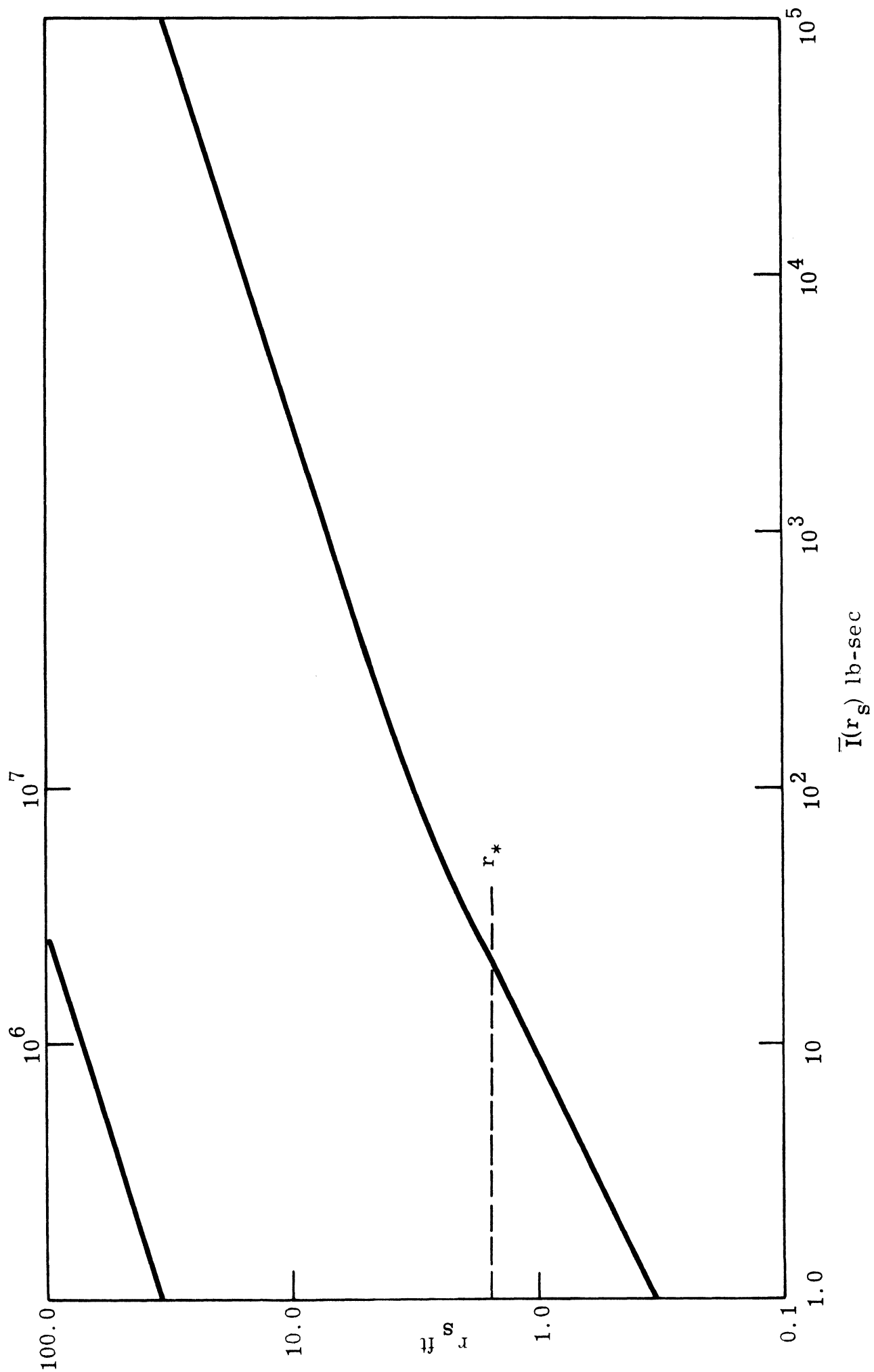
Figure 11. Variation of Ground Impulse with Wave Radius—Ideal Mapp-Air FAE; $\phi = 0.563$

40
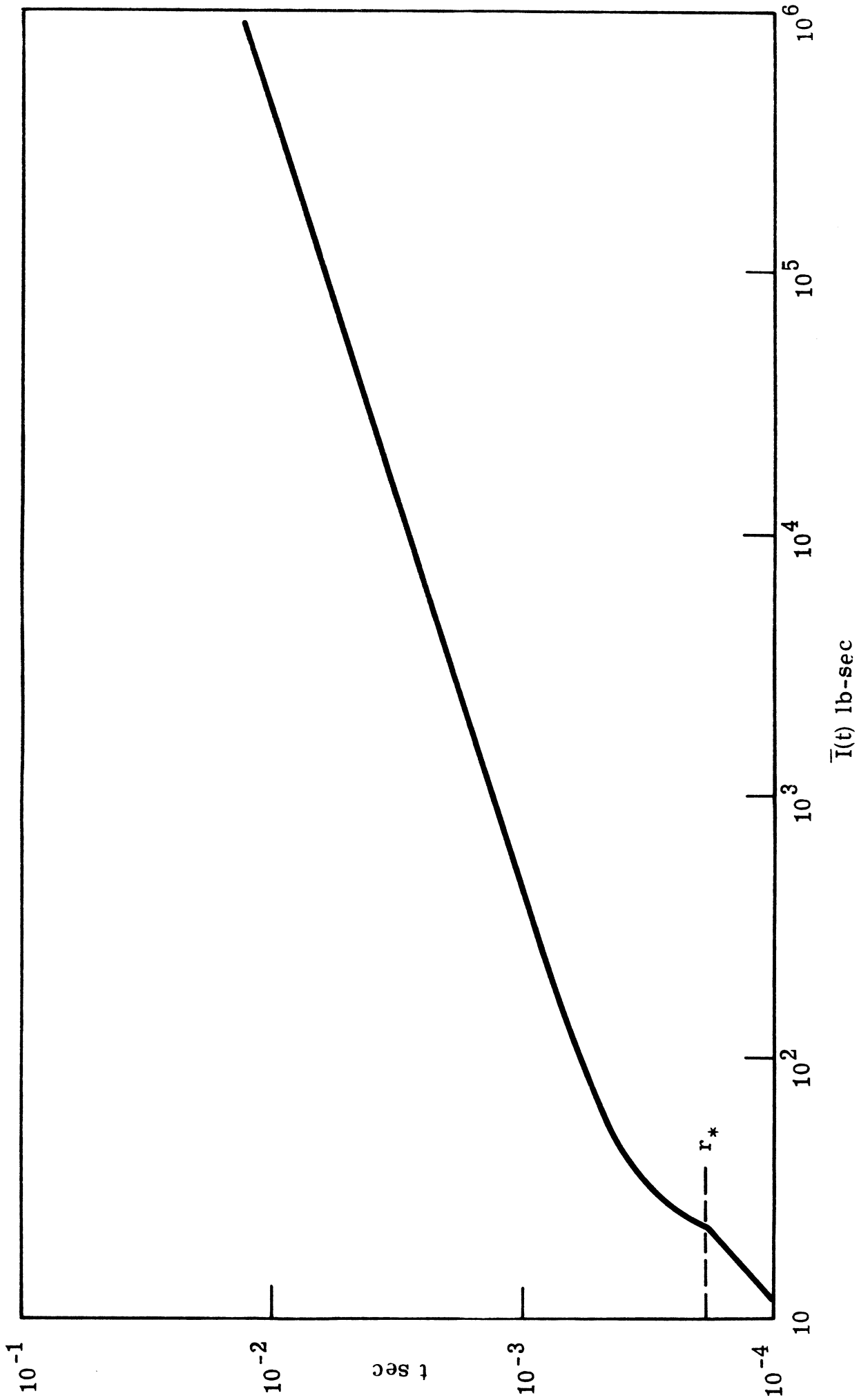
Figure 12. Variation of Ground Impulse with Time—Ideal Mapp-Air FAE: $\phi = 0.563$

41

D. DISCUSSION

Simple relations are presented above for the computation of the total ground impulse generated by an idealized FAE. Given the detonation properties and the energy released by the secondary blast, the relations presented here permit computation of ground impulse with minimal effort.

The idealized FAE involves a number of approximations. The self-similar strong blast wave solution[4,5] is used to represent the secondary blast. The perfect gas assumption is used in the region behind the leading shock, back pressure is neglected, and no attempt is made to assess how the method of blast initiation affects the wave. As indicated by Brode, Glass, and Oppenheim[7], this self-similar blast wave solution provides only a crude approximation, and with recent advances in numerical computation, more accurate theoretical solutions have become available. However, the secondary blast energy will generally be very small compared to the total energy release in a FAE, i.e., r_*; the critical radius will generally be much smaller than the fuel cloud radius. In the example treated above r_* was only 1.54 feet. Thus, even though the self-similar blast solution may be crude it has, in any case, a small influence upon the total impulse generated by the FAE, and the simplicity of this solution makes it very attractive for the model presented here. It is encouraging that there is good agreement between the idealized FAE and the tests in the segmented shock tube reported below.

42

The side relief due to the inert gas bounding the upper surface of the cloud is neglected in the ideal FAE. The expansion wave which propagates from the inert gas into the combustion products behind the C-J detonation will, no doubt, result in an appreciable drop in the ground impulse generated by a real FAE. The influence of side relief is currently under investigation.

Beyond the outer radius of the fuel cloud the FAE will continue to propagate as a decaying shock wave which provides a further contribution to the ground impulse. The propagation of this wave has been examined by R. Kiwan[8] by replacing the C-J detonation by a spherical piston moving outward with constant velocity and then examining the nature of the wave development after the piston stops. The numerical solutions obtained by Kiwan[8] look very similar to the self similar blast wave solution and suggest that the FAE behavior beyond the fuel cloud may be approximated by a blast wave with suitably chosen initial conditions. This aspect of the FAE is also under study.

The secondary blast wave is generated by an explosive line source in this ideal FAE and so has cylindrical symmetry. In an actual FAE it is more likely that the secondary blast will originate from a concentrated or point source of explosive and so will be spherical. The details of the transition from spherical to cylindrical symmetry during the initiation process will be quite complex and, of course, are not included in the

idealized **FAE**. Finally, ground shocks and reflection of the **FAE** shock front from the ground in those cases when the fuel cloud is not immediately adjacent to the ground plane are neglected.

The sample computations and the detonation data presented here have been determined for fuel in gaseous form. The C-J conditions will be modified slightly when the fuel is in liquid form. This problem, which is discussed in Reference 1, is under investigation.

SECTION III

EXPERIMENTAL RESEARCH

A. INTRODUCTION

The current objectives of this phase of the research have been to resolve in a controlled manner overall propagation details of blast initiated unconfined gas-phase and two-phase detonations. The functional dependency of blast wave propagation details upon time and radius and of detonation wave details upon time, radius, critical threshold energy, equivalence ratio, and fuel properties has been sought. To achieve these objectives the basic experimental hardware previously described[1] has been utilized with some additional alterations.

B. EXPERIMENTAL FACILITY

1. Drop Production Technique

The basic method for generating a cloud of fuel drops, employed from the beginning, has continued to perform satisfactorily. However, problems stemming from continuous blockage of needles by combustion products has dictated that an alternate sub-manifold design be chosen. Shown in Figure 13 is one such assembly of the new design. The essential improvement of this design lies with its use of hypodermic needles which may be individually replaced in the event of blockage. This will not completely eliminate the needle plugging problem but will provide a much easier technique for correcting for it.
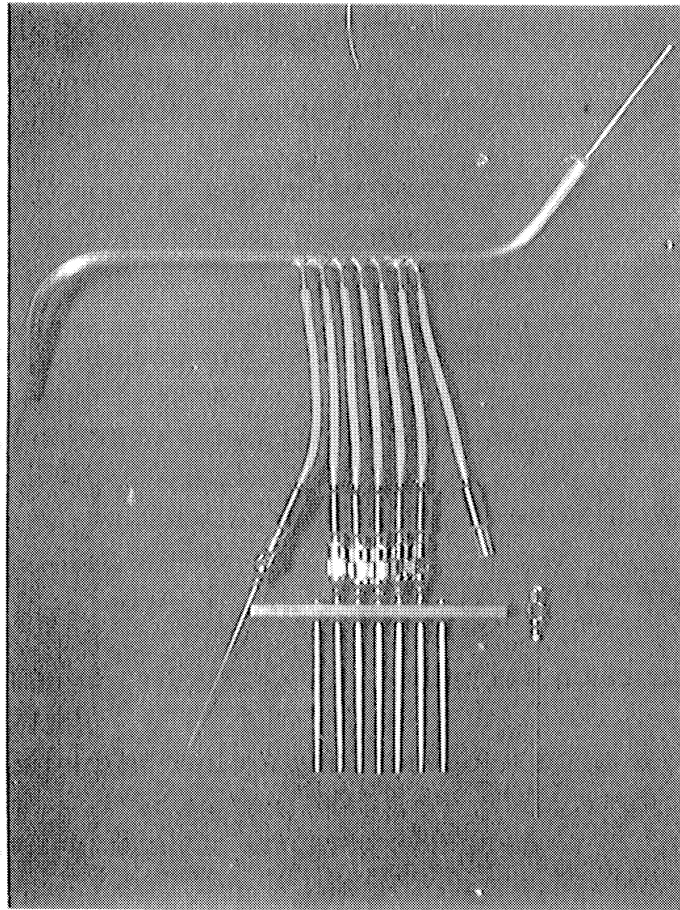
Figure 13. New Submanifold

46

2. Instrumentation

Work has continued with improving and expanding chamber instrumentation. Through these efforts notable improvements in data regularity have been observed. The pressure transducers initially employed are continuing to give satisfactory data. The pressure switches described in the previous report, which were employed as time-of-arrival devices, have, however, been replaced with others of an alternate design. Figure 14 is a drawing of the switch now being used. The primary advantages of this alternate design are its much higher reliability and ease of refurbishment. The design and development of heat transfer gages were initiated during this period. Some hardware is currently being tested, but a usable design has not yet been established.

Likewise, during the period of this report the design and construction of hardware to allow an optical study of the wave processes was begun. Initially, a design was attempted which made use of chamber windows of the size of the entire chamber side plates. This design met with little success. Thus, a new design was arrived at and hardware was subsequently obtained.

Figure 15 is an exploded view of the new chamber side plates and Pyrex windows which comprise the proposed design. The practical feasibility of this hardware shall be examined through subsequent tests.

Brass

Phenolic

Brass

Stainless Steel Foil
0.001 in. Thick

1/8 in. diam
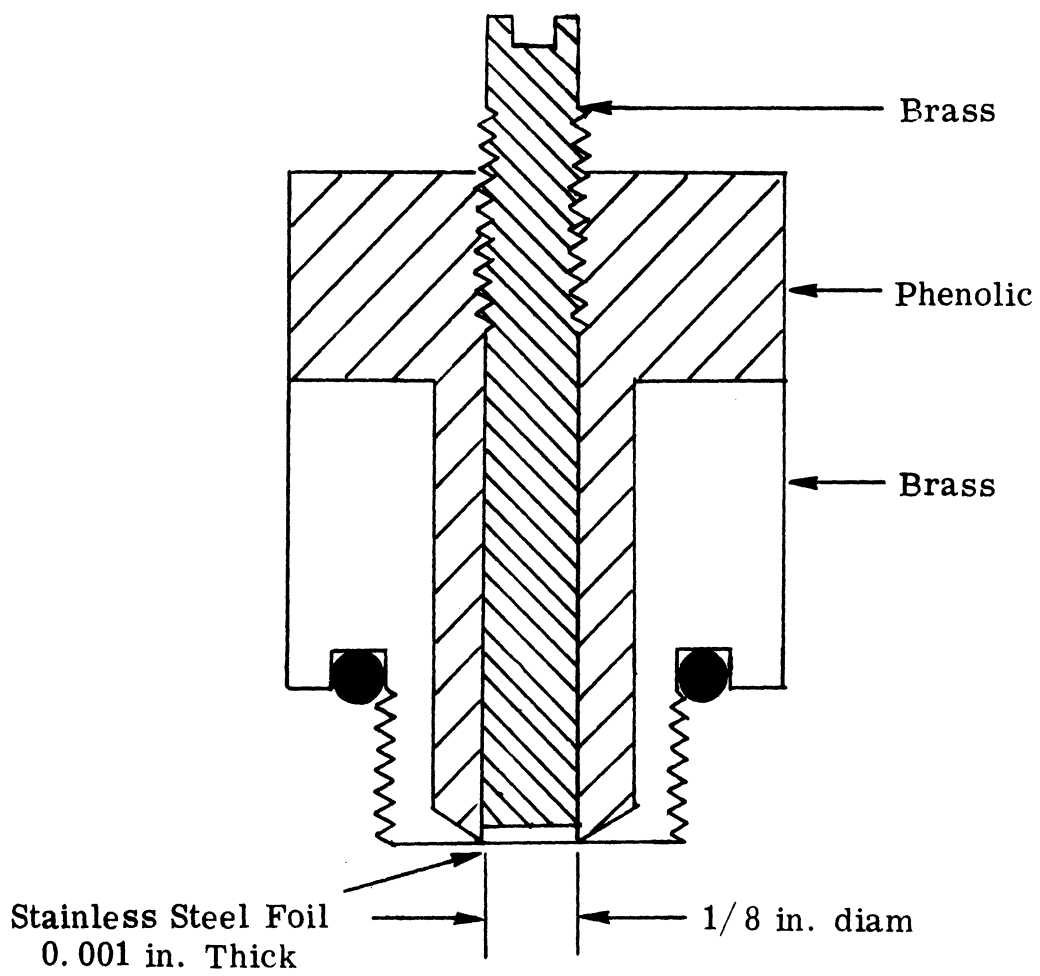
Figure 14.   Current Pressure Switch Design

48
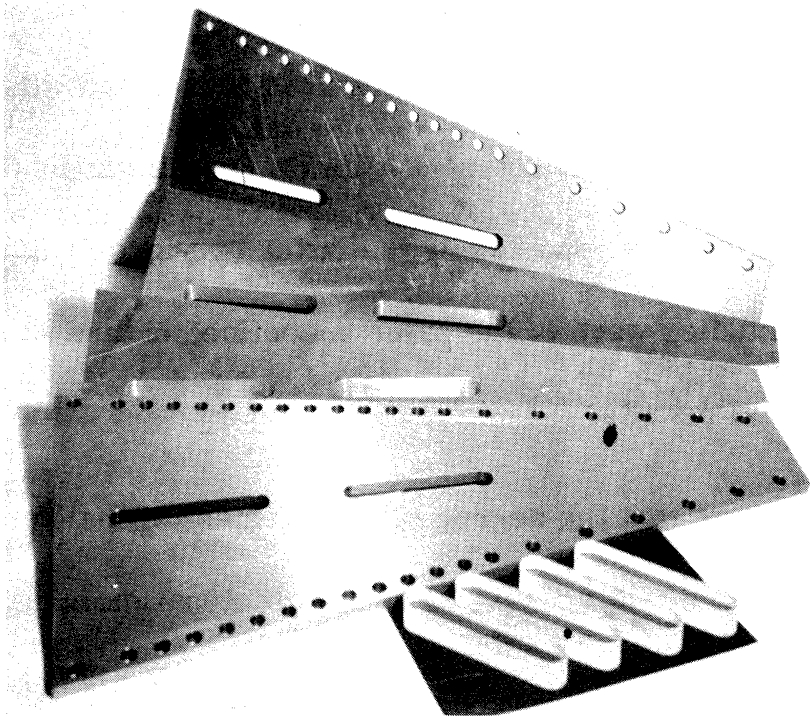
Figure 15. Side Plates and Windows for Optical Study

49

3. Gas-Phase Detonation Facility

Gas-phase detonation studies were carried out during the period

encompassed by this report. In recent years some investigations have

been made in an attempt to establish the dependency of critical threshold

energy for detonation initiation as a function of the concentration of MAPP

(hydrocarbon gas)-air mixtures. Among these investigations were the

tests performed in the confinement of the Crawshaw-Jones Apparatus[9],

the bag tests of Benedick et al.[10], and the bag tests of Collins[11]. The

investigations performed in the Crawshaw-Jones Apparatus reported

functional dependencies of detonation limits upon initiation energy

which largely went unsupported by the latter two investigations. The

two bag test studies were of the same unconfined nature and produced

nearly identical results.

It is apparent that the degree of confinement of the experimental

apparatus has an effect upon the determined detonation initiation limits.

Hence, it was of much interest to undertake MAPP-air detonation tests

in order to establish conclusively the unconfining nature of the sectored

chamber and hence its utility to the determination of fundamental in-

formation. This information is of general interest but also of particular

interest to the Air Force and FAE problem.

The gas used in these tests was MAPP, a hydrocarbon gas comprised of methyl acetylene, propane, and propadiene gases. Some results of this study are presented and discussed in sub-Section C of Section III.

Some modifications to the basic sectored chamber were necessary, and additional support hardware was required. A schematic of the gas-phase detonation apparatus is given in Figure 16. Shown in Figure 17 are the major components of the support hardware. The system employed used a MAPP-air reservoir wherein a given concentration of MAPP and air could be pre-mixed. The reservoir, which had a volume of one cubic foot, was charged to 60 psig and contained enough mixture to allow completion of up to fifteen experimental runs. This provided enough MAPP-air mixture to allow completion of runs at each concentration with but a single charging of the reservoir.

Several constraints on the handling of MAPP in such reservoir system had to be satisfied prior to successful operation. One such constraint required that if the condensed phase was to be avoided the storage pressure of MAPP must be below 80 to 100 psig for a temperature
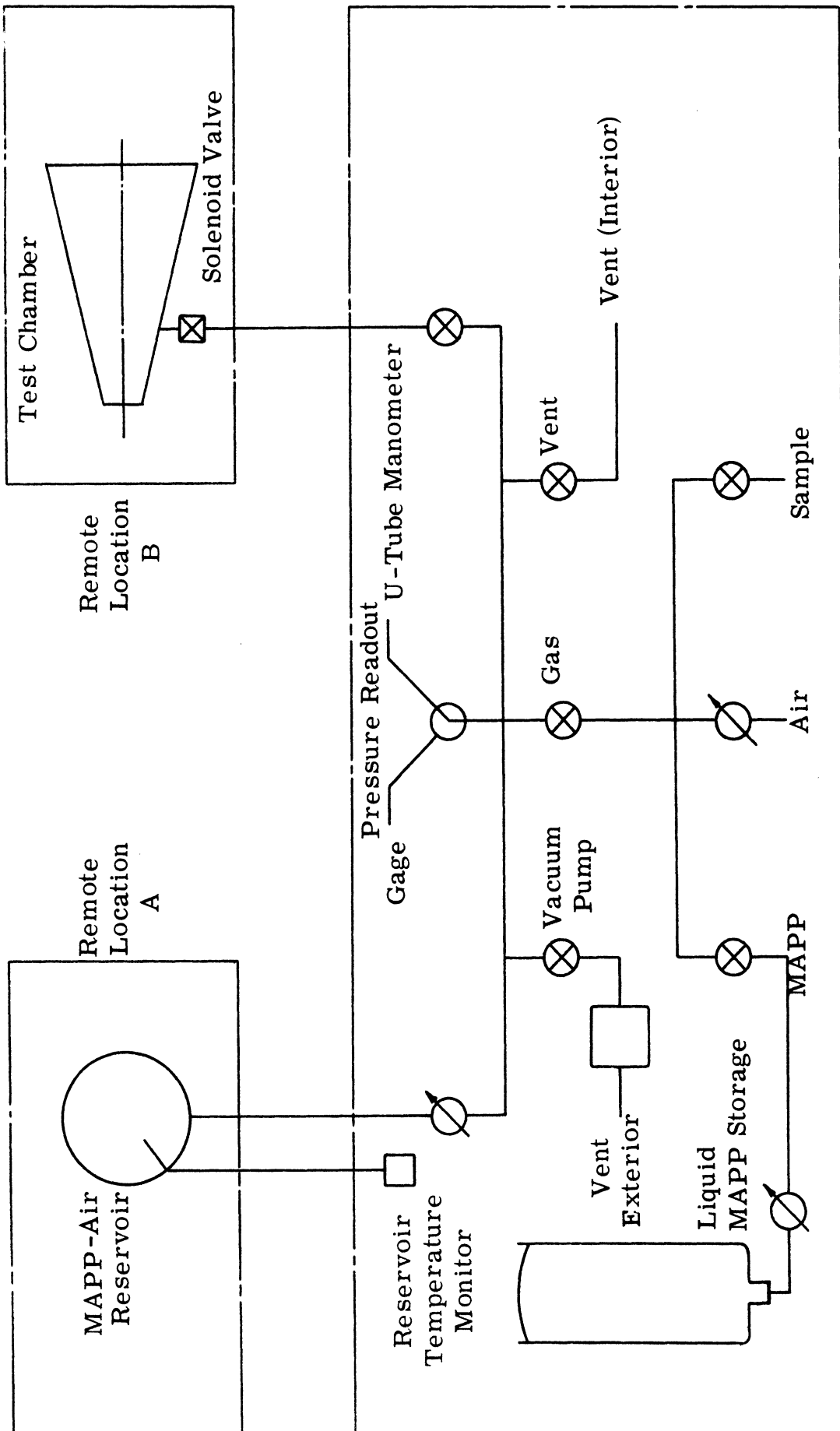
Figure 16. Schematic of Gas Detonation Apparatus

52
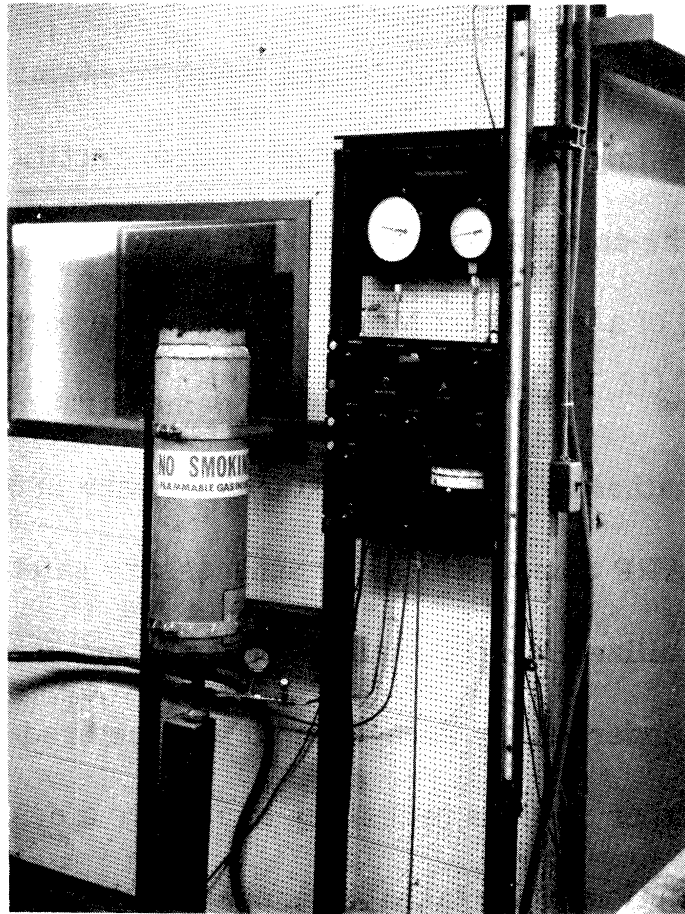
Figure 17. Gas Detonation Support Hardware

between 60 to 80°F. Hence, the reservoir was charged to 60 psig to ensure

the MAPP gas and air would mix uniformly and remain so throughout the

duration of the runs. An additional constraint required that the MAPP

gas cylinder, containing the fuel in its condensed phase, be positioned

in its inverted position.

When vapor is removed from a vessel containing a liquid hydrocarbon

mixture, a simple batch distillation without rectification (called weathering)

occurs. The compositions of liquid in equilibrium with vapor for the

weathering of a stabilized MAPP mixture have been determined by other

researchers[12, 13, 14]. Their results demonstrate the potential hazards

with the weathering of MAPP mixtures. Hence in order to avoid non-

uniform MAPP compositions and unnecessary safety hazards stemming

from unstabilized MAPP, liquid MAPP was metered from its inverted

storage cylinder. Only enough liquid was metered out and allowed to ex-

pand to a vapor as was necessary to achieve a desired partial pressure.

Many precautions were taken to insure that the desired composition was that

which was obtained in the reservoir. Samples of reservoir chargings were

taken and analyzed by gas chromatographic techniques. The degree of success

achieved in obtaining desired MAPP-air concentrations is shown in Table VI.

The sectored chamber required plugs for the holes in the top plate,

through which the capillary needles for the two-phase studies normally

TABLE VI. MAPP -AIR CONCENTRATIONS BY VOLUME AT
WHICH TESTS WERE PERFORMED

Desired	Obtained	Percent Difference
9.5	9.7	-2.1
8.5	8.5	0.0
7.0	6.8	2.8
6.0	6.0	0.0
4.5	4.3	4.4
3.75	3.8	-1.3
3.3	3.3	0.0
3.0	2.9	3.3

penetrate. The chamber also required a fixture at the downstream end to hold a mylar diaphragm which is replaced for each run. These changes along with clay packed around the blasting cap leads and silicone sealant in strategic locations proved to be satisfactory enough to pull the chamber vacuum down to within 0.2 to 0.5 in. of a hard vacuum.

The procedure for a given gas detonation run was as follows:

1. Clean chamber of combustion products.

2. Insert blasting cap——Detasheet initiation charge, secure breech, and clay packing.

3. Secure mylar diaphragm.

4. Evacuate chamber, 20 to 30 minutes.

5. Recharge to 1 atm with current MAPP-air mixture.

6. Evacuate all plumbing of MAPP-air mixture from chamber to reservoir.

7. Initiate timing sequence to detonate mixture.

C. RESEARCH RESULTS AND DISCUSSION

1. Introduction

Experimental FAE research efforts have remained focused upon evaluation of the two limiting cases for an FAE model — the strong cylindrical blast wave and the cylindrical Chapman-Jouguet detonation wave. Table VII gives a summary of experimental tests performed during the period of this report. As shown, further blast wave runs were made with

TABLE VII. SUMMARY OF EXPERIMENTAL TESTS PERFORMED

Run No.	Type	Explosive Charge (grams)	Comments
100-135	Blast Wave	1.0-2.25	Open Breech
200-211	Detonation	0.5-3.0	Kerosene 2-Air
212-217	Blast Wave	0.5	Open Breech
218-282	•Detonation	0.5-3.5	Kerosene 2-Air
283-286	Blast Wave	1.0-1.75	Open Breech
287-289	Detonation	1.25	Kerosene 2-Air
290-309	Blast Wave	1.0-3.0	Closed Breech
310-362	Blast Wave	Small Detonators[a]	Open Breech
363-418	Blast Wave	Small Detonators[a]	Closed Breech
419-559	Detonation	Small Detonator[a]-3.5	MAPP-Air

[a]DuPont electric detonators E-94 and E-101 series having energy releases smaller than generally employed—Atlas detonator.

both an open and closed breech configuration the distinction being the presence of a clay plug surrounding the blasting cap ignition wires as they exit from the breech for the closed breech configuration. The detonation runs were composed of two basic types, two-phase Kerosene 2-air and gas-phase MAPP-air. The designation Kerosene 2 is intended to distinguish it from the previously employed lesser refined fraction, Kerosene 1.

An in-depth analysis of the blast wave data yielded information which helps to establish the nature of the sectored chamber as an experimental model of cylindrically propagating waves. Two basic developments followed from this analysis. An energy efficiency of the sectored chamber was derived which relates the effective energy release with the calculated or maximum allowable energy released in the chamber. The second development stems from a quantitative comparison of experimental blast wave regression models with strong blast wave theory, thereby yielding a behaviorial estimate of wave processes in the sectored chamber. A presentation and discussion of two-phase and gas-phase detonation results follow.

2. Blast Wave Results

Experiments conducted in the sectored chamber without fuel present have continued. In order to make meaningful use of the blast wave data received from these tests, it was necessary to arrive at a standard reduction technique. Once established, this technique should yield self-consistent results useful

in describing the behavior of wave processes in the sectored chamber.
The reduction technique finally chosen begins with a translation of the
rough radius-time data from the raster scope photographs for a given
energy level. This rough data is then smoothed using a least squares
polynomial regression to the model

$$T = a_{01} + a_{02} R + a_{03} R^2 \qquad (27)$$

Examples of this polynomial smoothing technique are given in Figure 18.
Shown here are radius-time plots for three energy levels 1.0 gram, 1.75
grams, and 3.0 grams of Detasheet. Displayed in the plots are the actual
rough data points and the subsequent least squares fit of Equation (27) to the
data.

Equation (27) with the corresponding calculated coefficients is taken
to represent the experimental data. The equation is then used to compute
values of t_o, as previously described in Reference 1. Recall that t_o is the value
of time necessary to relate the experimental data to the imaginary origin.
All time values of the specified energy level are then adjusted by the
computed t_o. The adjusted data is then subsequently regressed by means
of the least squares fit to the following experimental models:

$$T = a_1 R + a_2 R^2 \qquad (28)$$

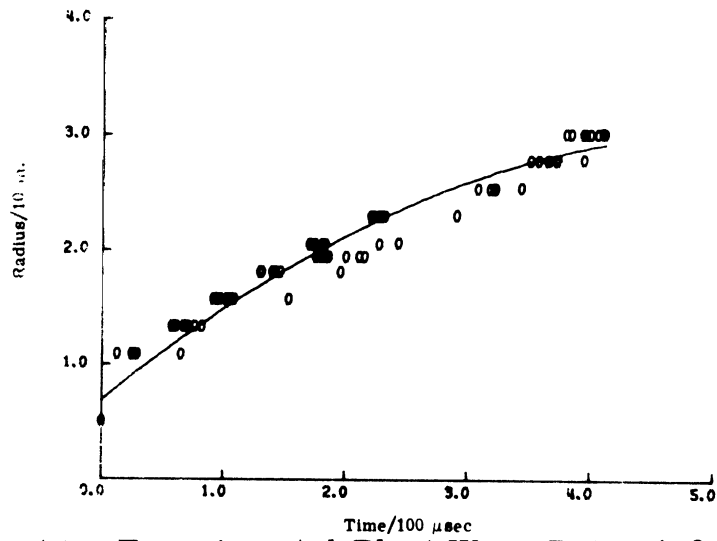$$T = b_1 R^2 \qquad (29)$$

$$T = c_1 R^{c_2} \qquad (30)$$

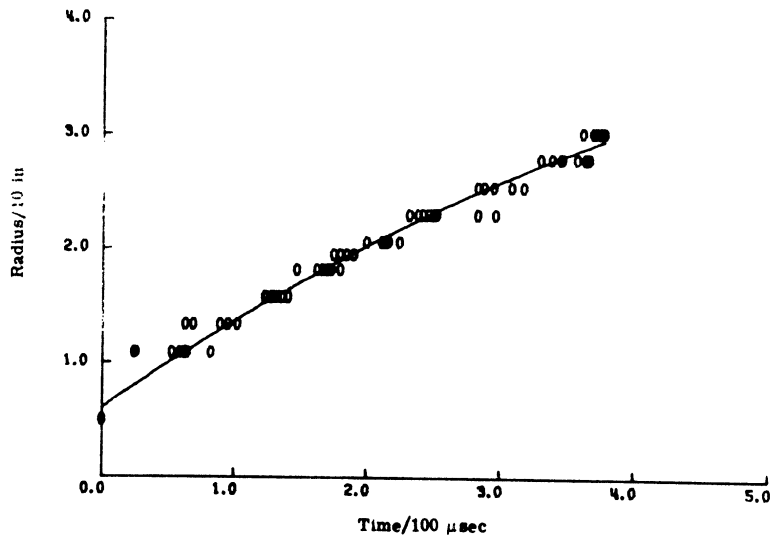Figure 18(a). Experimental Blast Wave Data, 1.0 gram

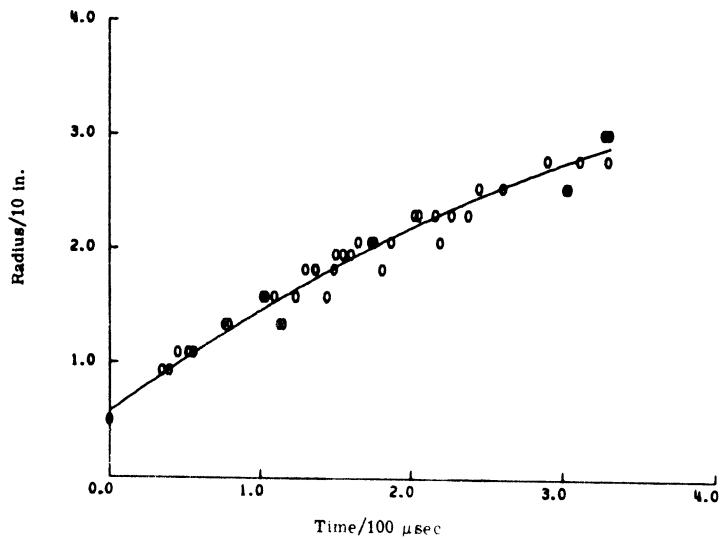Figure 18(b). Experimental Blast Wave Data, 1.75 grams

Figure 18(c). Experimental Blast Wave Data. 3.0 grams

The reason for selection of these particular models is that the experimental data should reflect second order behavior as predicted by strong cylindrical blast wave theory. It was further desired to verify that the comparison be substantially independent of the choice of mathematical regression models. Since the data has already been adjusted to the imaginary origin, no leading constants are necessary. A numerical check was performed to examine just how close to the origin the adjusted data curves come. For this purpose the adjusted data was again fit to the model of Equation (30) and new t_o's computed. This check in all cases suggested that an iterative process seeking t_o was not necessary as the t_o in the second run was within a small number of being zero. This entire data reduction technique was repeated for each energy level as characterized by a given detonator-Detasheet combination.

During the course of these tests and following data analysis it was found that the energy release experienced in the sectored chamber was less than that which may be predicted from a known quantity of Detasheet. This fact is quite justifiable on the basis that non-idealities exist in the physical model of a cylindrical blast or detonation wave. The significant deviations from an ideal blast wave model are:

(1) The existence of a physically limiting chamber suggests losses to the walls.

(2) Initiation energy release is, in fact, not instantaneous as assumed by theory. It was estimated to be of the order of 10 μsec.

(3) Initiation energy is not released uniformly along a line source.

61

The numerical values of energy efficiencies were arrived at through use

of experimental data regressed by the model of Equation (29) and the

general radius-time form of strong cylindrical blast wave theory

given in Equation (31)

$$t = (E_o/\rho_1)^{-1/2} r^2$$

or   (31)

$$t = d_1 r^2$$

Since Equations (29) and (31) are of the same general form, any dif-

ferences in radius-time behavior between the two for a given process

relates directly to deviations in their constant coefficients b_1 and d_1.

It is clear then that b_1 reflects actual behavior while d_1 reflects

theoretical behavior in the sectored chamber. This fact can be stated

by the representation of b_1 and d_1 as

$$b_1 = \left[(E_o/\rho_1)^{-1/2} \right]_{regression}$$ (32)

$$d_1 = \left[(E_o/\rho_1)^{-1/2} \right]_{calculated}$$

Then $E_{o_{reg}}$ and $E_{o_{calc}}$ are given by

$$E_{o_{reg}} = \rho_1/b_1^2$$

                                                                                            (33)

$$E_{o_{calc}} = \rho_1/d_1^2$$

An efficiency factor can now be constructed

$$\eta_e = E_{o_{reg}} / E_{o_{calc}} \qquad (34)$$

where the energies are defined by Equations (33). Thus, $E_{o_{reg}}$ follows

directly from a mathematical regression to experimental data, while $E_{o_{calc}}$

is derived from knowledge of the detonator-Detasheet combination. For

the combination of an Atlas blasting cap yielding 1110.0 ft-lbf energy and

X grams of detasheet yielding 2911.0 ft-lbf/gram, $E_{o_{calc}}$ in the sectored

chamber would become

$$E_{o_{calc}} = (12.0/2.05)(360/20)(1110.0 + 2911 \, X) \text{ ft-lbf/ft} \qquad (35)$$

Energy efficiencies can then be computed for a range of energies for

which experimental blast wave data was taken. Figure 19 gives the results

of this computation for both open and closed breech configurations. It was

deemed necessary to assess the degree which closed breech wave behavior

deviated from the open breech case. The former configuration was

employed in the MAPP-air gas-phase detonation tests. The curve dis-

played is a second order polynomial regression to all the data and was

used to describe the data in subsequent computations. The closed breech

data fell within the data scatter and hence no definite trend of its own

was determined.

In the interest of examining how closely cylindrical behavior was

modeled in the sectored chamber, experimental data was compared with
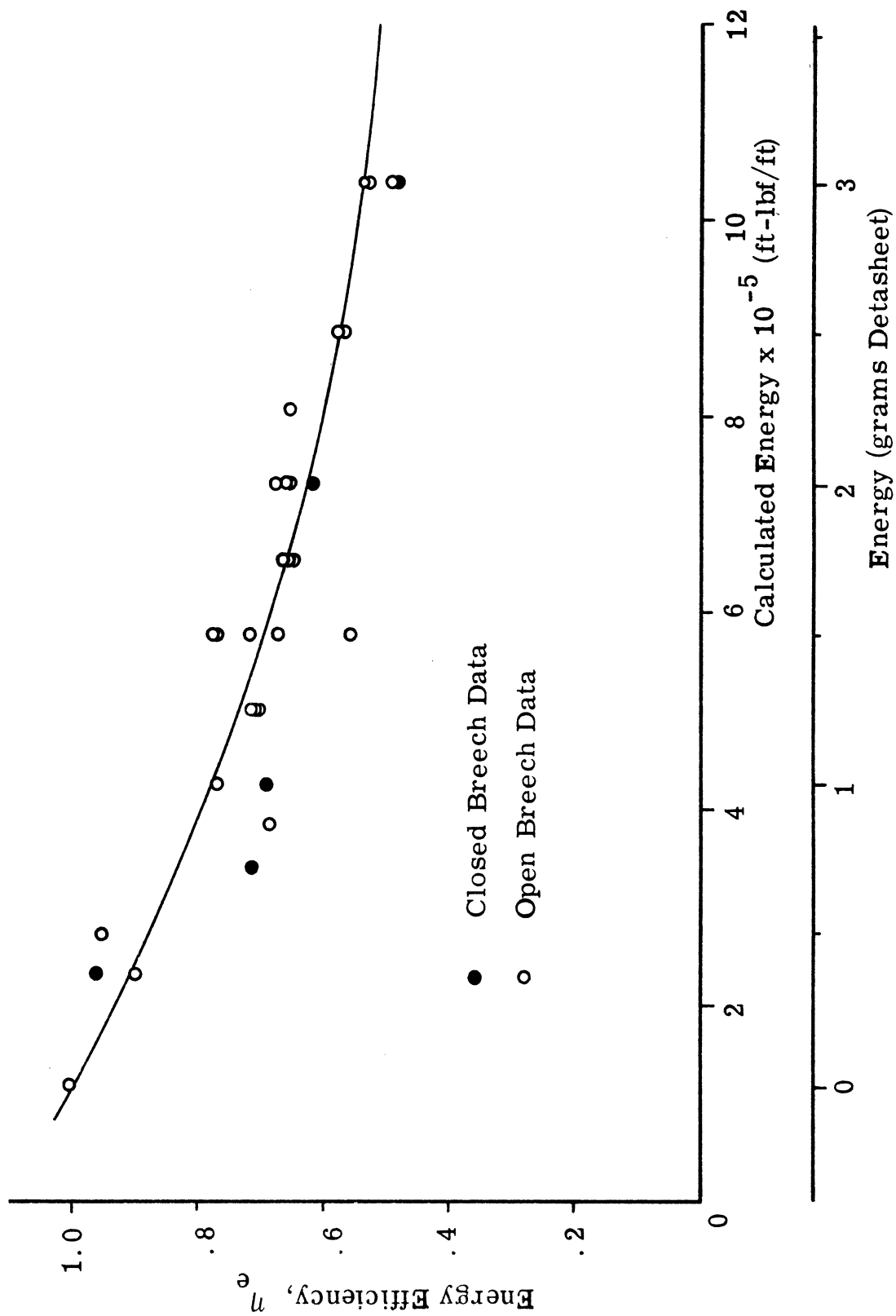
63

Figure 19. Sectored Chamber Energy Efficiency as a Function of Calculated Energy Release.

strong blast wave theory. A quantitative comparison between experiment

and theory was achieved by making use of the experimental regression

models of Equations (28), (29) and (30) and the following expressions for

cylindrical blast theory

$$r = \left(\frac{E}{\rho_1}\right)^{1/4} t^{1/2} \tag{36}$$

$$v = \frac{1}{(\gamma + 1)} \left(\frac{E}{\rho_1}\right)^{1/4} t^{-1/2} \tag{37}$$

The energy used in the above theoretical expressions was that given

by Equation (34) and repeated here as

$$E_{cylindrical} = E_{calc} \times \eta_e \ (ft\text{-}lbf/ft) \tag{38}$$

Figures 20, 21, and 22 reveal the radius-time and Mach number-radius

behavior for 0.0, 1.5, and 3.0 grams of Detasheet, respectively. Shown

in these figures are the three experimental regression models as com-

pared with strong cylindrical blast wave theory.

All the curves of Figures 20, 21, and 22 are self-consistent and

substantially in agreement about major behavioral trends. However,

Equation (29), the form for ideal strong cylindrical blast wave behavior,

is seen to give the much better agreement between experiment and theory.

In part this is to be expected because the effective energy release was

obtained by assuming such behavior. On the other hand, the adjusted

Figure 20(a). Radius versus Time Behavior of Strong Blast Wave Theory and Experimental Regression Models for 0.0 gram of Detasheet 'C'.

66

Figure 20(b). Mach Number versus Radius Behavior of Strong Blast Wave Theory and Experimental Regression Models for 0.0 gram of Detasheet 'C'.

Figure 21(a). Radius versus Time Behavior of Strong Blast Wave Theory and Experimental Regression Models for 1.5 grams of Detasheet 'C'.

Figure 21(b). Mach Number versus Radius Behavior of Strong Blast Wave Theory and Experimental Regression Models for 1.5 grams of Detasheet 'C'.
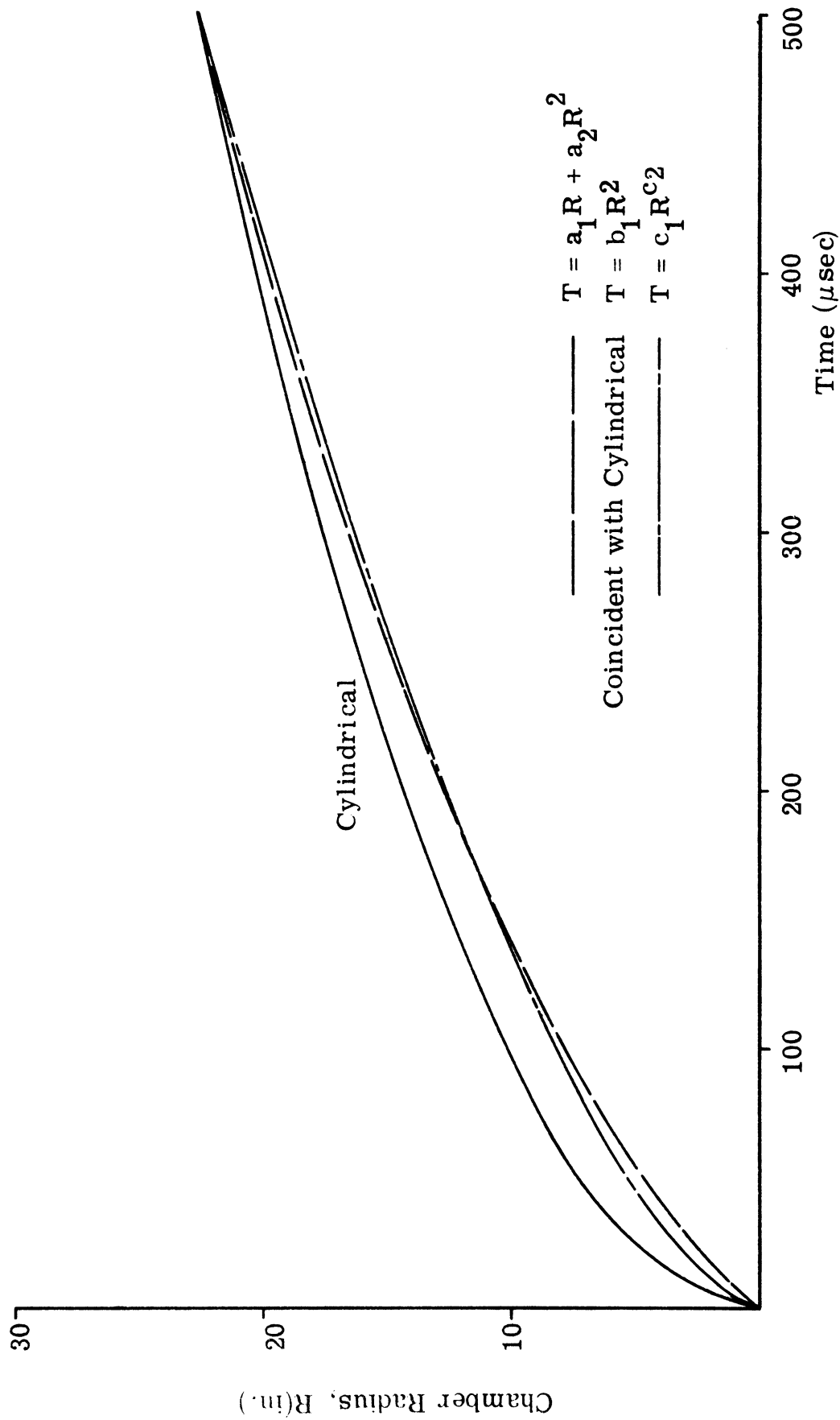
Figure 22(a). Radius versus Time Behavior of Strong Blast Wave Theory and Experimental Regression Models for 3.0 grams of Detasheet 'C'.
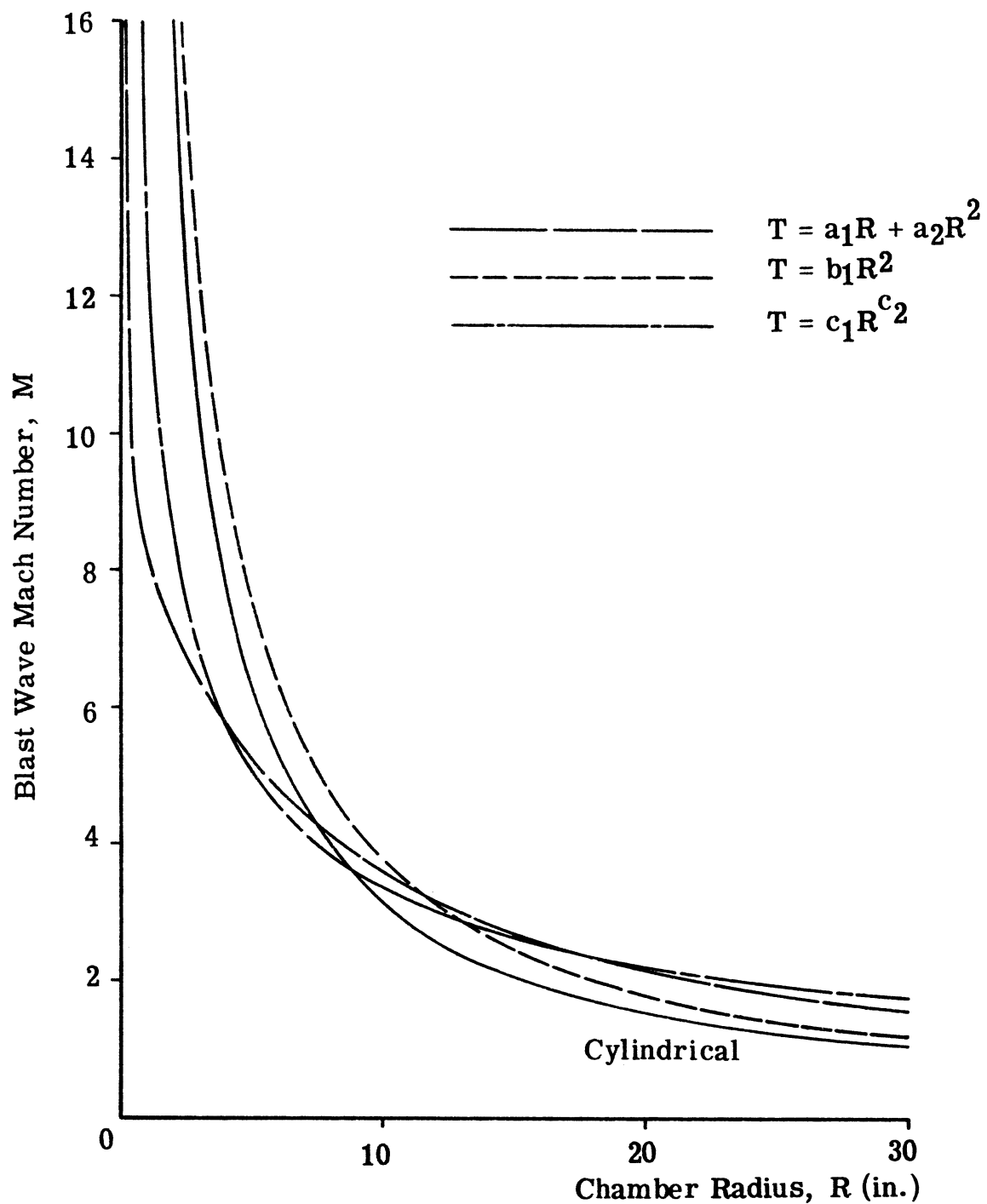
70
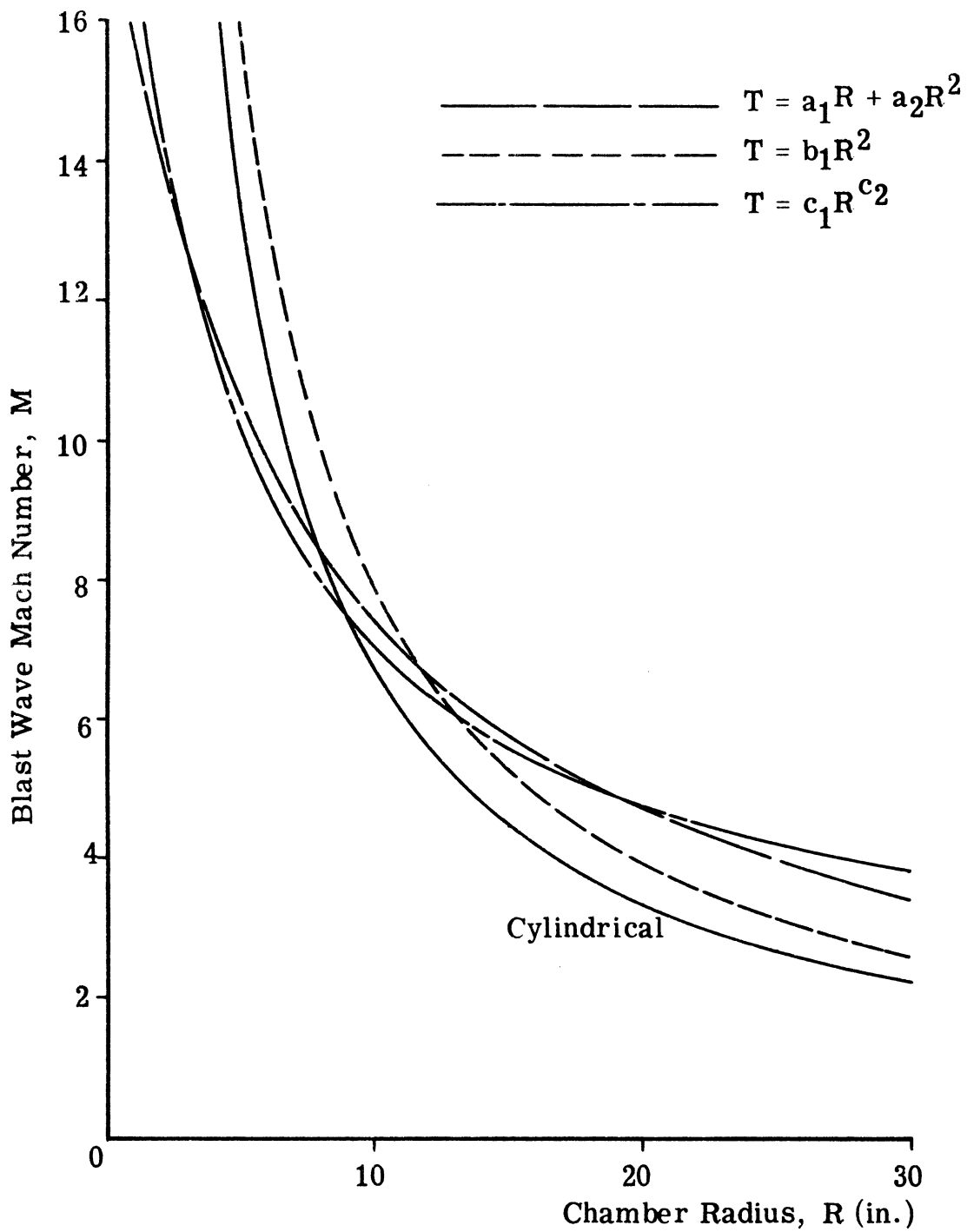
Figure 22(b). Mach Number versus Radius Behavior of Strong Blast Wave Theory and Experimental Regression Models for 3.0 grams of Detasheet 'C'.
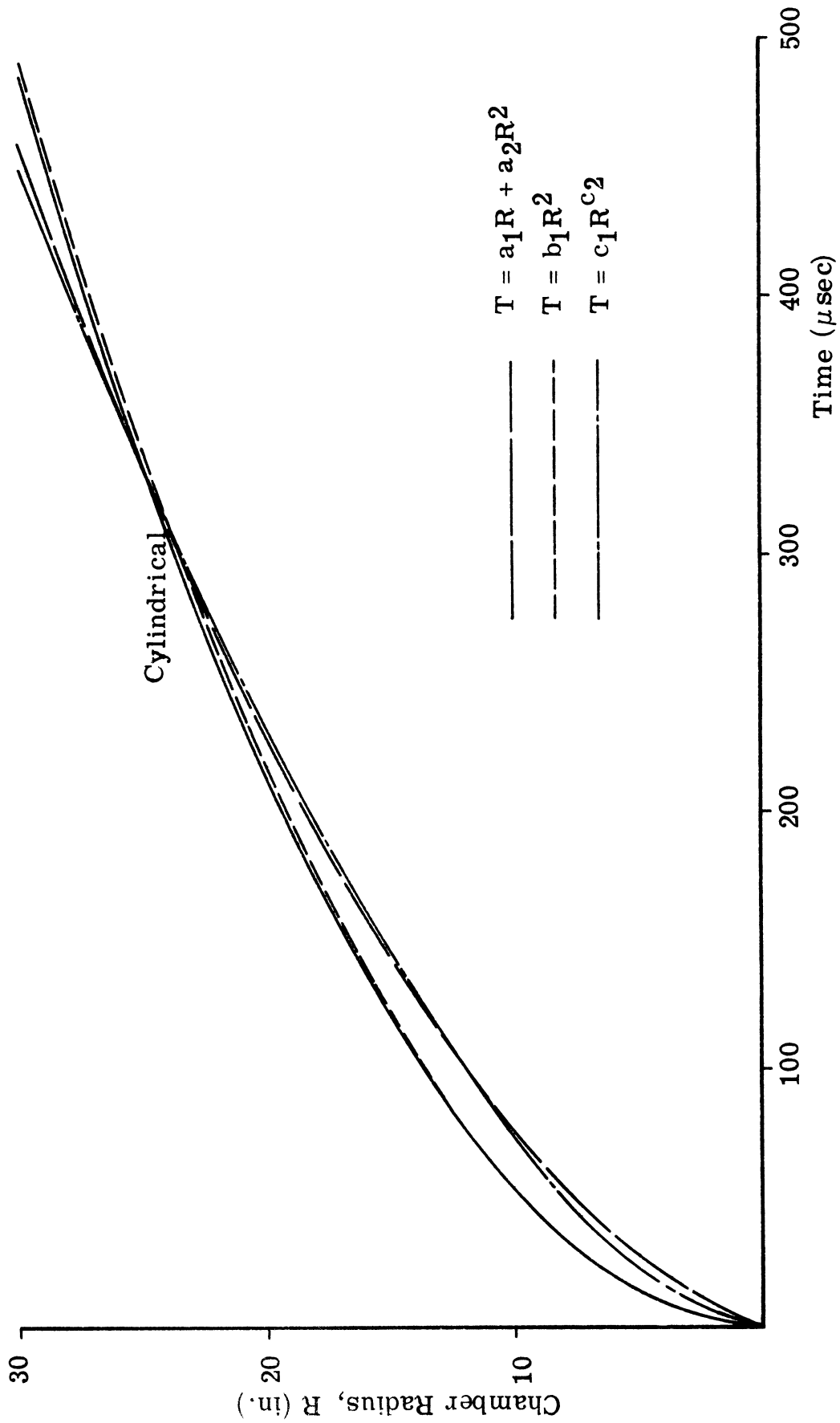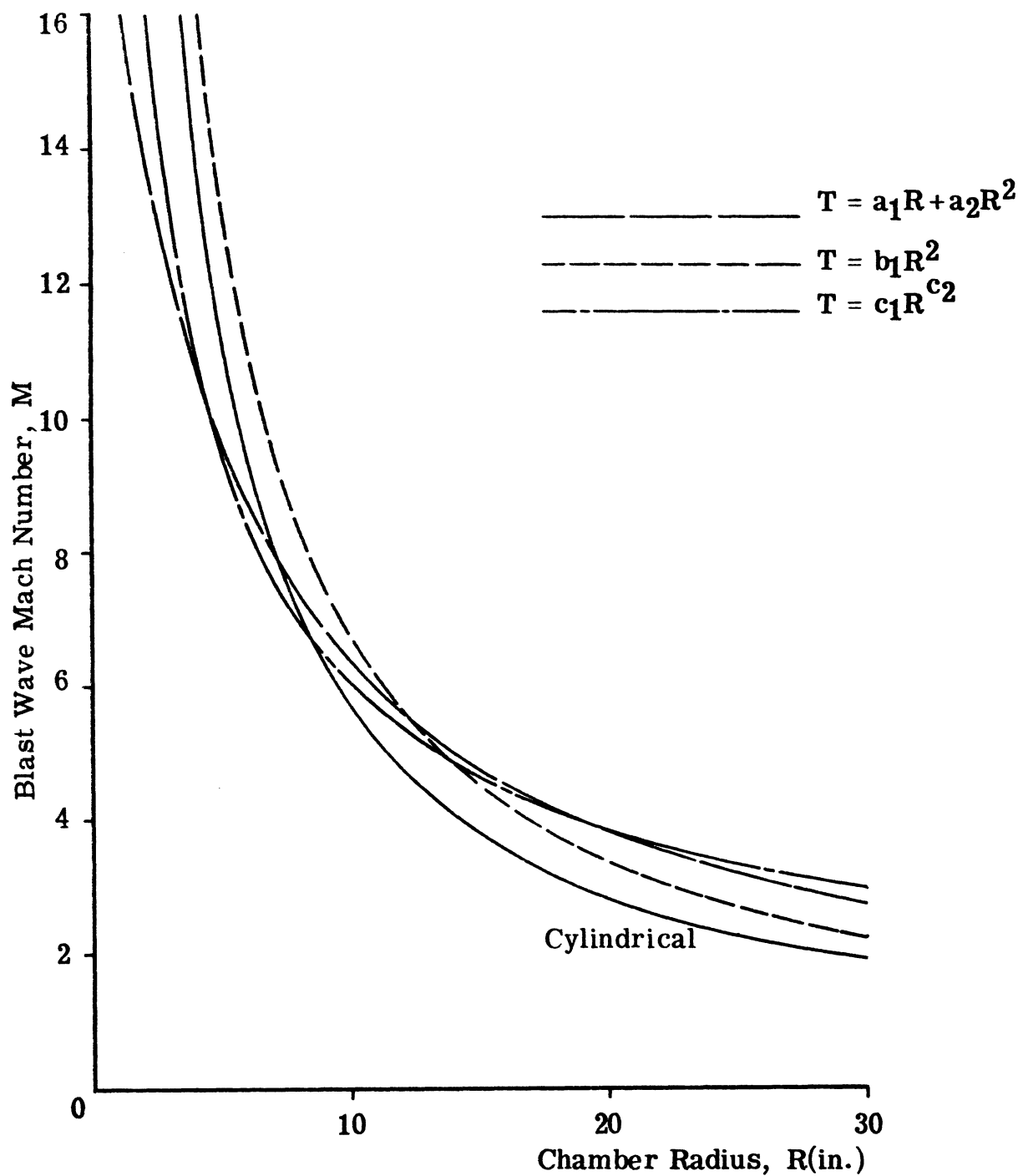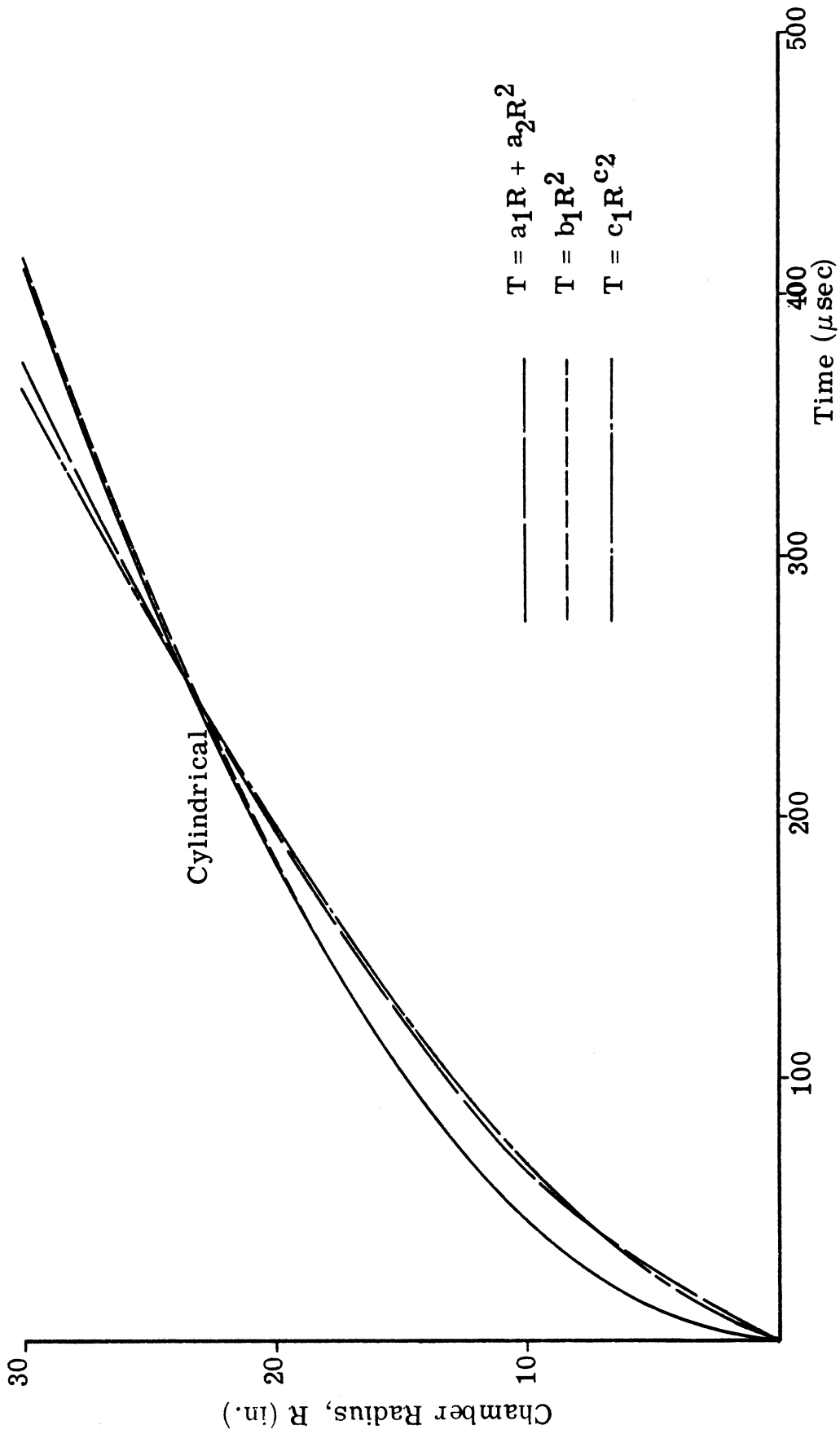
time coordinate was arrived at by a different technique.

Inasmuch as the theoretical curve involves use of an experimentally determined efficiency factor, the influence of this value on predictions was examined. Various polynomial fits to the efficiency data of Figure 19 were assumed and showed little influence on the value of η_e for a given energy level. Further, variations in η_e were assumed and the changes in theoretical blast wave arrival times, wave velocity, and wave Mach number were noted. A 10 percent variation in η_e led to a 3 to 4 percent variation in the latter quantities.

It is concluded that the experiments do exhibit the desired cylindrical behavior and that this characteristic is taken on rather early, say by a radius of 6 inches.

It is anticipated that the blast wave phase of this research will not be terminated completely. Periodically additional runs will be made to gain a good statistical sample for establishing the energy efficiency. Also a comparison of blast wave pressures and possibly heat transfer as functions of radius is planned.

3. Two-Phase Detonation Results

Experiments have been conducted in monodisperse sprays of a highly refined fraction of Kerosene, subsequently referred to as Kerosene 2, the oxidizer was air at atmospheric conditions. At this time the controls exercised upon the conditions of the detonation runs have been limited to

systematic variations in initiation energy, E_O, at a fixed global equivalence

ratio, ϕ_T, for a given fuel. Variations in ϕ_T to investigate the influence

of this parameter upon wave properties are easily accommodated and

this is planned for future experiments. Presently detonation runs have

been made at $\phi_T \approx 0.63$. This figure was calculated on the basis of an

experimentally determined mean drop size of 380 microns. A 5 percent

variation in mean drop size by these calculations produces a 10 percent

variation in ϕ_T.

The liquid fuels used to date and those with which further experiments

are planned are given in Table VIII, along with their more common physical

properties. As expected, the properties of the two kerosene fractions

are very much alike, as are the properties of the two nitropropane types.

In view of this, 1-Nitropropane may be dropped from the experimental

schedule. The Gordon-McBride NASA program which has proved so

useful in the past has been used to derive equivalent gas phase detonation

properties. Plotted in Figures 23, 24, and 25 are these properties for

Kerosene 2, 2-Nitropropane and Propyl Nitrate, respectively. A cursory

comparison of the curves reveals behavioral trends which should be inter-

esting to examine experimentally. Detonation velocities for the two latter

fuels mentioned above tend to effectively plateau for a large range of equiva-

lence ratios. Additionally, the behavior in the pressure ratios of these

same two fuels follows trends considerably different from the fuels which

73
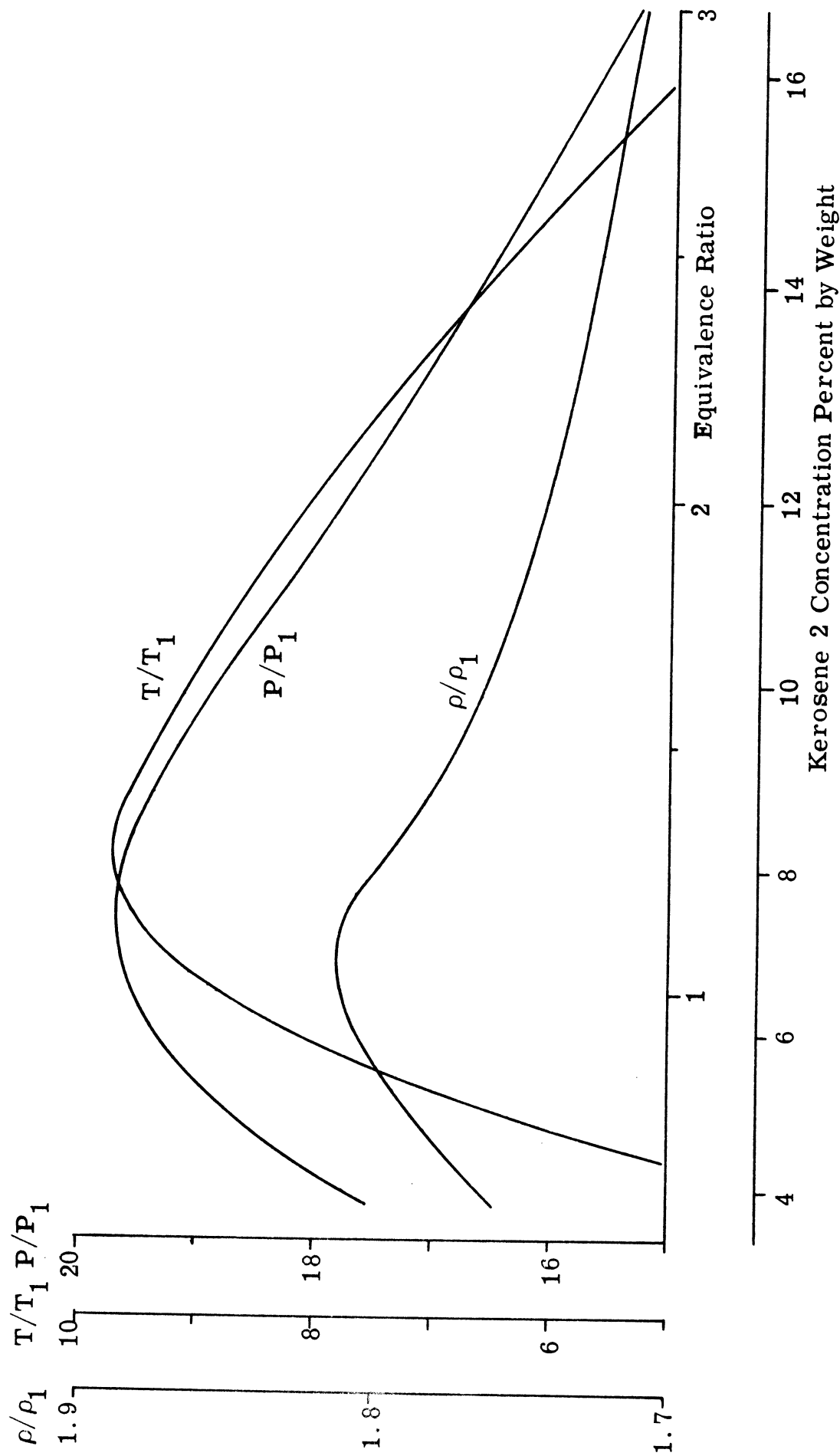
Figure 23(a). Kerosene 2-Air Gas Detonation Parameters.
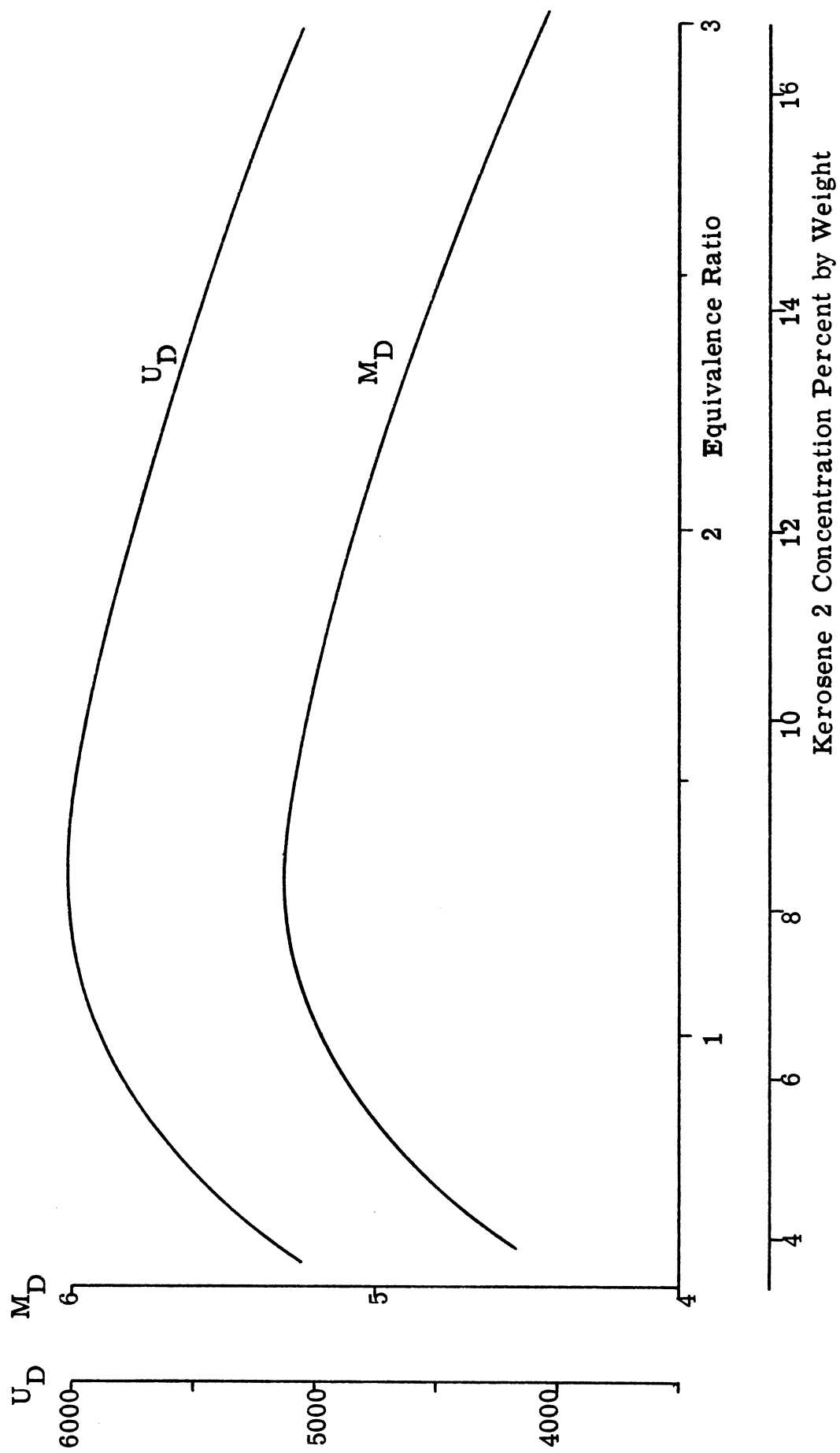
Figure 23(b). Kerosene 2-Air Gas Detonation Parameters.
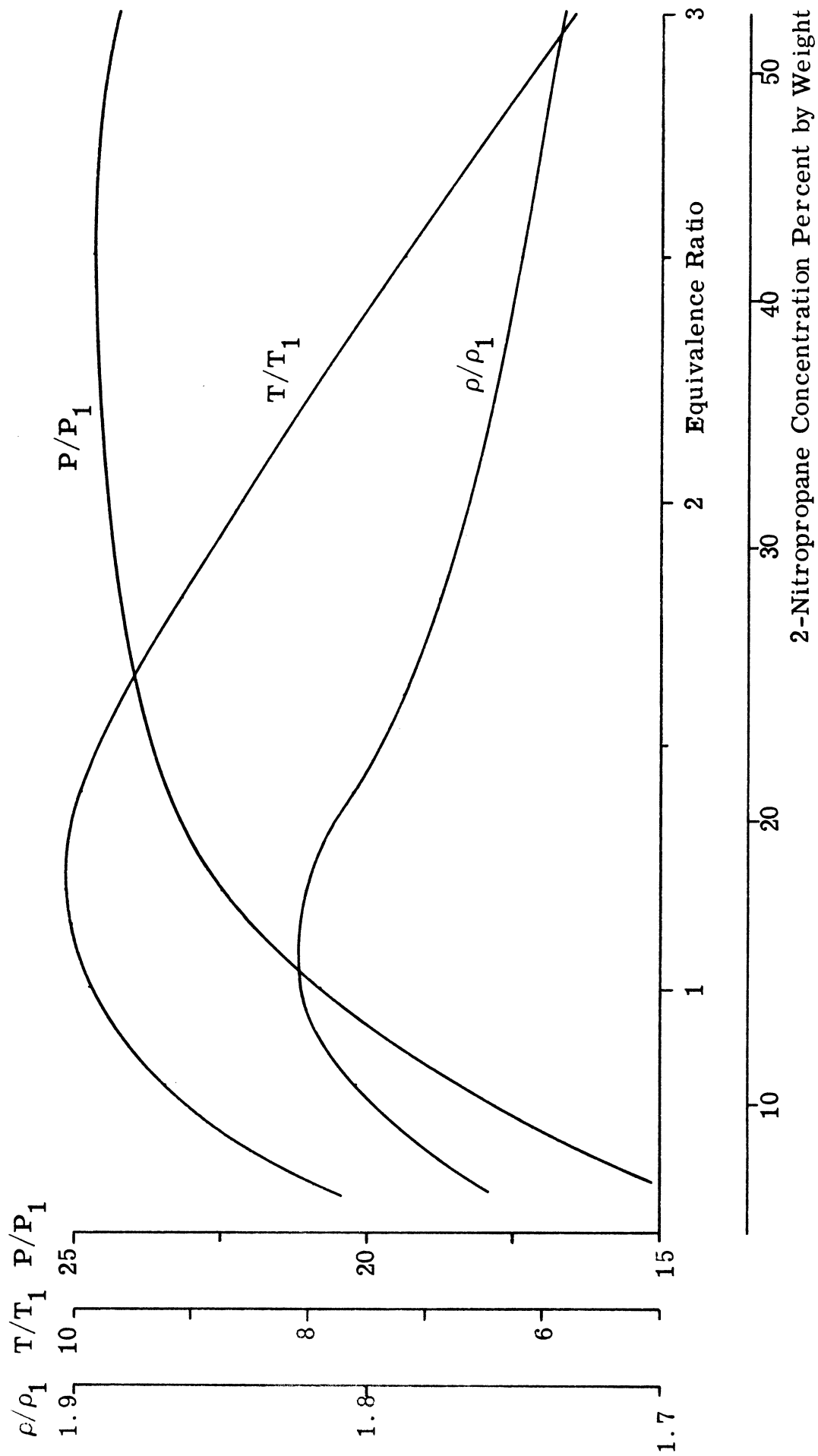
Figure 24(a). 2-Nitropropane-Air Gas Detonation Parameter.

76
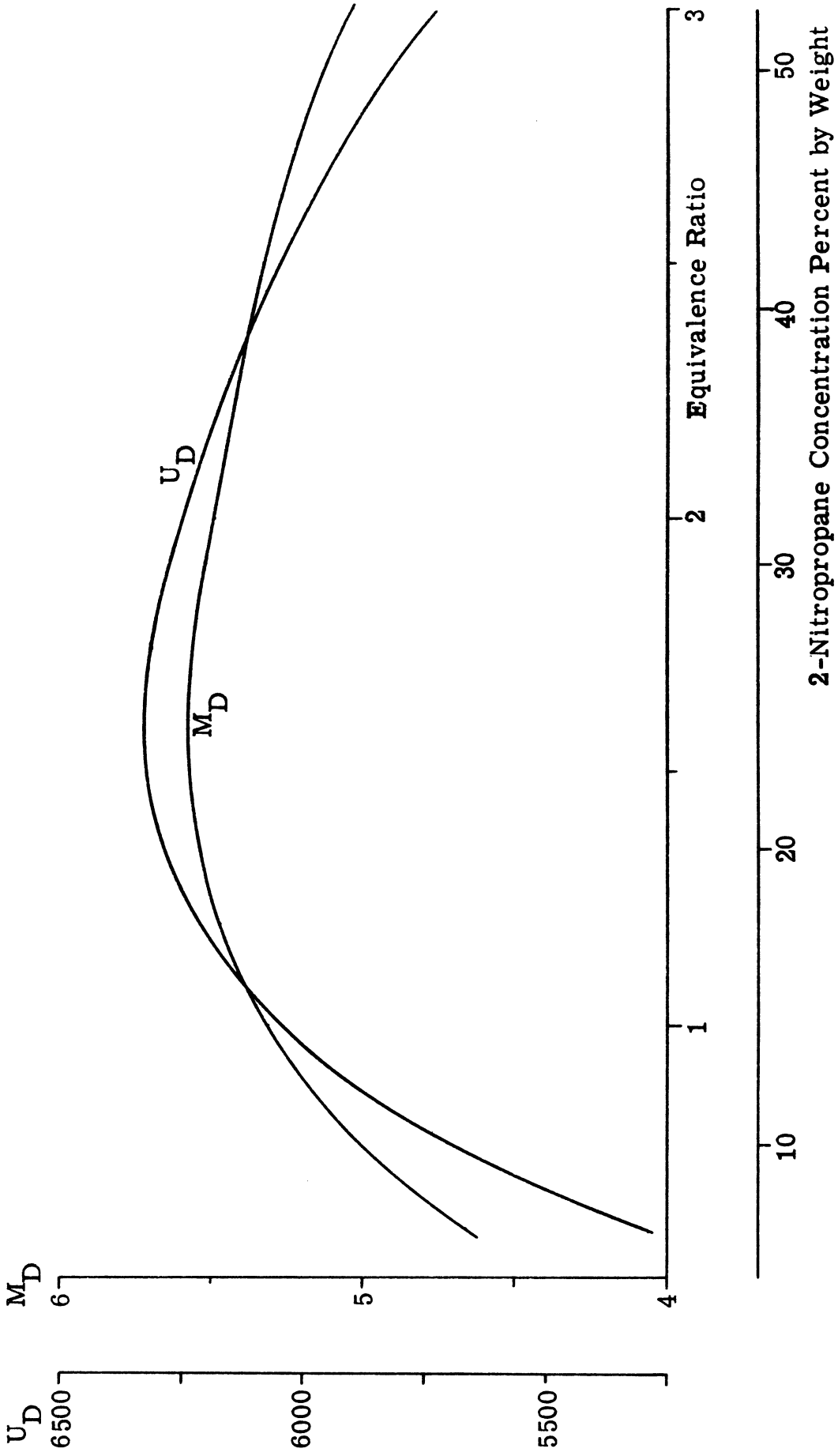
Figure 24(b). 2-Nitropropane-Air Gas Detonation Parameter
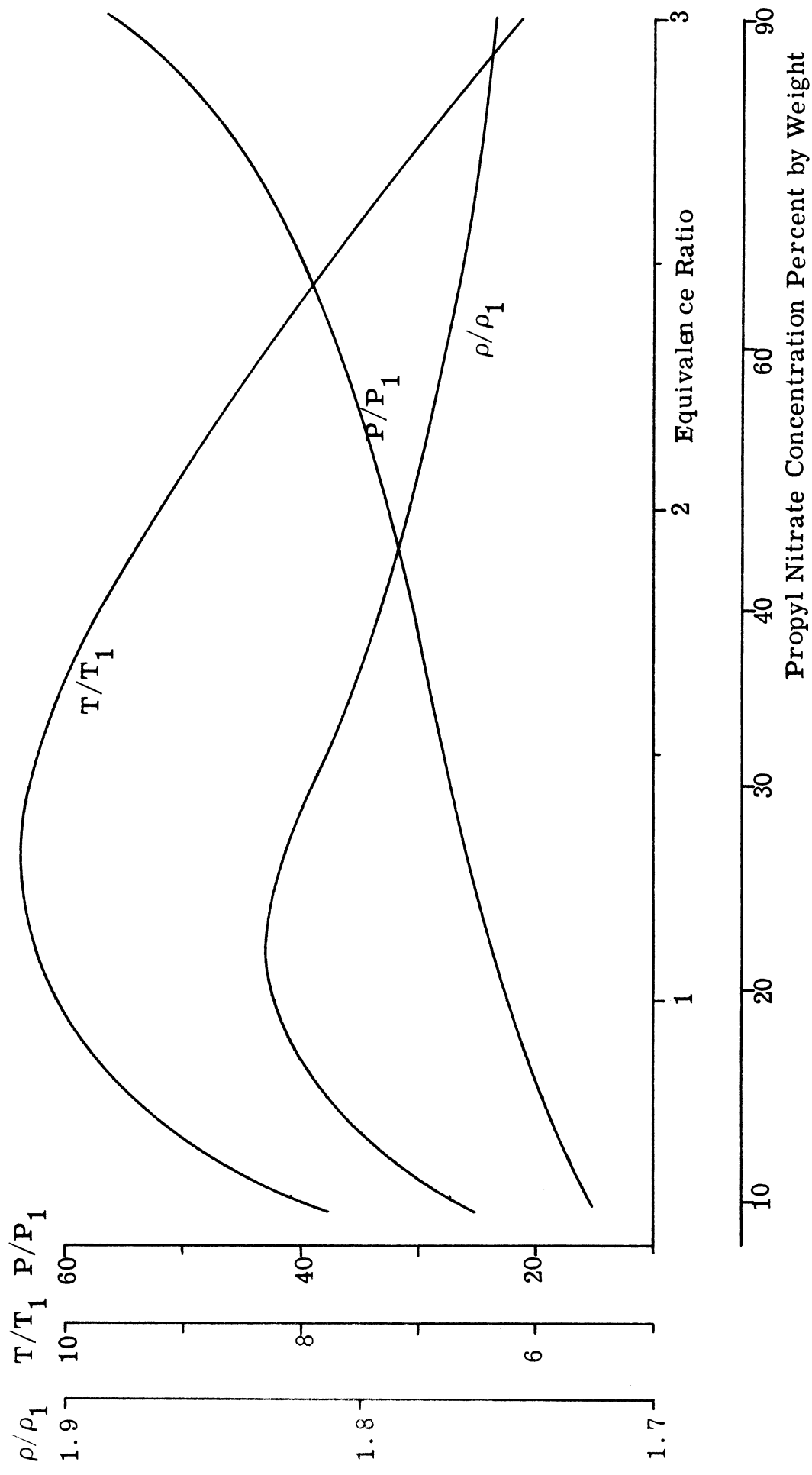
Figure 25(a). Propyl Nitrate-Air Gas Detonation Parameter.

78
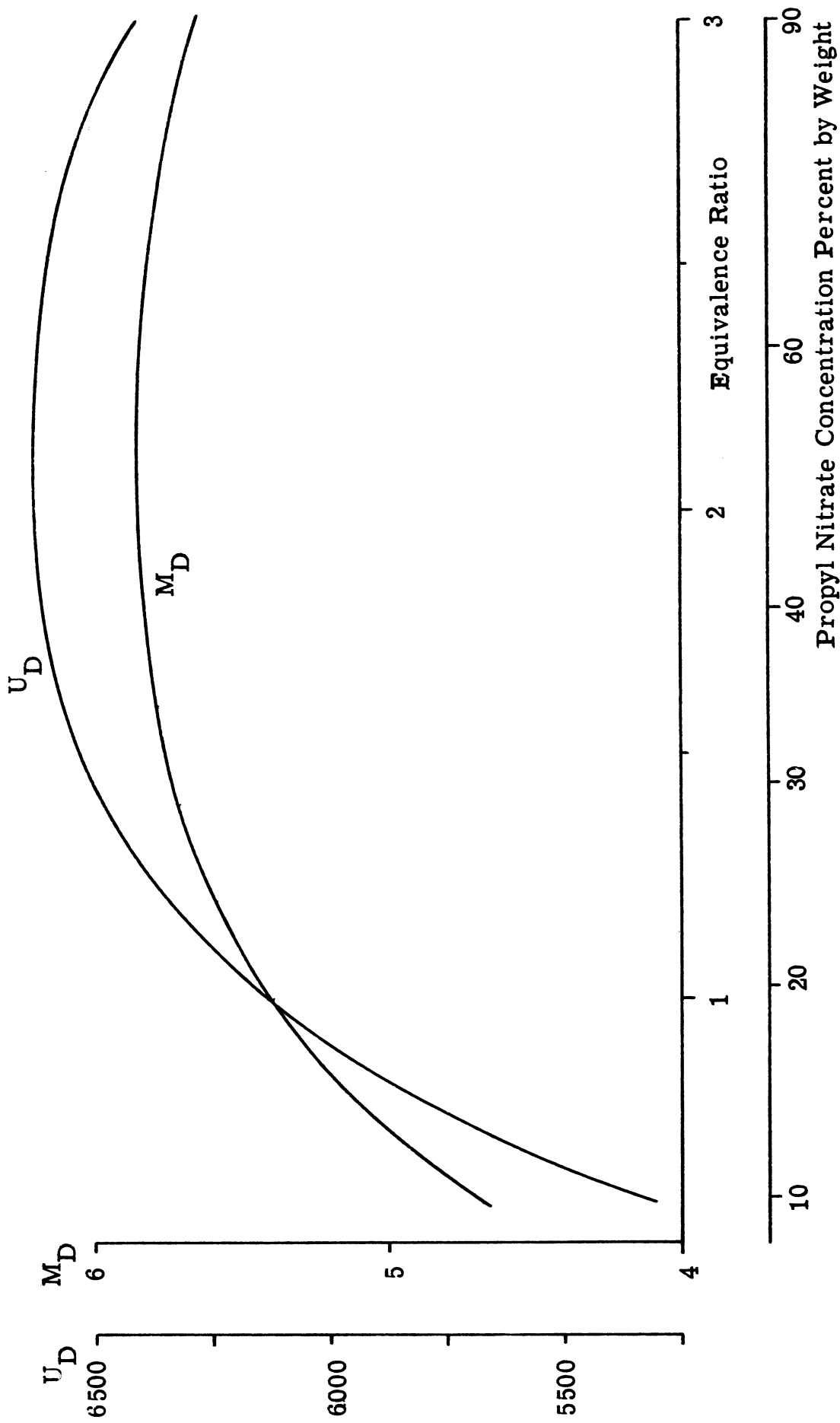
Figure 25(b). Propyl Nitrate-Air Gas Detonation Parameter.

79

TABLE VIII. COMPARISON OF PHYSICAL PROPERTIES OF HYDROCARBON FUELS

	Kerosene 1	Kerosene 2	2-Nitropropane	1-Nitropropane	Propyl Nitrate
Density $(slugs/ft^3)$	1.5281	1.4464	1.9069	1.9305	2.0375
Surface Tension (lb/ft)	2.023×10^{-3}	2.059×10^{-3}	2.393×10^{-3}	2.465×10^{-3}	2.31×10^{-3}
Viscosity $(lb-sec/ft^2)$	5.307×10^{-5}	5.348×10^{-5}	1.573×10^{-5}	1.656×10^{-5}	1.172×10^{-5}
Molecular Weight	177.06	206.8	89.09	89.09	105.09
Composition					
Percent C	86.38	85.38	40.28	40.54	35.02
Percent H	13.75	14.46	7.90	8.28	7.01
Percent N	-	-	15.29	15.10	12.49
Percent O	-	-	36.53	36.08	45.48
Heat of Combustion (cal/gm)	11,220	11,310	5,531	5,462	4,594
Heat of Formation $(cal/gm-mole)$	-68,770	-60,450	-30,340	-35,330	-39,320
Stoichiometric Equivalence Ratio $(O_2$ basis)	0.292	0.292	0.743	0.743	0.989

are currently being examined. Pressure ratio behavior of this type is

partially due to the increased amounts of oxygen present in the reaction.

Reduction of the experimental detonation data proved it to be very

self-consistent and in substantiating agreement with that reported upon

previously. Figures 26 and 27 are characteristic radius-time plots of

detonation data at varying energy levels for Kerosene 1 and Kerosene 2.

These plots demonstrate the general form of the rough data as well as the

currently employed fourth order polynomial fit to this data. The reason

for selecting a fourth order polynomial was simply that it tended to reflect

wave properties sufficiently well:

1. Slope of r-t plot beyond r_* is generally constant for appropriate

    energies, if low frequency polynomial generated oscillations

    are ignored.

2. Constant detonation velocity is predicted for energies above

    the critical threshold energy.

3. Decaying detonation velocity is predicted for energies below

    the critical threshold energy.

4. Critical radii is predicted with remarkable accuracy.

5. Detonation velocity similarly predicted with remarkable accuracy.

This technique, however, does possess many disadvantages, none the

least of which is a lack of sensitivity to variations in wave velocity. Con-

sequently, work on an alternate detonation data regression model was

Figure 26(a). Kerosene 1-Air Detonation Data, 0.5 gram

Figure 26(b). Kerosene 1-Air Detonation Data, 1.5 grams
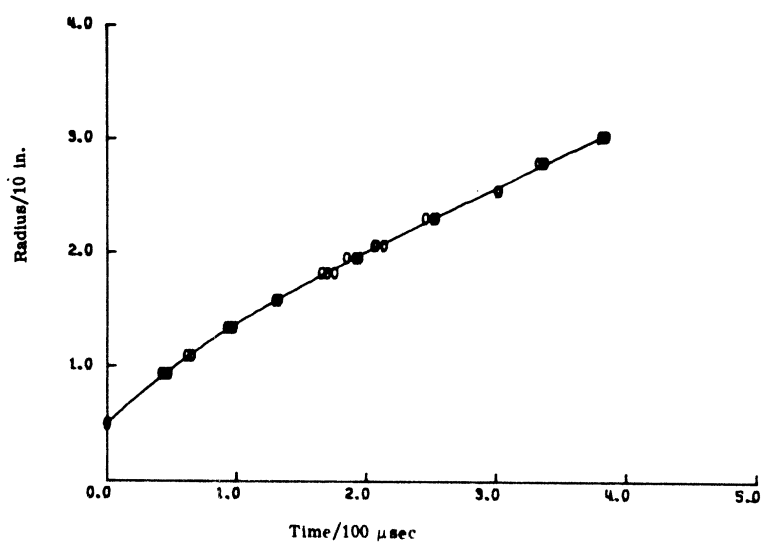
Figure 26(c). Kerosene 1-Air Detonation Data, 2.5 grams
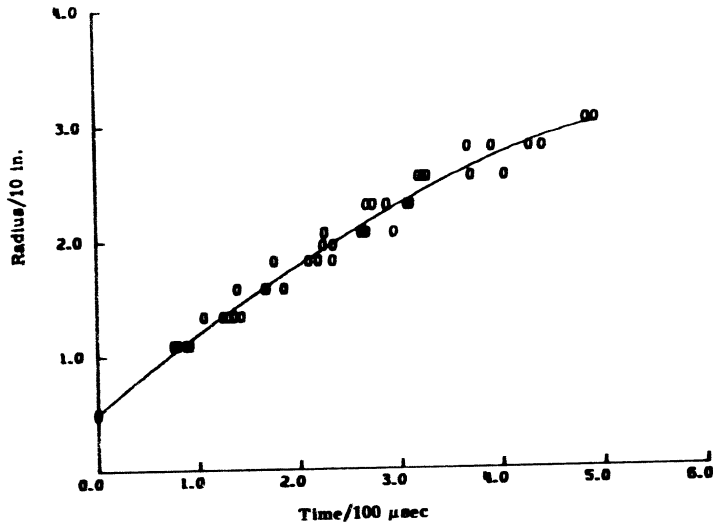
Figure 27(a). Kerosene 2-Air Detonation Data, 0.5 gram
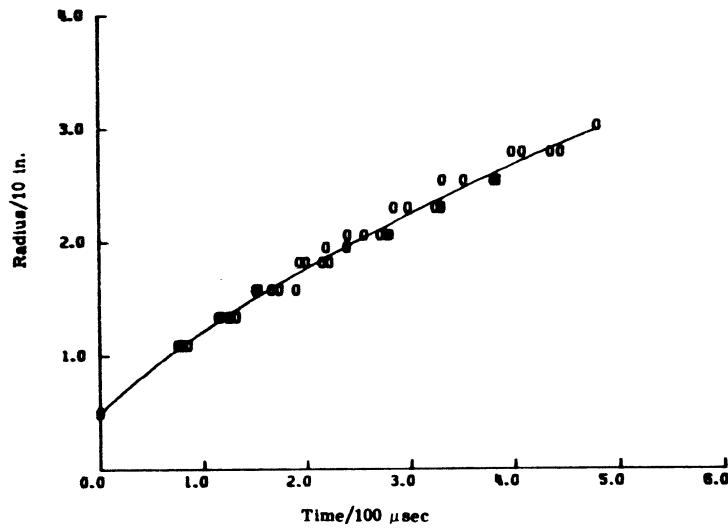
Figure 27(b). Kerosene 2-Air Detonation Data, 0.75 gram
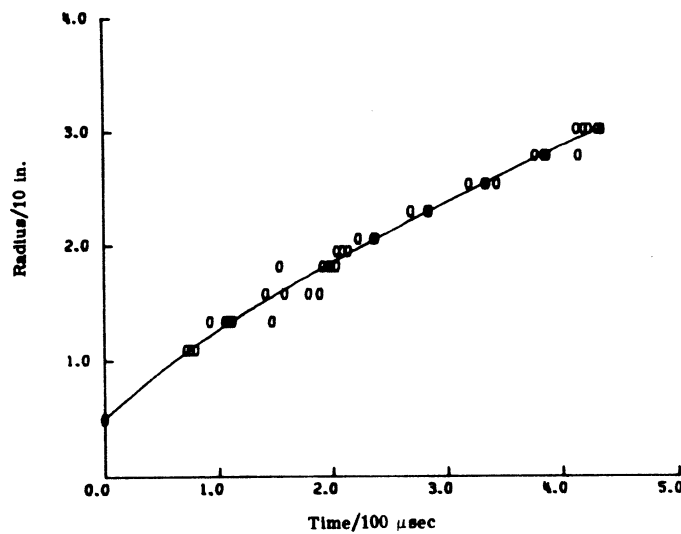
Figure 27(c). Kerosene 2-Air Detonation Data, 1.0 gram
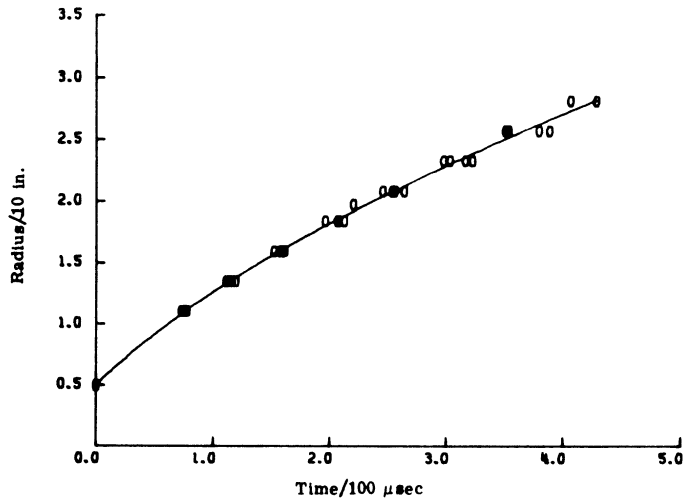
Figure 27(d). Kerosene 2-Air Detonation Data, 1.25 grams
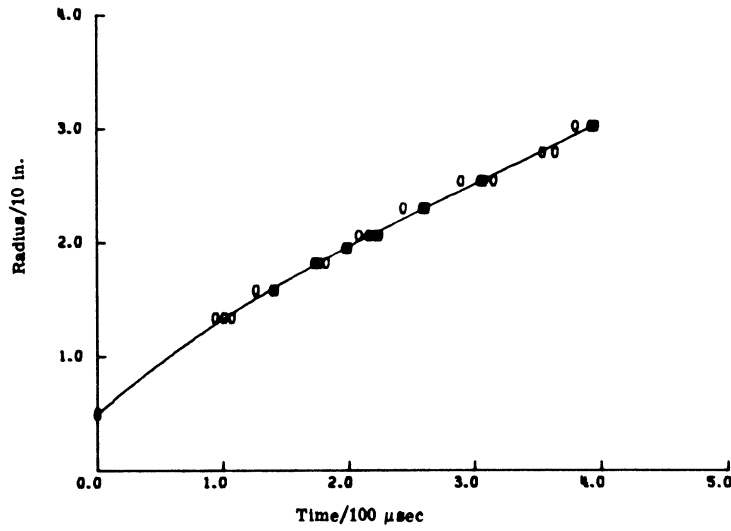
Figure 27(e). Kerosene 2-Air Detonation Data, 1.5 grams
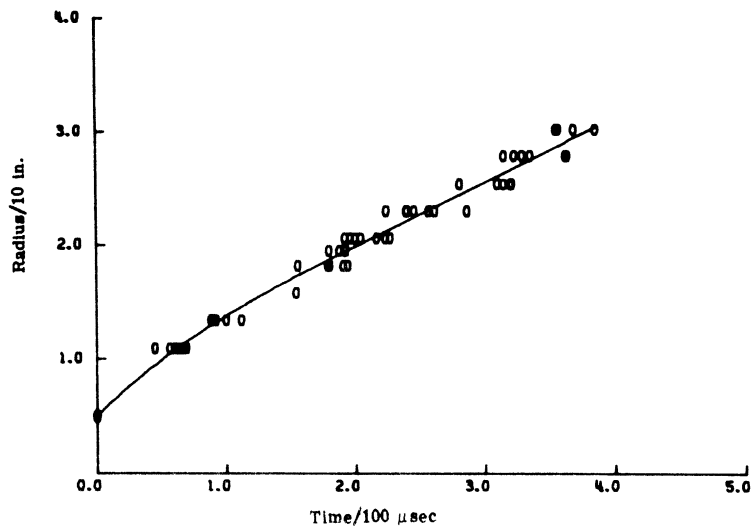
Figure 27(f). Kerosene 2-Air Detonation Data, 2.0 grams
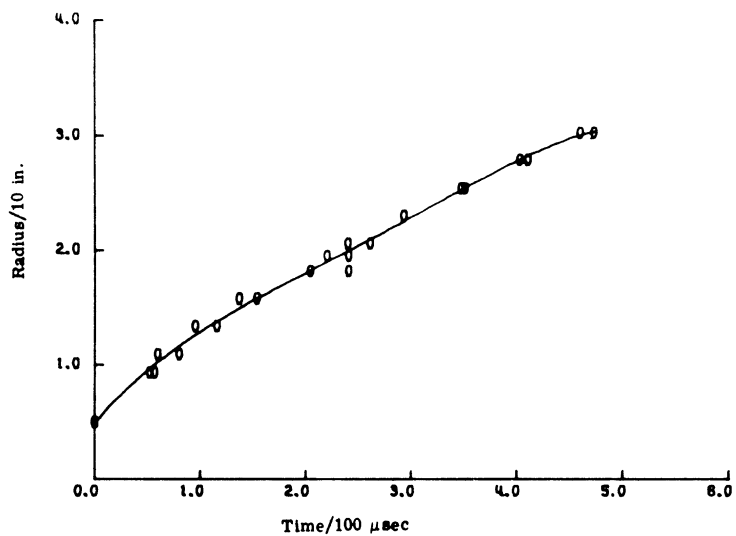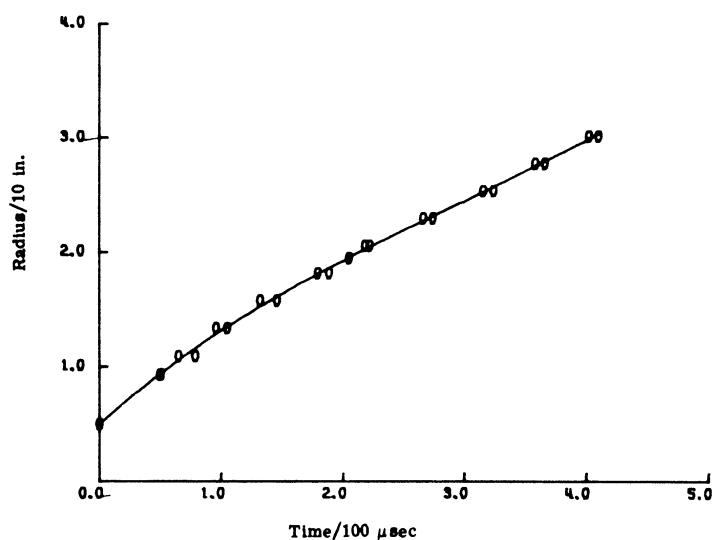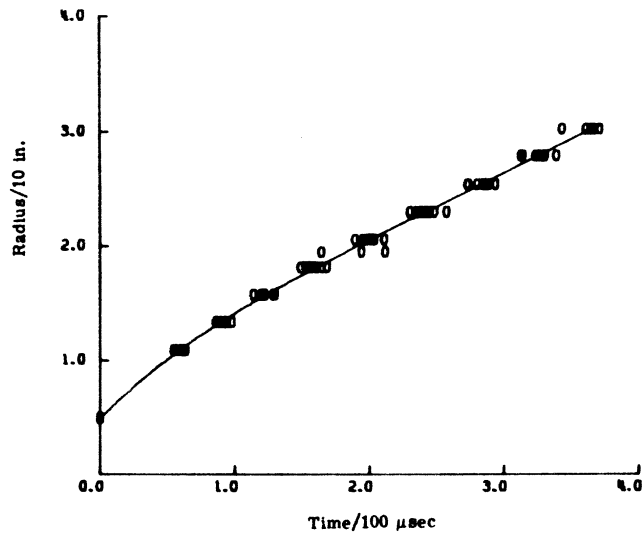
Figure 27(g). Kerosene 2-Air Detonation Data, 2. 5 grams
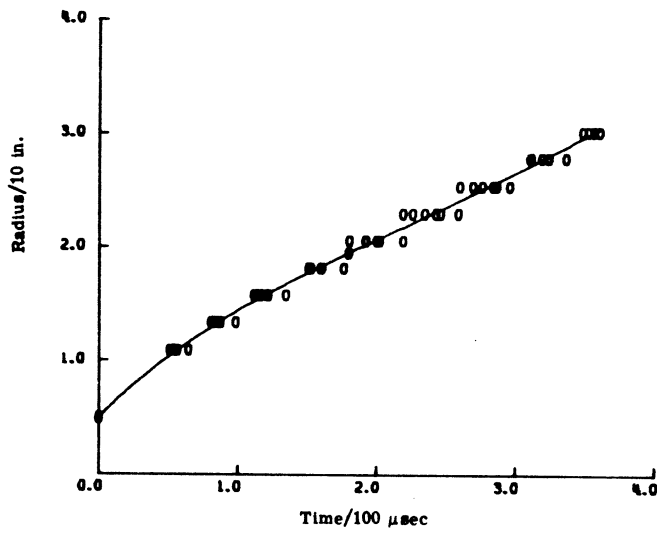
Figure 27(h). Kerosene 2-Air Detonation Data, 3. 0 grams
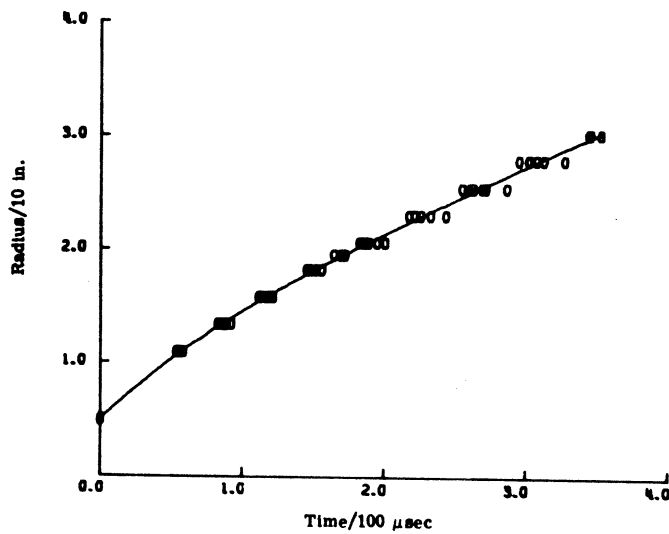
Figure 27(i). Kerosene 2-Air Detonation Data, 3. 5 grams

undertaken. This regression model, which is not yet completed, makes use of the method of LaGrange multipliers to minimize the standard deviation of a least squares curve fit of rough experimental radius-time data to the following:

$$T_i = \alpha_0 + \alpha_1 R_i + \alpha_2 R_i^2 + \epsilon_i \qquad \text{for } R_i < r_*$$

and

$$T_i = \beta_0 + \beta_1 R_i + \epsilon_i \qquad \text{for } R_i \geq r_*$$

(39)

The problem is then to compute the constant coefficients α_0, α_1, α_2, β_0, β_1, and the critical radii r_* in order to minimize the standard deviation subject to the constraints that at $R_i = r_*$

$$\alpha_0 + \alpha_1 r_* + \alpha_2 r_*^2 = \beta_0 + \beta_1 r_*$$

and

$$\alpha_1 + 2\alpha_2 r_* = \beta_1$$

(40)

The primary advantages to this model are the greater reliability in the derived critical radii values and the well behaved continuous nature of the final function $T = T(R)$. The latter point will allow for a more representative continuous record of wave propagation velocity.

Figure 28 demonstrates the current technique for obtaining detonation wave propagation velocity and critical radii. Displayed in Figure 29 and Table IX are the basic results for Kerosene 1. Figure 29 is a plot of two-phase detonation velocity as a function of equivalence ratio and drop size. The predicted theoretical two-phase velocity was determined by modifying the equivalent gas phase velocity by a mean velocity deficit.
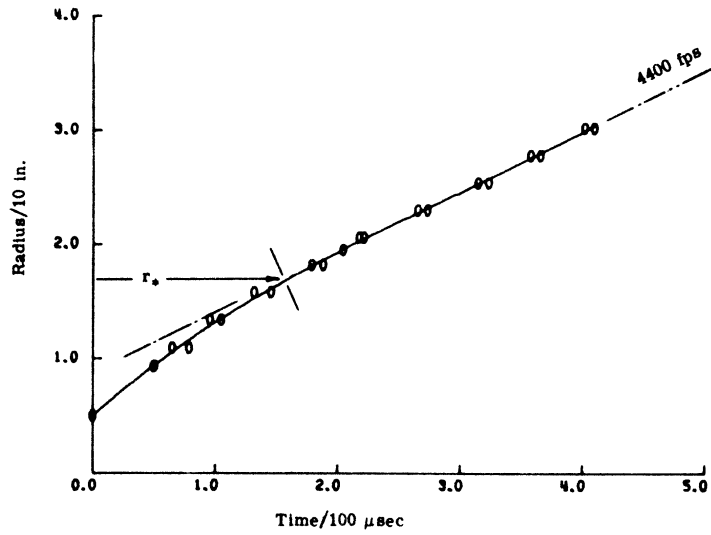
Figure 28(a). Data Reduction Technique, 1.5 grams
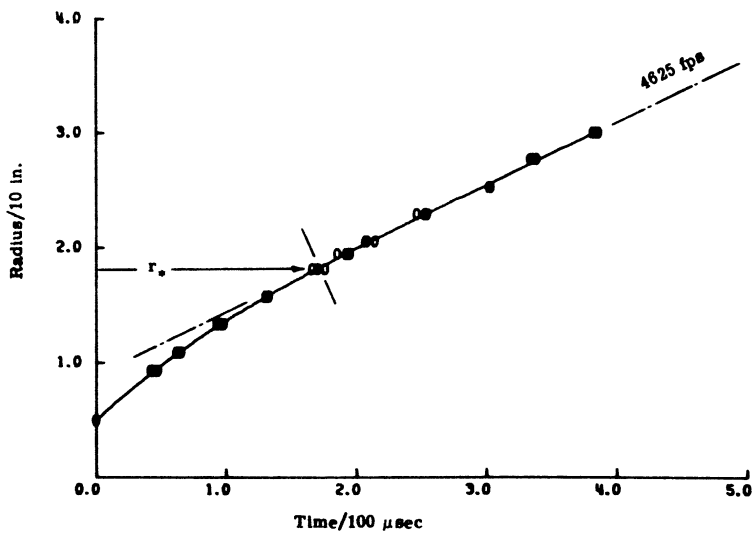
Figure 28(b). Data Reduction Technique, 2.5 grams
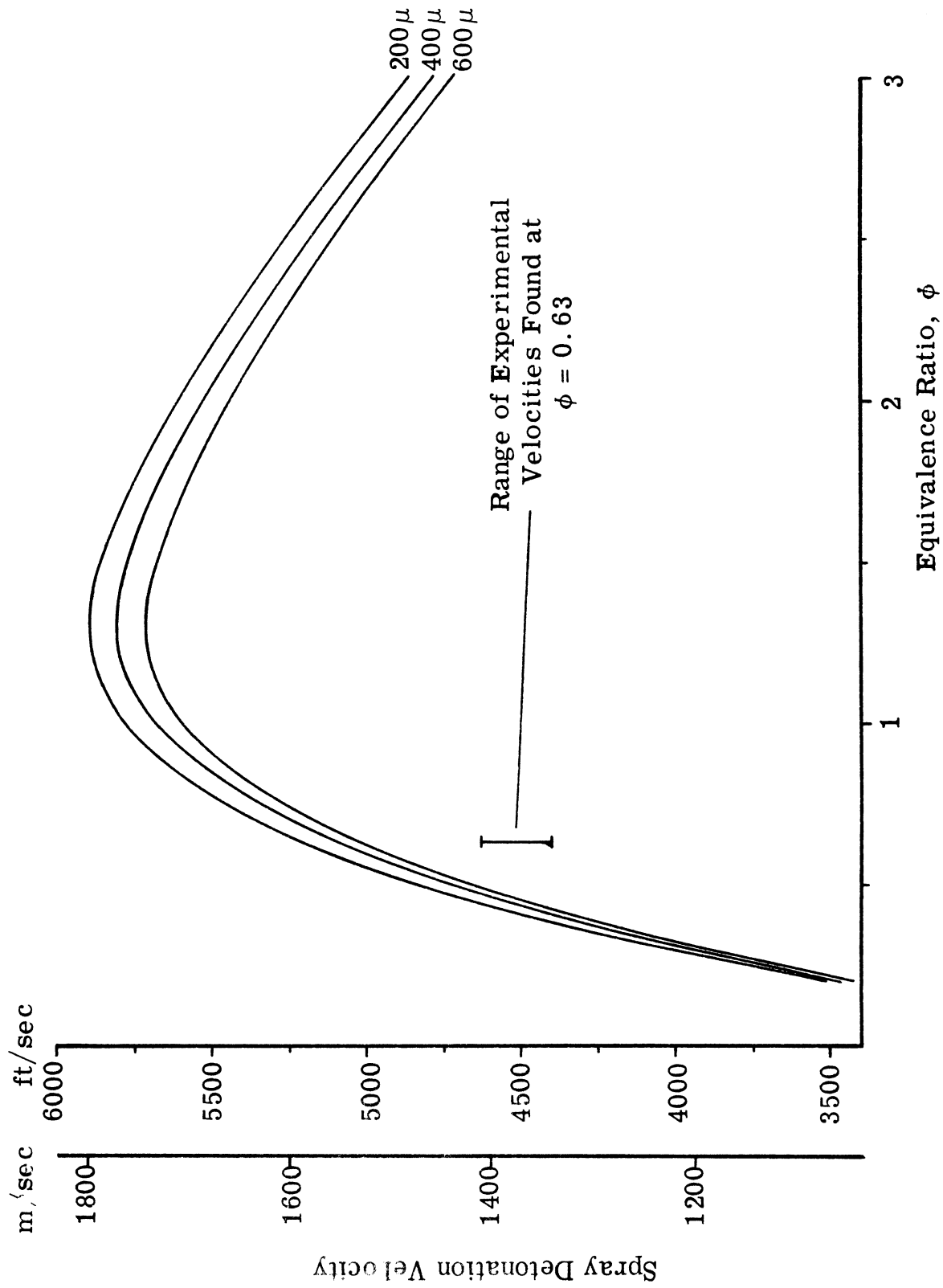
Figure 29. Spray Detonation Velocity for Kerosene 1 as a Function of Equivalence Ratio and Drop Size.

TABLE IX. EXPERIMENTAL TWO-PHASE DETONATION RESULTS FOR KEROSENE 1.

Explosive Charge grams	Detonation Velocity ft/sec	Detonation Mach No.	Percent Difference [a]	r_{*exp}	r_{*theo} [b]	Percent Difference
2.5	4625	4.07	9.5	18.5	18.44	- 0.33
1.5	4400	3.87	13.9	17.3	16.36	- 5.74

[a] Based upon theoretical two-phase detonation velocity of 5110 ft/sec.

[b] Computed using energy adjusted by energy efficiency factors.

89

Recall that velocity deficit is a function of drop size, chamber hydraulic

radius, fuel, and oxidizing medium. The mean or average velocity deficits

used in the determination of kerosene spray velocity were computed to be

1.44%, 2.88% and 4.32% for 200 μ, 400 μ and 600 μ drop sizes,respectively.

The experimental values of spray velocity and critical radii are given. The

results appear quite satisfactory. Similarly, Figure 30 and Table X give

the detonation results for Kerosene 2. The comparison between experi-

ment and theory proved to be even more satisfactory than with Kerosene 1.

Definite trends in this comparison are now beginning to show up. Basically,

the difference between experiment and theory becomes wider as the explo-

sive charge is decreased toward the ignition threshold energy. This holds

true for velocity as well as critical radii data for both kerosene fractions.

Figure 31 displays in a more transparent fashion the fundamental

wave behavior of a Kerosene 2- air detonation as a function of chamber

radial distance and explosive charge. The continuous and expected decay

patterns of the curves up to the critical radii are clearly noticeable. The

trends depicted here are in contrast, but not necessarily in disagreement,

with those reported upon in Figure 48 of the previous annual report[1].

The dissimilar decay trends reported upon therein suffered by virtue of

the fact that no mathematical regression model was available with which to

describe the experimental detonation data. Consequently, velocities were

obtained by taking slopes of radius-time data curves by observation. Such
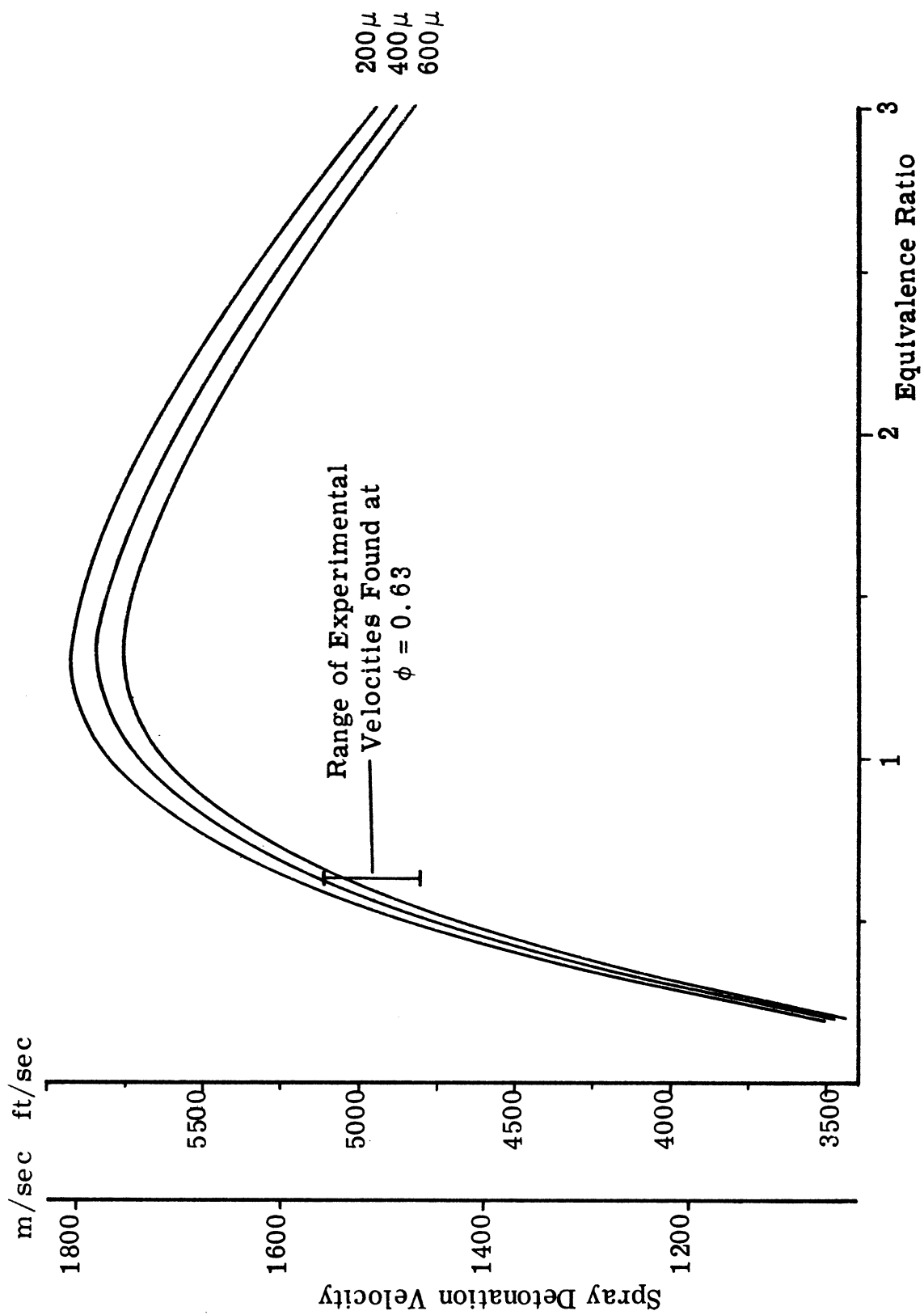
Figure 30. Spray Detonation Velocity for Kerosene 2 as a Function of Equivalence Ratio and Drop Size.

91
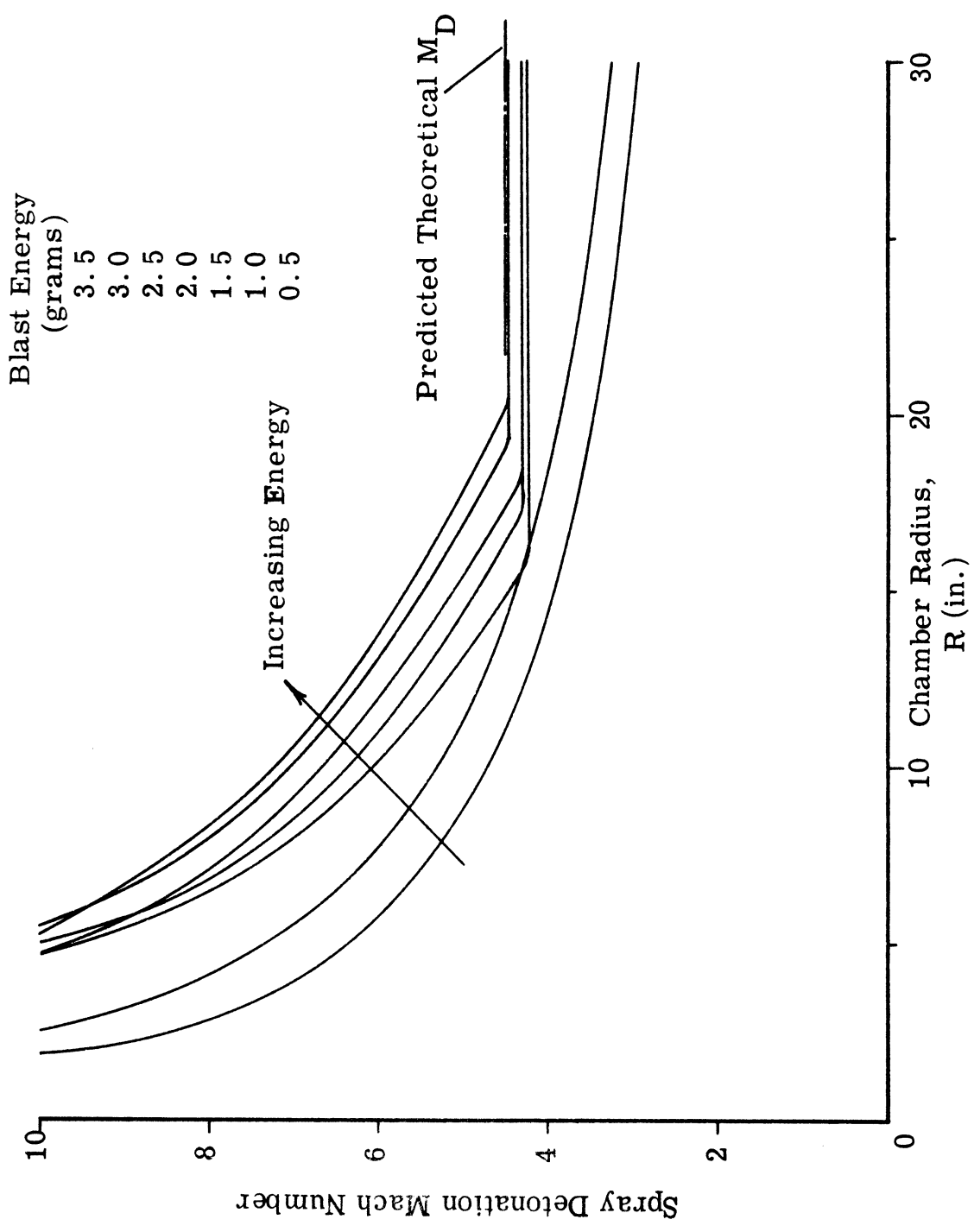
Figure 31. Experimental Two-Phase Detonation Mach Number as a Function of Initiation Energy and Chamber Radius for Kerosene 2 (ϕ = 0.63).

TABLE X. EXPERIMENTAL TWO-PHASE DETONATION RESULTS FOR KEROSENE 2.

Explosive Charge grams	Detonation Velocity ft/sec	Detonation Mach No.	Percent Difference[a]	r_{*exp} in.	r_{*theo}[b]	Percent Difference
3.5	5106	4.50	0.30	20.3	20.3	0.0
3.0	5090	4.48	0.60	19.2	19.31	0.57
2.5	4900	4.32	4.30	18.2	18.44	1.30
2.0	4800	4.23	6.30	17.2	17.51	1.77
1.5	4800	4.23	6.30	15.8	16.41	3.72

[a]Based upon theoretical two-phase detonation velocity of 5120 ft/sec.

[b]Computed using energy adjusted by energy efficiency factors.

a technique can hardly help but introduce artificial trends and inaccuracies into the data. The recently developed detonation regression model addresses itself to the solution of this problem. Since this model is not presently available to produce, among other things, statistically accurate Mach number-radius behavior, and a return to the old technique is not desirable, an alternate method for generating such data was devised.

It was felt that it would be instructive to use strong blast wave experimental data to assist in the representation of the beginning of the blast-initiated detonation process. The strong blast and strong blast-initiated detonation processes initially have identical decay trends. Hence, the detonation process should follow the strong blast process on an M-r plot until the energy released by the detonation is significant enough to cause a modifying effect upon the strong blast decay trend. By making use of such a representation,it was thus felt that preliminary trends in the modified character of the blast wave decaying process due to the presence of the detonation could be observed. It should be made clear that this technique is only a temporary representation of the data until use can be made of the detonation regression model. At that time observations made here will be pursued further.

The curves of Figure 31 were constructed by generating an experimental M-r curve at the desired energy and then modifying it to conform to the experimental critical radii—detonation Mach number at the selected

energy. During the construction of these curves it was observed that the experimental blast wave rate of decay quickened with increasing energy. Hence, the deviation of the detonation from that of strong blast wave M-r behavior was increasingly more evident as energy was increased. This deviation is primarily due to the fact that while blast wave velocity decays faster with increasing energy, the critical radii for detonation increases. It was further observed that at the critical threshold energy for Kerosene 2 (approximately 1.5 grams) the experimental blast wave datum curve nearly passed through the critical radii-detonation Mach number intersection. It would appear from this crude representation that the larger the blast energy used to detonate a fuel, the quicker the attendent blast decay and the sooner the energy released by the detonation process has a modifying effect upon this decay. All this occurs subject to the additional requirement that the proper critical radii-detonation Mach number constraint is satisfied at each energy level.

The general form of the experimental M-r curves of Figure 31 then presents the picture of a wave process initially dominated, but slightly modified, by the generally characteristic decay of a strong cylindrical blast to an energy dependent critical distance. At this critical point an abrupt transition to a detonation dominated wave process occurs. A dependency of the final detonation velocity upon the initiation energy appears to show up to some degree in these curves. At this time, however,

such a dependency can only be conjecture in view of the error tolerances associated with the data reduction technique used to obtain these curves. Many such dependencies should be more thoroughly established with the subsequent use of the detonation regression model.

Plotted in Figure 32 is critical radii as a function of calculated energy. Two analytic curves appear with experimental points for both kerosene fractions superimposed. The upper curve is critical radii computed as a function of energy by

$$r_* = \left(\frac{E_o}{\pi \, \rho_1 Q}\right)^{1/2} \tag{41}$$

where 100 percent of E_o calculated is used. The lower curve is critical radii computed by Equation (41) where E_o is altered by blast wave energy efficiency discussed earlier. The results are most striking, since a remarkable agreement occurs between an analytically determined r_* and experimental values. The same value of $P_3/P_1 = 12.55$ was used to compute Q for both kerosene fractions, thus making possible the representation of experimental r_* values on the same plot.

4. Gas-Phase Detonation Results

Experiments have been conducted in gaseous MAPP-air mixtures. Experimental runs were made in these mixtures for a constant pressure of 1 atmosphere and atmospheric temperatures ranging from $19.0^{\circ}C$ to $25.7^{\circ}C$. The controls exercised upon the conditions of the detonation
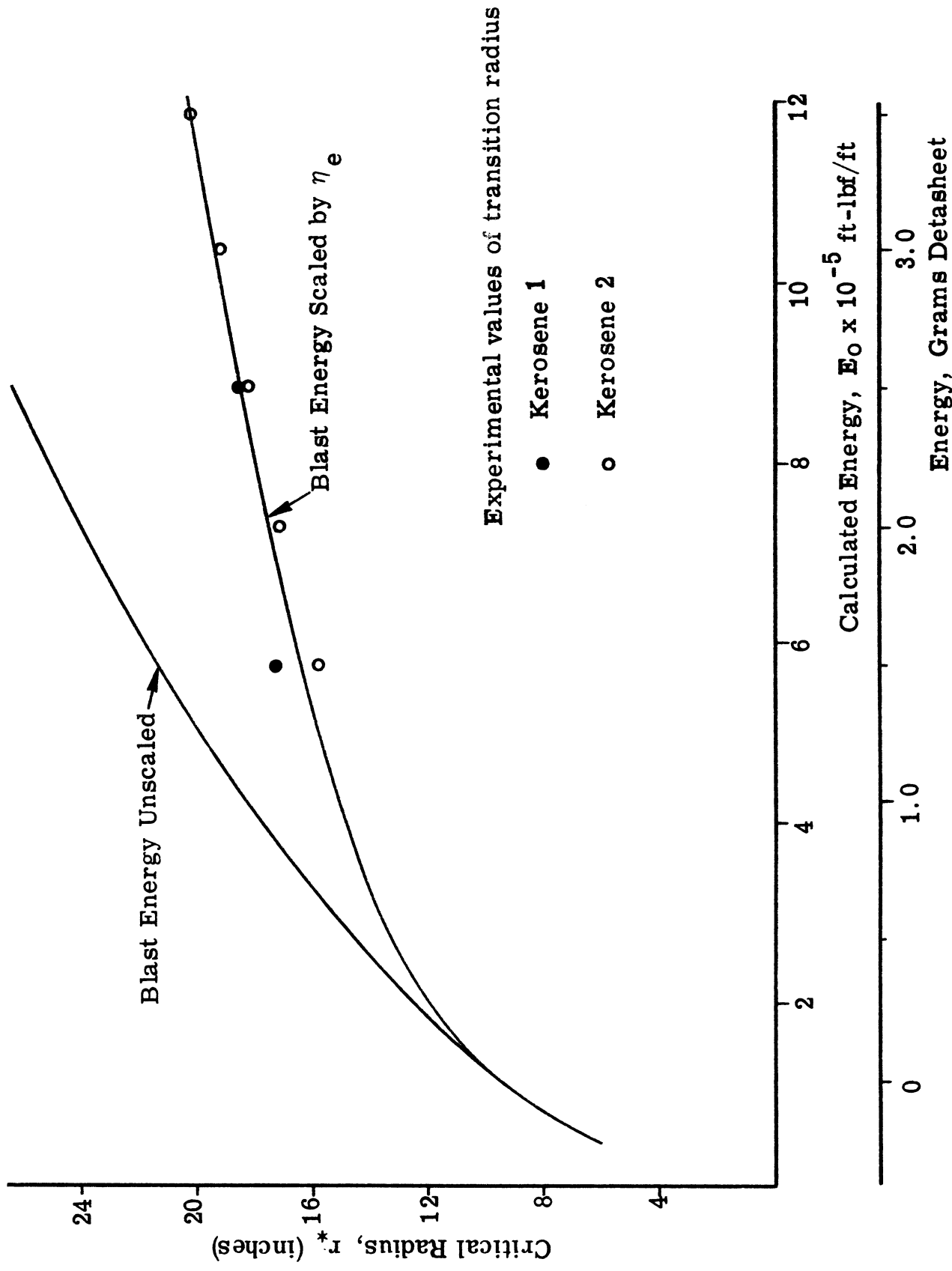
Figure 32.   Critical Ignition Distance as a Function of Energy for Kerosene 1 and Kerosene 2.

97

runs were over a broader range than those presently exercised upon the two-phase detonation runs. Experimental data on wave propagation as a function of radius was obtained for a systematic variation of initiation energy at each of eight different equivalence ratios as given in Table VI.

It was deemed necessary to establish the composition of the MAPP-gas used for the detonation tests. Consequently, a gas chromatographic analysis was performed upon several samples of the pure gas as well as upon the eight MAPP-air mixtures. The analysis was performed upon a Varian 90-C gas chromatograph with the conditions specified in Table XI.

Figures 33 and 34 give examples of gas chromatograms produced by the analysis. As is apparent from the chromatograms, separation of the constituents was very well defined despite the fact that they were very nearly of the same molecular weight. Figure 33 is a chromatogram for pure MAPP, while Figure 34 is for a 10 percent MAPP-air mixture. The jump in the base line between air and propane is due to a scale change necessary to keep the traces on scale. Table XII lists the significant properties of the MAPP gas used during the tests. Once established these properties were used as input data to obtain characteristic gas detonation parameters from the previously mentioned NASA program. Given in Figure 35 are plots of these parameters. An anomalous density ratio behavior shows up for equivalence ratios nearing 3.0. The primary reason for this is due to the appearance of solid carbon in the combustion products.

Propane   Propadiene   Methyl
                          Acetylene
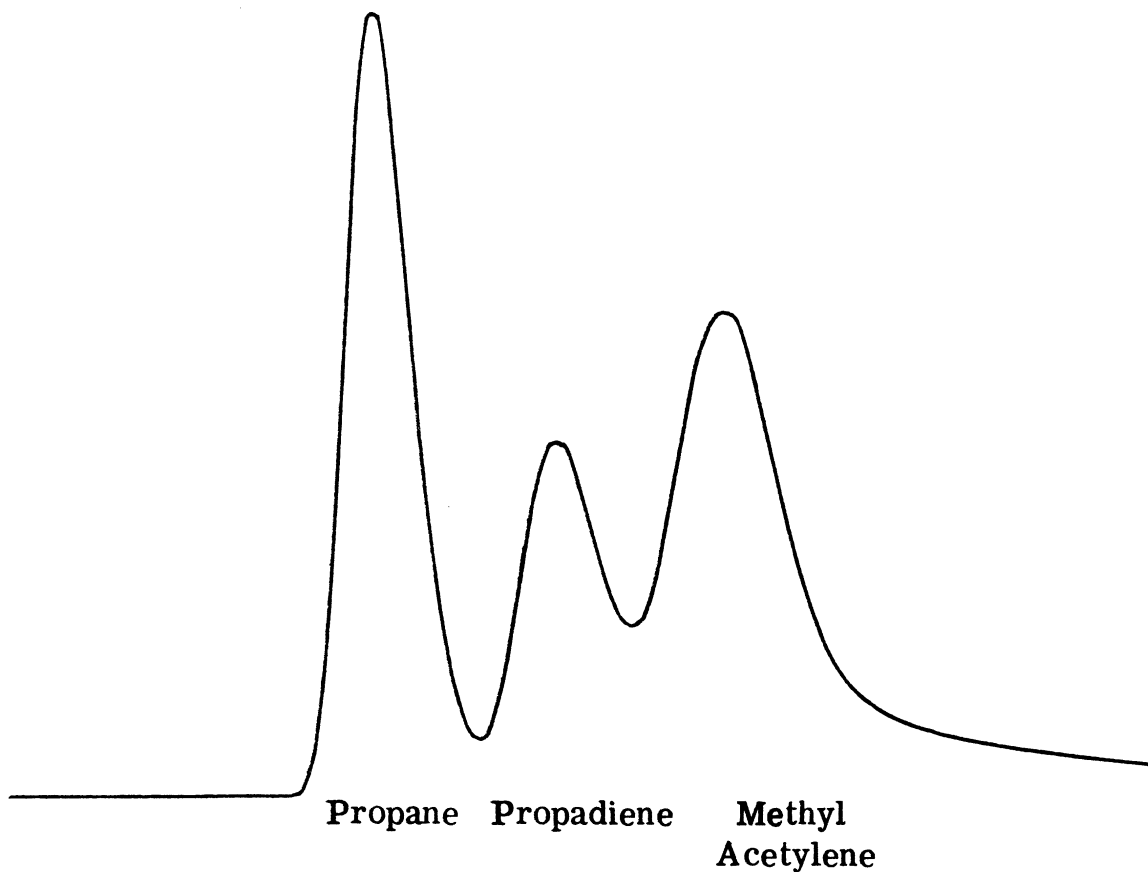
Figure 33. MAPP Gas Chromatogram.

Air   Propane   Propadiene   Methyl
                                         Acetylene
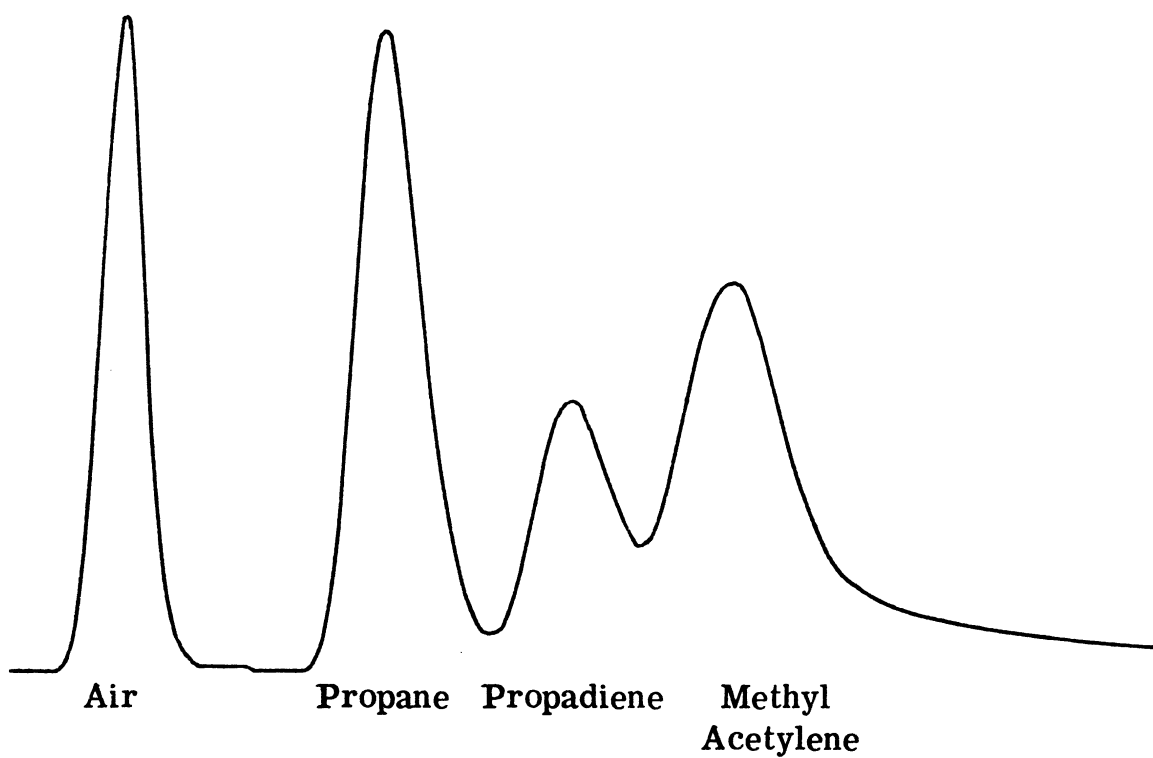
Figure 34. MAPP-Air Gas Chromatogram (10% MAPP).

99
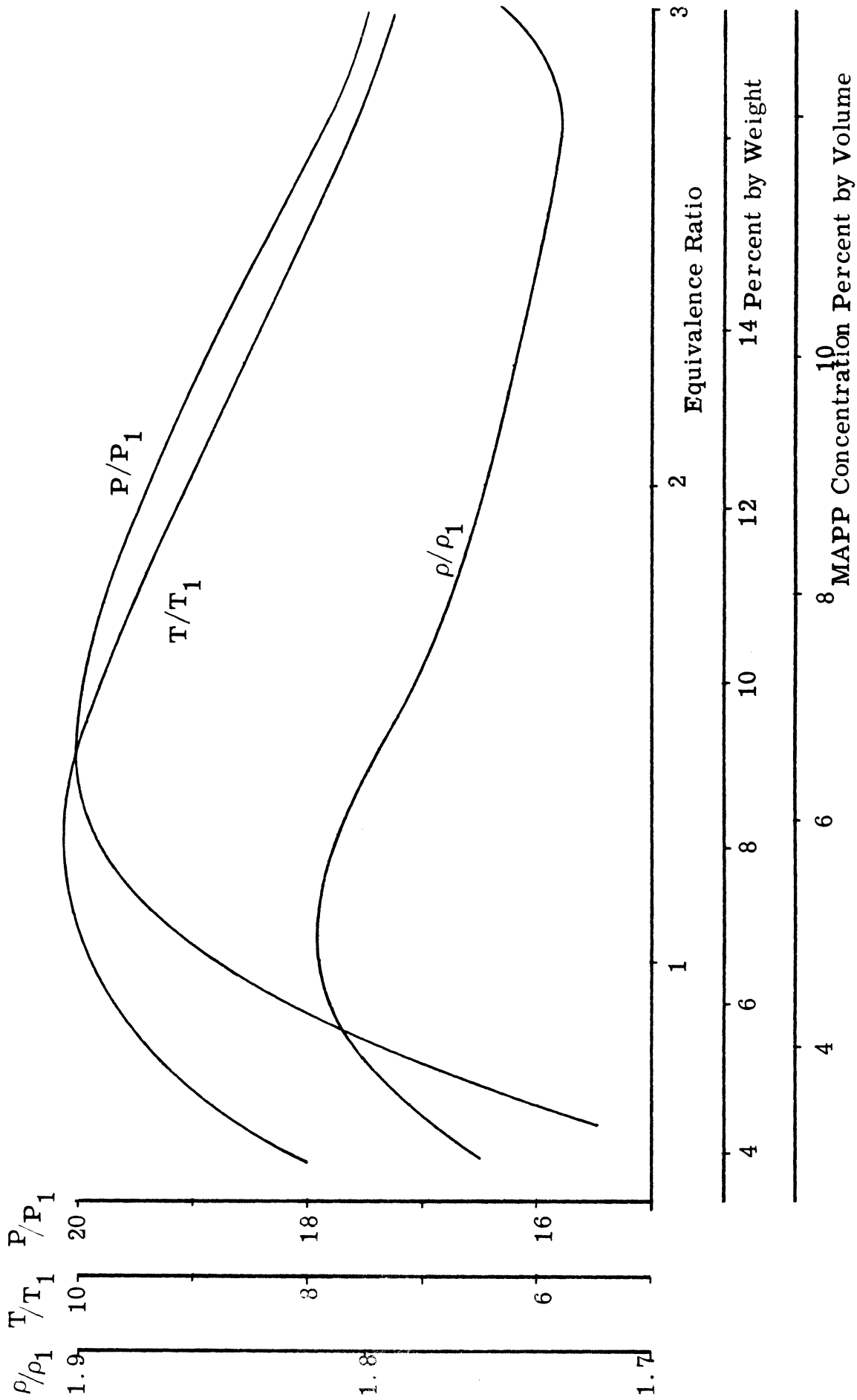
Figure 35(a). MAPP-Air Gas Detonation Properties.

100
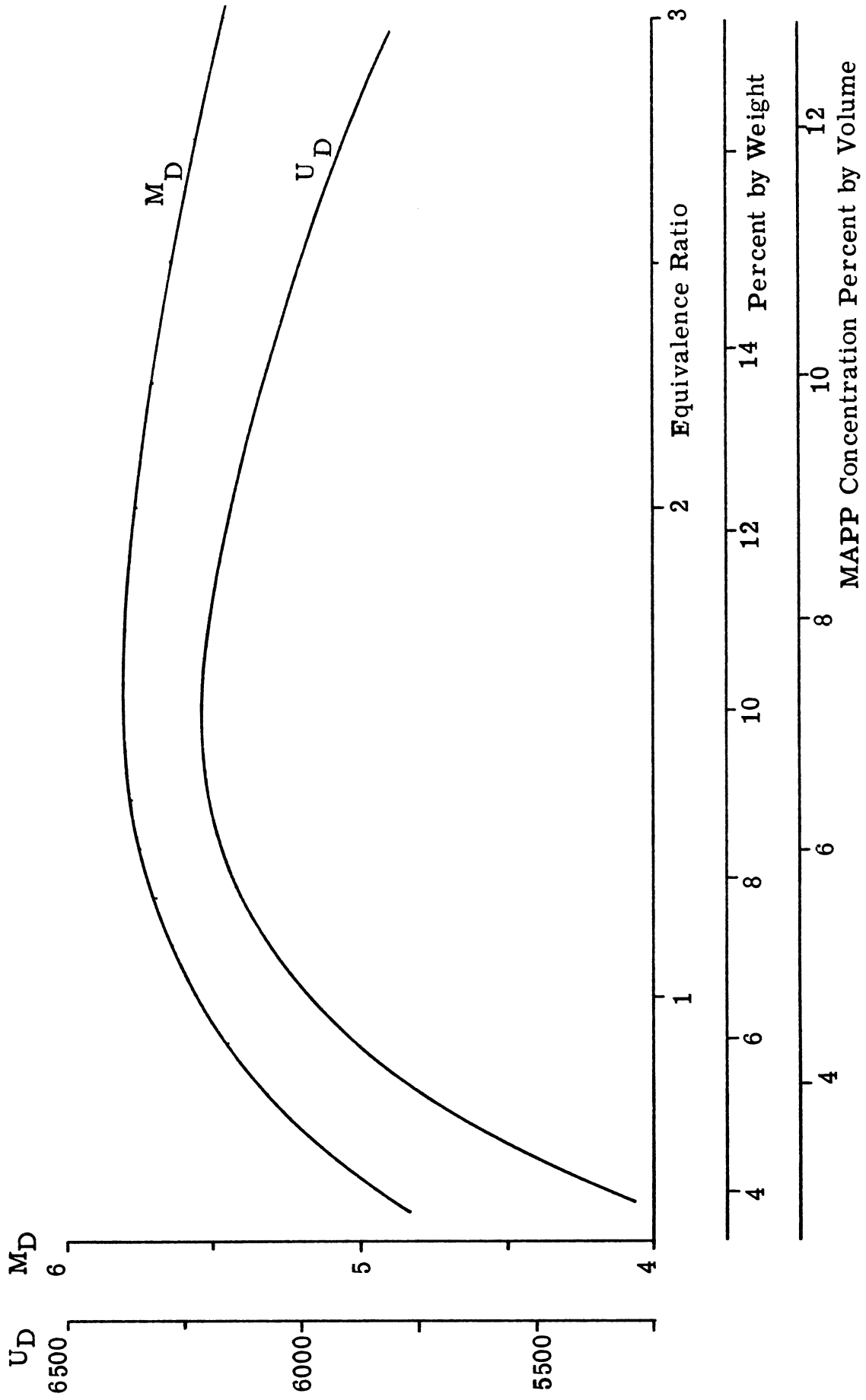
Figure 35(b). MAPP-Air Gas Detonation Properties.

101

TABLE XI. GAS CHROMATOGRAPH ANALYSIS CONDITIONS

Column:	
Length	10 ft
Inside diameter	1/4 in.
Composition	QF-1 30% on 60-80 chromosorb
Settings:	
Column temperature	$55^{O}F$
Detector temperature	$150^{O}F$
Injector temperature	$30^{O}F$
Helium flow	11 ml/min
Filament current	100 milliamperes

TABLE XII. MAPP GAS PROPERTIES

Molecular Weight	41.0
Density (slugs/ft^3)	0.1126
Stoichiometric equivalence ratio (O_2 basis)	0.302
Composition	
Methyl Actylene	51.0%
Propane	26.0%
Propadiene	23.0%

Appearing in Figure 36 is a sample series of radius-time plots of rough detonation data for concentration of 9.7 percent MAPP (by volume) in air. The threshold ignition energy for this concentration was selected to be 1.6 grams Detasheet. It is at this energy where the curve first begins to suggest a constant slope, implying constant propagation velocity beyond a given radii. A similar series of curves were generated for each of the other seven concentrations to establish the dependence of critical threshold energy upon MAPP concentration. This dependence is displayed in Table XIII, and it is plotted in Figure 37. The characteristically narrow U-shape of the MAPP-air detonation curve has been satisfactorily established. The limits of detonability found for the MAPP gas used were from 2.9 percent to 10.5 percent by volume. The rich limit is an extrapolation of data taken up to MAPP concentration of 9.7 percent by volume and represents a reasonable extension of the data.

It is of interest to examine these detonation limits in light of other recent experimental results. Table XIV represents a comparison of detonation limits on a percent volume basis between four separate experimental studies. By using the Crawshaw-Jones Apparatus, it was found that detonation limits of MAPP-air mixtures widened with increasing initiator energy. Yet the bag tests of Benedick et al.[10] and Collins[11] did not confirm this functional dependency. Similarly, the present study,
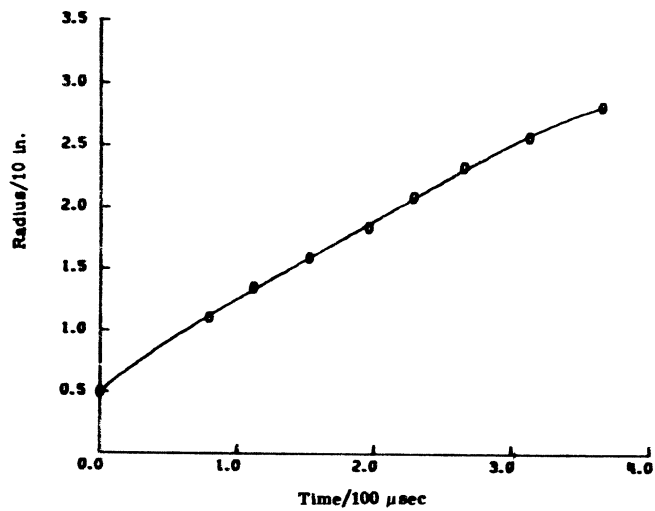
Figure 36(a). 9.7% MAPP-Air Detonation Data, 0.75 gram
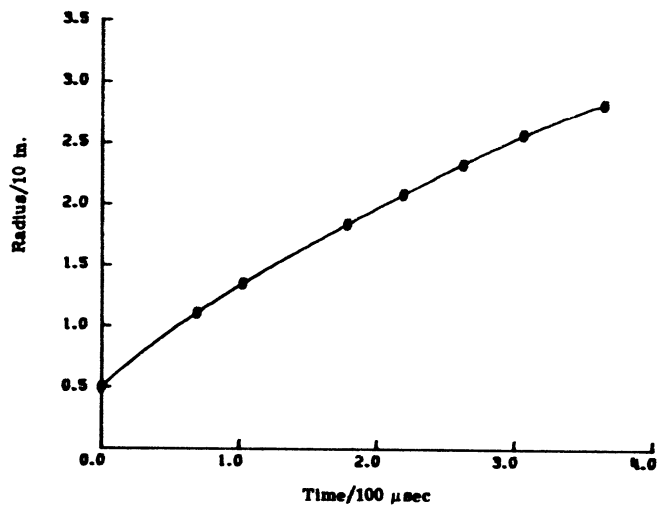
Figure 36(b). 9.7% MAPP-Air Detonation Data, 1.0 gram
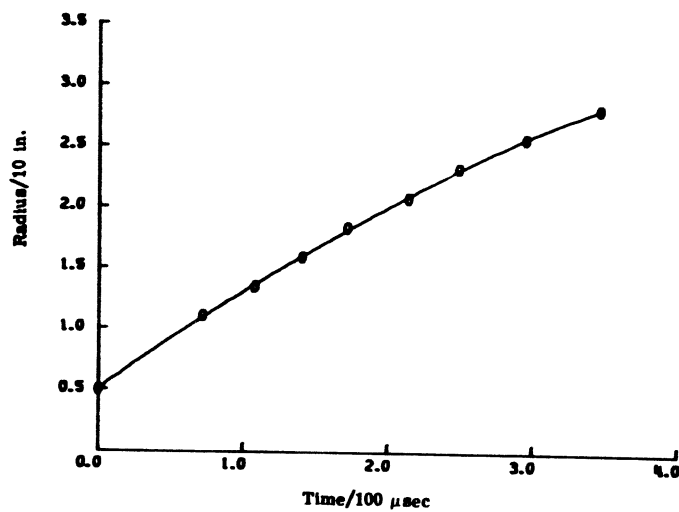
Figure 36(c). 9.7% MAPP-Air Detonation Data, 1.25 grams
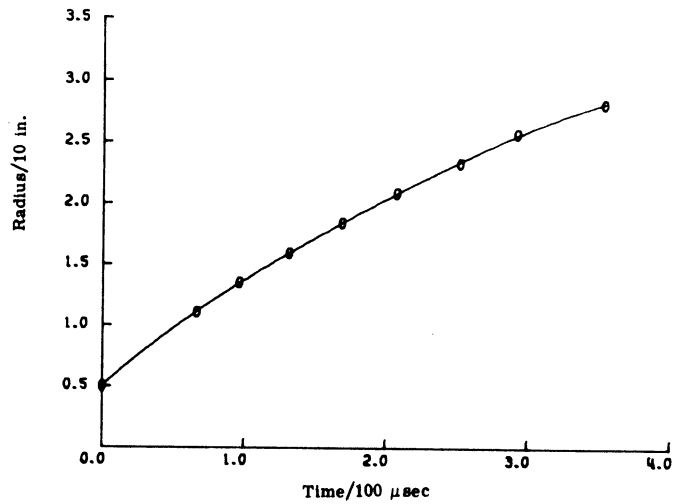
Figure 36(d).   9.7% MAPP-Air Detonation Data, 1.4 grams
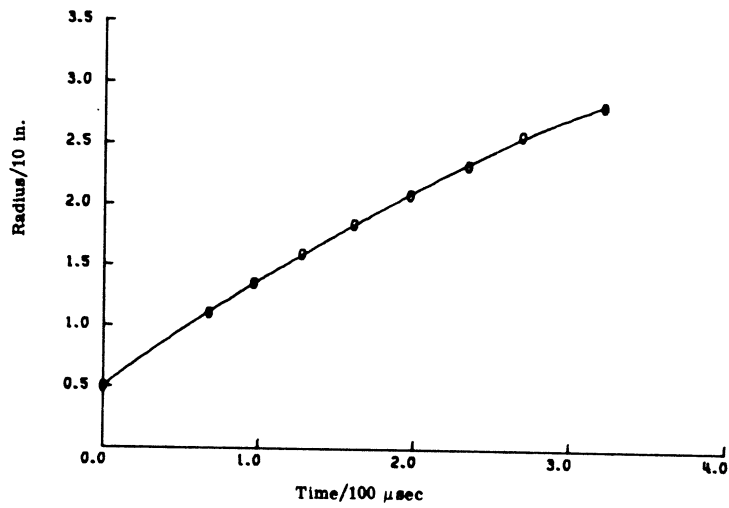
Figure 36(e).   9.7% MAPP-Air Detonation Data, 1.5 grams
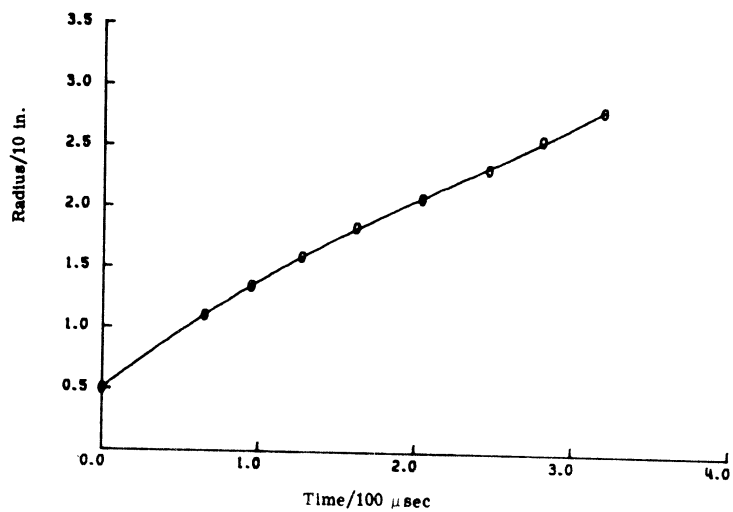
Figure 36(f).   9.7% MAPP-Air Detonation Data, 1.6 grams

106
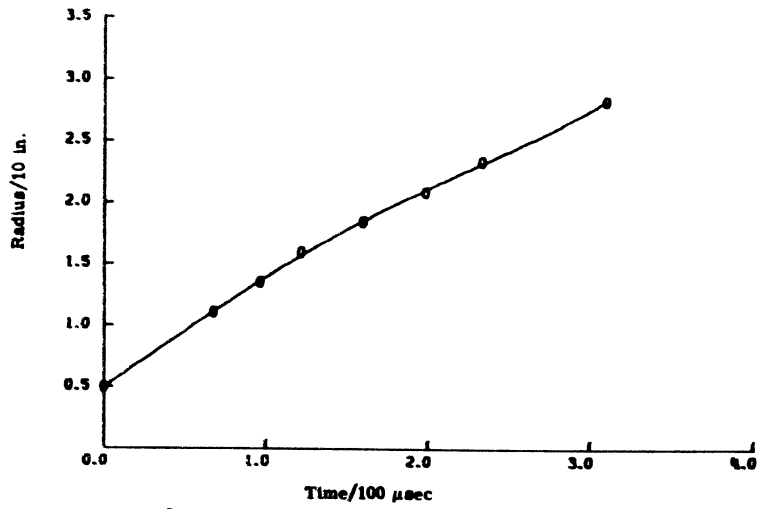
Figure 36(g). 9.7% MAPP-Air Detonation Data, 1.75 grams
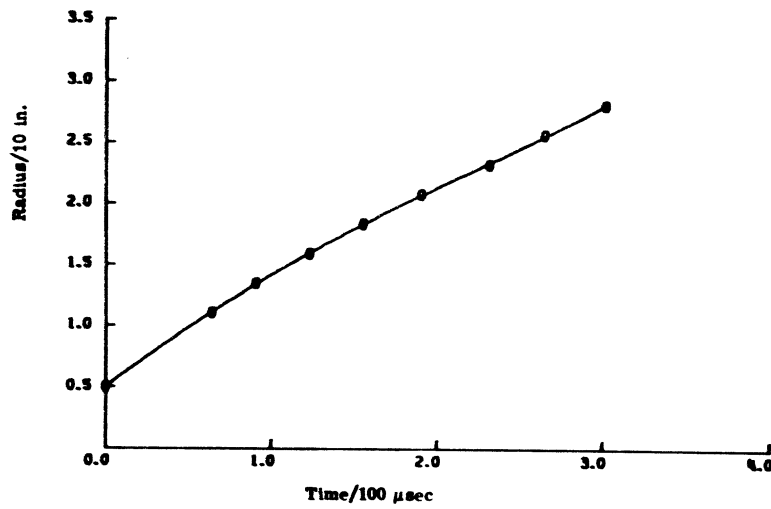
Figure 36(h). 9.7% MAPP-Air Detonation Data, 2.0 grams
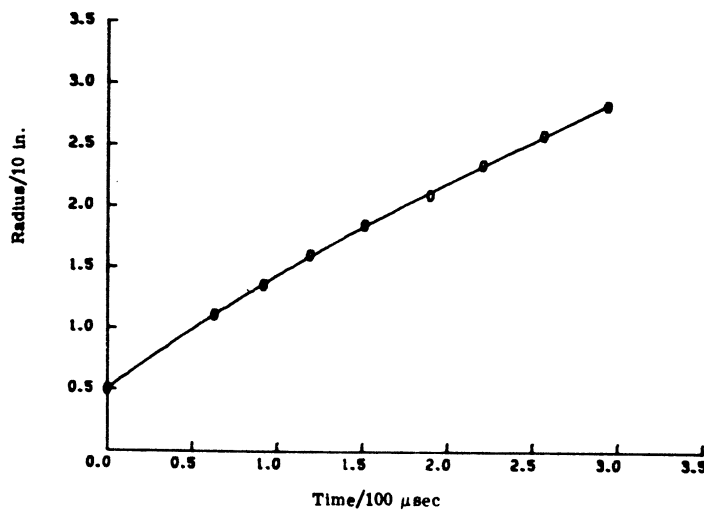
Figure 36(i). 9.7% MAPP-Air Detonation Data, 2.5 grams

107
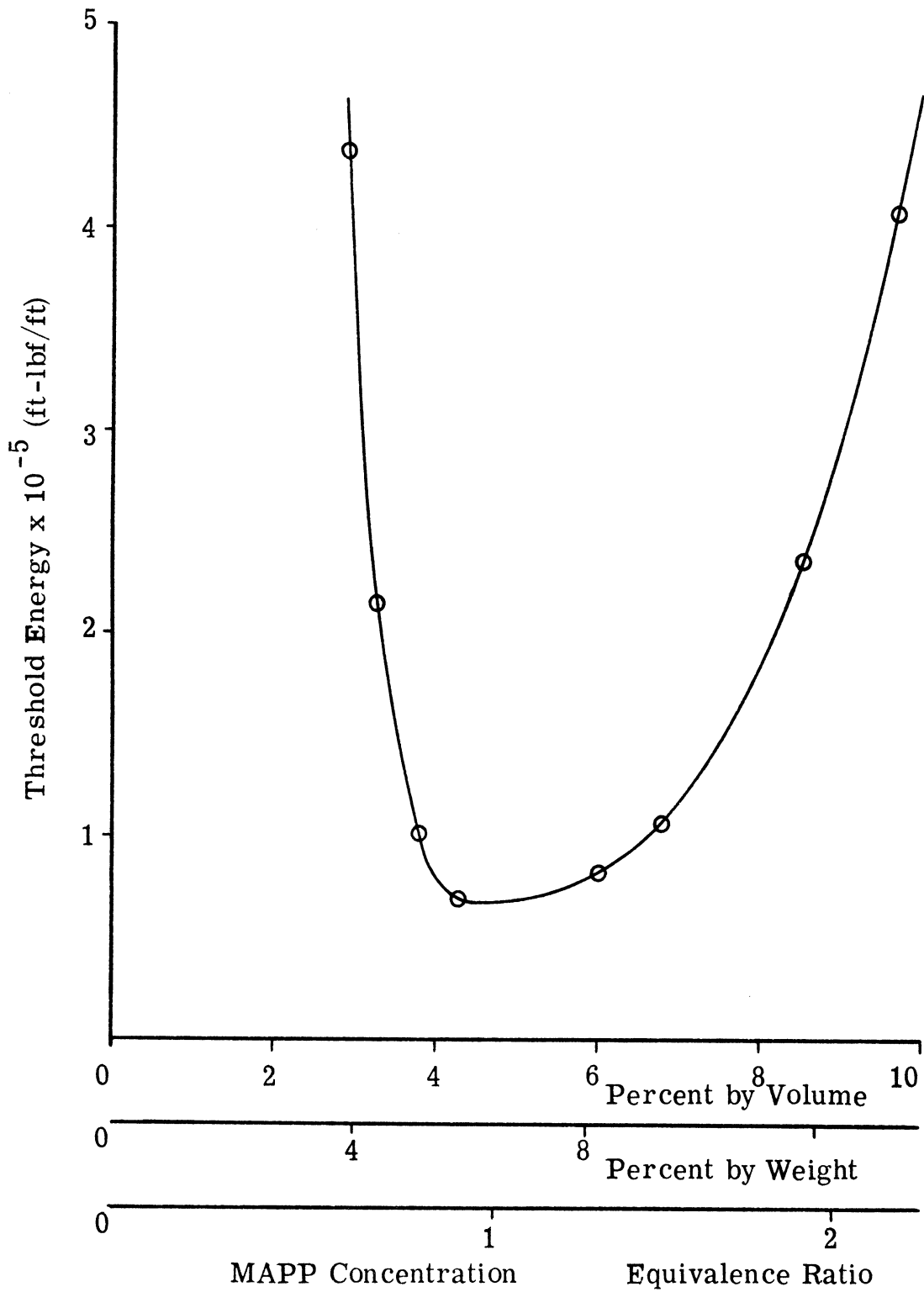
Figure 37. Critical Threshold Energy for Detonation Initiation as a Function of MAPP Concentration in Air.

TABLE XIII. CRITICAL ENERGY THRESHOLD FOR MAPP-AIR MIXTURES IN THE SECTORED CHAMBER

Φ	Percent MAPP in Air by Weight	Percent MAPP in Air by Volume	Effective Initiator Energy	
			ft-lbf	ft-lbf/ft
2.20	13.33	9.7	3875.3	408,664
1.90	11.69	8.5	2243.0	236,190
1.49	9.43	6.8	1011.9	106,553
1.30	8.36	6.0	793.4	83,545
0.90	5.92	4.3	647.9	68,234
0.78	5.12	3.8	1144.1	120,471
0.59	4.40	3.3	2039.2	214,731
0.56	4.00	2.9	4160.7	438,118

TABLE XIV. DETONATION LIMITS OF MAPP-AIR MIXTURES BY VOLUME

Method	Initiator	Lower Limit	Upper Limit
Crawshaw-Jones Apparatus	1 gram, PETN	4.1	7.8
Crawshaw-Jones Apparatus	10 grams, PETN	2.4	13.7
Crawshaw-Jones Apparatus	100 grams, PETN	-	≥ 30
Bag Test	800 grams, C-4 (672 grams, PETN equivalent)	2.9	10.2
Bag Test	386 grams, PETN	2.9	9.1
Sectored Chamber	2 grams, Detasheet 'C' (1.57 grams, PETN equivalent)	2.9	10.5[a]

[a] Extrapolated from test results taken up to 9.7 percent by volume.

using initiator energies two orders of magnitude smaller than the latter

two studies, tends to cast doubt upon such a dependency. There is ob-

viously a need for further work on this subject.

A further comparison was performed to examine the critical threshold

energy limits of the present study relative to those of recent AFATL bag

tests by P. Collins[11]. Figure 38 is a plot of nondimensional critical

threshold energy as a function of MAPP concentration by weight for the

two mentioned studies. The nondimensional energy, $\overline{E}$, was arrived

at by dividing all energies for a given study by an energy selected from

this data as the standard. The standard for each study was the value

of critical energy corresponding to 11.7 percent MAPP by weight.

This standard is not absolute, but rather it was conveniently chosen to

demonstrate relative trends in critical energy since data was obtained

in both studies at this MAPP concentration. The comparison reveals the

present study produced data suggesting a slightly broader and slightly

shallower characteristic threshold curve. The broader detonability

limits in the present study are supported by the fact that the MAPP gas

used had a higher percent of methyl acetylene present as compared to

the MAPP used in the bag tests. The composition of the MAPP used in

the bag tests is reported to have approximately the composition 37 percent

methyl acetylene, 25 percent prodadiene, 20 percent propane, 9 percent

C_4-carbon compounds (mostly n-butane) by volume.
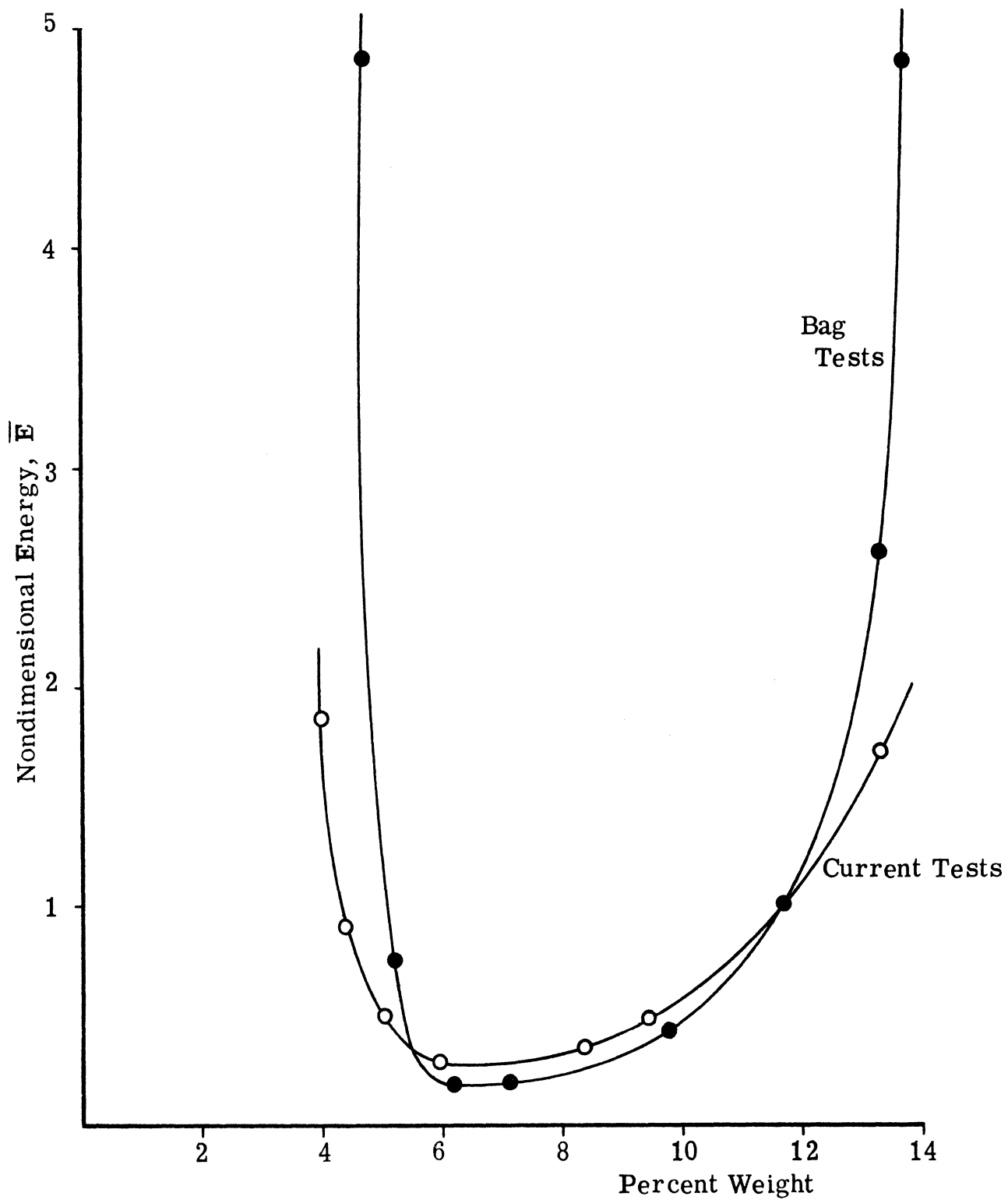
Figure 38. Comparison of Current MAPP-Air Detonation
Initiation Limits with AFATL "Bag" Test Results.

It is apparent from the foregoing discussions that the experimental

phase of this research continues to lend encouragement to the prediction

of gas-phase and two-phase detonation wave properties and threshold

energy levels required for detonation initiation.

APPENDIX I

CALCULATION OF BLAST WAVE IMPULSE

As indicated in Reference 1 the self-similar blast wave solution can be found in analytical form. The analytical solution, which is given by Sedov[4] and repeated here, is expressed with the dimensionless velocity V as a parameter. $V(\lambda)$ is related to the dimensional velocity v by

$$v = (r/t)\ V(\lambda) \tag{I-1}$$

With v_2, ρ_2, p_2, and T_2, the velocity, density, pressure, and temperature immediately behind the leading shock the analytical solution is as follows:

$$\frac{r}{r_s} = \left[\frac{(\nu + 2)(\gamma + 1)}{4}\ V\right]^{-2/(2+\nu)} \left\{\frac{\gamma + 1}{\gamma - 1}\left[\frac{(\nu + 2)\gamma}{2}\ V - 1\right]\right\}^{-\alpha_2}$$

$$\times \left\{\frac{(\nu + 2)(\gamma + 1)}{(\nu + 2)(\gamma + 1) - 2\left[2 + \nu(\gamma - 1)\right]}\left[1 - \frac{2 + \nu(\gamma - 1)}{2}\ V\right]\right\}^{-\alpha_1} \tag{I-2}$$

$$\frac{v}{v_2} = \frac{(\nu + 2)(\gamma + 1)}{4}\ V\ \frac{r}{r_s} \tag{I-3}$$

$$\frac{\rho}{\rho_2} = \left\{\frac{\gamma + 1}{\gamma - 1}\left[\frac{(\nu + 2)\gamma}{2}\ V - 1\right]\right\}^{\alpha_3}\left[\frac{\gamma + 1}{\gamma - 1}\left(1 - \frac{\nu + 2}{2}\ V\right)\right]^{\alpha_5}$$

$$\times \left\{\frac{(\nu + 2)(\gamma + 1)}{(\nu + 2)(\gamma + 1) - 2\left[2 + \nu(\gamma - 1)\right]}\left[1 - \frac{2 + \nu(\gamma - 1)}{2}\ V\right]\right\}^{\alpha_4} \tag{I-4}$$

115

$$\frac{p}{p_2} = \left[\frac{(\nu + 2)(\gamma + 1)}{4}\right]^{2\nu/(2+\nu)} \left[\frac{\gamma + 1}{\gamma - 1}\left(1 - \frac{\nu + 2}{2}V\right)\right]^{\alpha_5 + 1}$$

$$\times \left\{\frac{(\nu + 2)(\gamma + 1)}{(\nu + 2)(\gamma + 1) - 2\left[2 + \nu(\gamma - 1)\right]}\left[1 - \frac{2 + \nu(\gamma - 1)}{2}V\right]\right\}^{\alpha_4 - 2\alpha_1} \qquad (I-5)$$

$$\frac{T}{T_2} = \frac{p}{p_2}\left(\frac{\rho_2}{\rho}\right) \qquad (I-6)$$

where

$$\alpha_1 = \frac{(\nu + 2)\gamma}{2 + \nu(\gamma - 1)}\left[\frac{2\nu(2 - \gamma)}{\gamma(\nu + 2)^2} - \alpha_2\right]$$

$$\alpha_2 = \frac{1 - \gamma}{2(\gamma - 1) + \nu} \qquad ; \qquad \alpha_3 = \frac{\nu}{2(\gamma - 1) + \nu}$$

$$\alpha_4 = \frac{\alpha_1(\nu + 2)}{2 - \gamma} \qquad ; \qquad \alpha_5 = \frac{2}{\gamma - 2}$$

For the blast wave solution V lies in the range

$$\frac{2}{(\nu + 2)\gamma} \leq V \leq \frac{4}{(\nu + 2)(\gamma + 1)} \qquad (I-7)$$

The value of $V = 4/(\nu + 2)(\gamma + 1)$ corresponds to a point immediately behind the shock wave and the point $V = 2/(\nu + 2)\gamma$ corresponds to the singular point at the center of the blast wave.

Equations (I-2) to (I-6) have been programmed for the computer to produce the variation of v/v_2, ρ/ρ_2, p/p_2, and T/T_2 as a function

of r/r_s. The calculation is started at $V = 4/(\nu + 2)(\gamma + 1)$ and V is

allowed to approach the blast center value of $2/(\nu + 2)\gamma$. As a check

several cases computed by Sedov[4] were also determined using the blast

computer program and exact agreement was found.

A separate computer program was developed to compute the param-

eters $\beta(\gamma, \nu)$ from Equation (15) and $\alpha(\gamma, \nu)$ defined by

$$\alpha(\gamma, \nu) = \sigma_\nu \left[\frac{1}{2} \int_0^1 R\, V^2 \lambda^{\nu+1}\, d\lambda + \frac{1}{\gamma - 1} \int_0^1 P \lambda^{\nu+1}\, d\lambda \right] \tag{I-8}$$

It is important to recognize that p/p_2 and the similarity variable $P(\lambda)$

are connected by the relation

$$P = \left(\frac{p}{p_2}\right) \frac{8}{(\nu + 2)^2 (\gamma + 1)} \frac{1}{\lambda^2}$$

The above computer programs and sample outputs are available on

request. Typical variations of p/p_2, v/v_2, and T/T_2 with the ratio of

specific heats γ and with the geometry parameter ν are shown in Figures

I-1 to I-6.
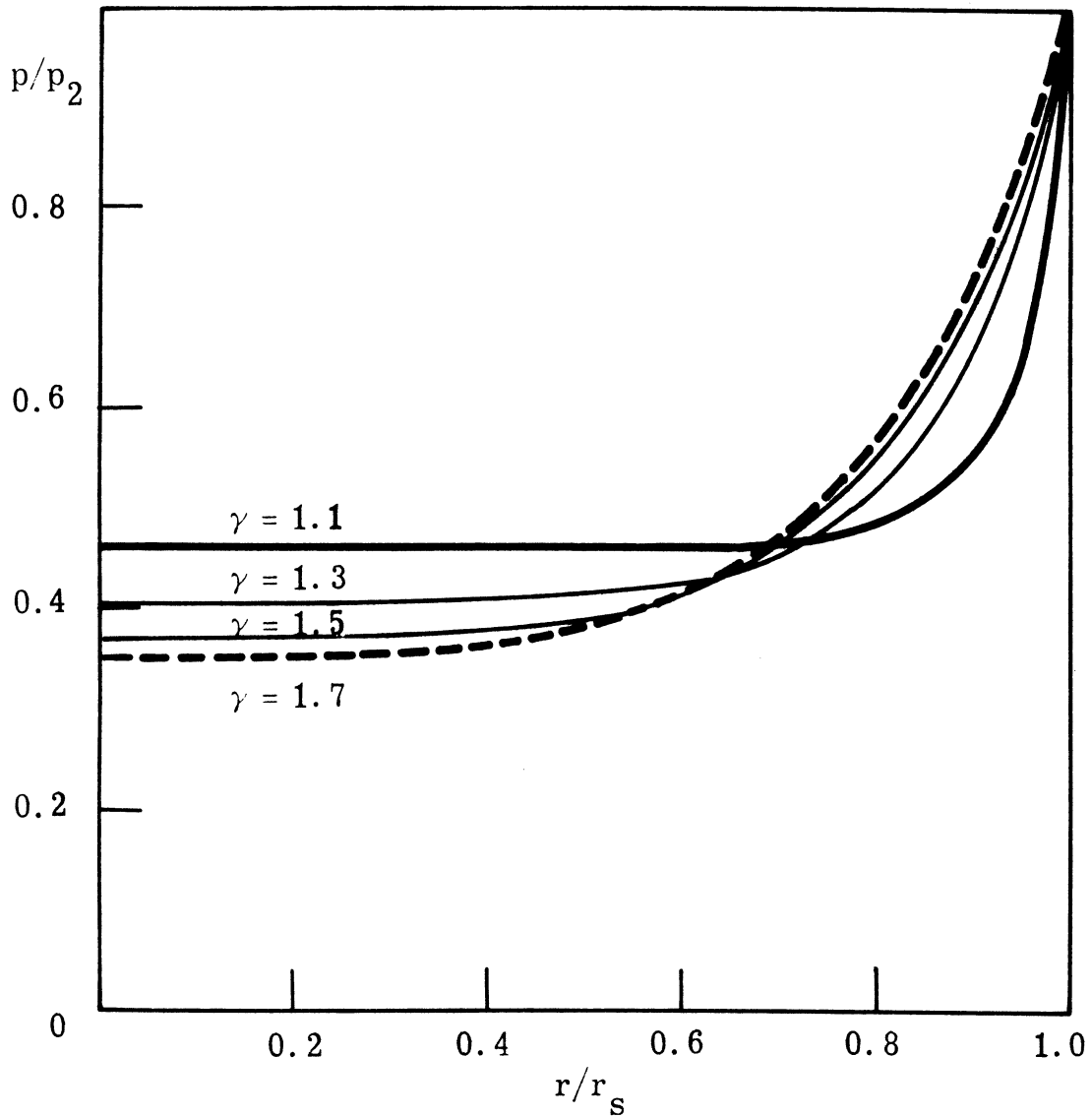
$$p_2 = \frac{8\rho_1}{(\nu + 2)^2 (\gamma + 1)} \left(\frac{E_o}{\alpha p_1}\right)^{2/\nu+1} t^{-2\nu/\nu+2}$$

$$r_s = \left(\frac{E_o}{\alpha \rho_1}\right)^{1/\nu+2} t^{2/\nu+2}$$

Figure I -1. Variation of Blast Wave Pressure with γ:
Planar Wave; ν = 1.0.

$$r/r_s = \lambda$$

$$v_2 = \frac{4}{(\nu + 2)(\gamma + 1)} \left(\frac{E_o}{\alpha \rho_1}\right)^{1/\nu+2} t^{-\nu/\nu+2}$$
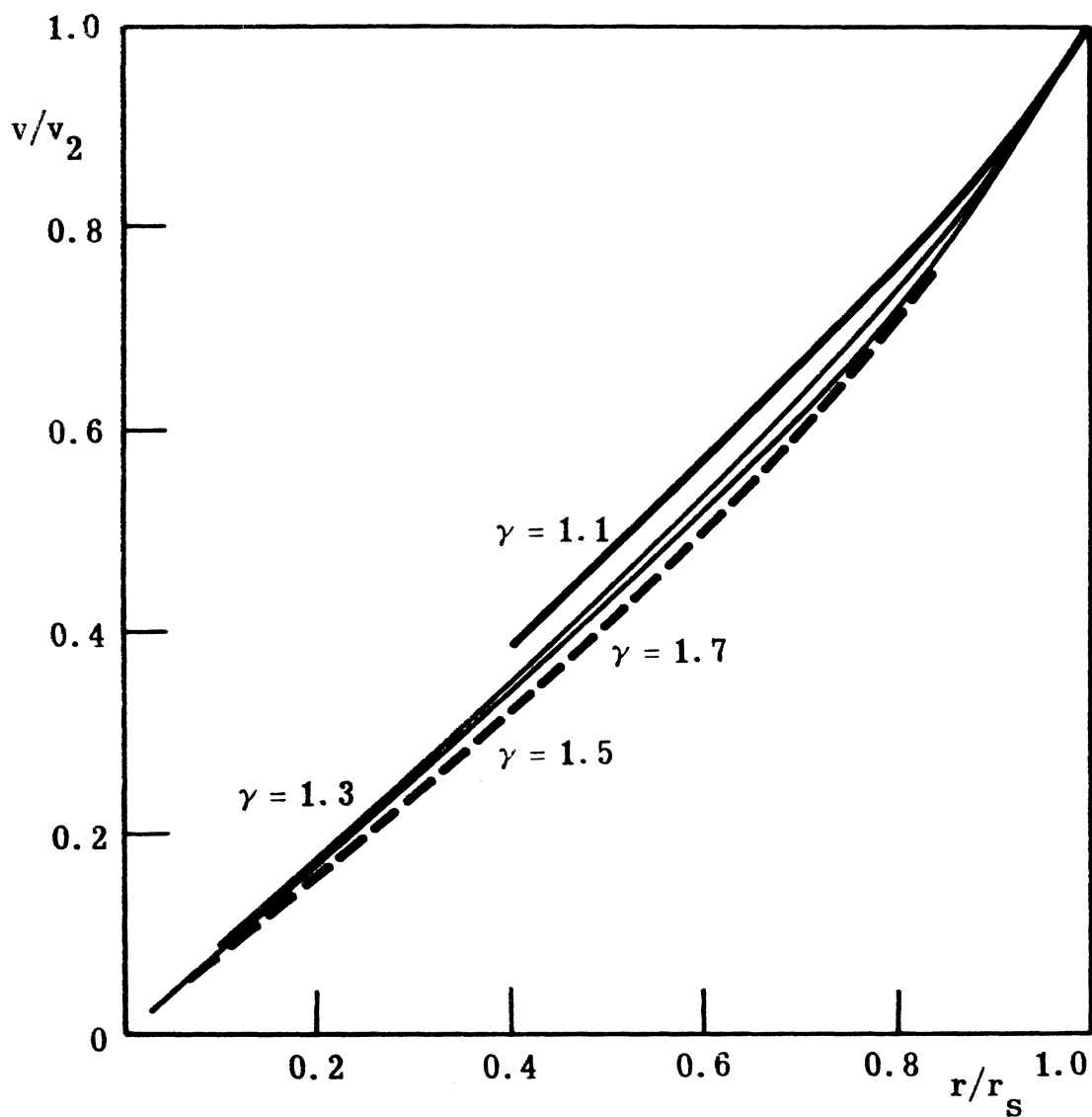
$$r_s = \left(\frac{E_o}{\alpha \rho_1}\right)^{1/\nu+2} t^{2/\nu+2}$$

Figure I-2. Variation of Blast Wave Velocity with γ:
Planar Wave; $\nu = 1.0$.

119
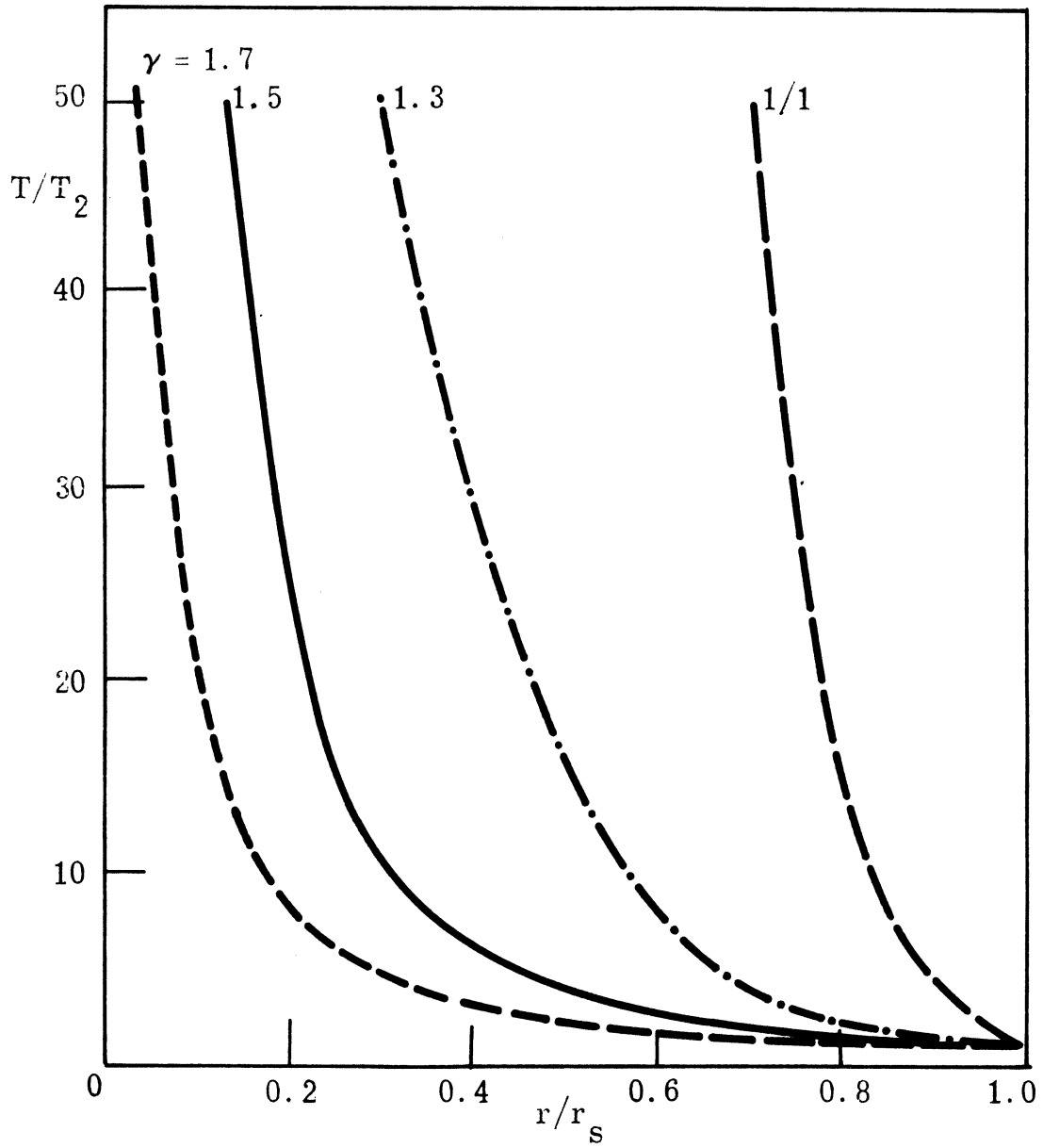
$$T_2 = \frac{8(\gamma - 1)}{(\nu + 2)^2 \, (\gamma + 1)^2} \left(\frac{E_o}{\alpha \rho_1}\right)^{2/\nu+2} t^{-2\nu/\nu+2}$$

$$r_s = \left(\frac{E_o}{\alpha \rho_1}\right)^{1/\nu+2} t^{2/\nu+2}$$

Figure I -3. Variation of Blast Wave Temperature with γ;
Planar Wave: $\nu = 1.0$

120

Dimensionless Pressure vs Distance

$$\text{———} \quad \nu = 1.0$$
$$\text{—···—} \quad \nu = 2.0$$
$$\text{— — —} \quad \nu = 3.0$$

$$\gamma = 1.3$$
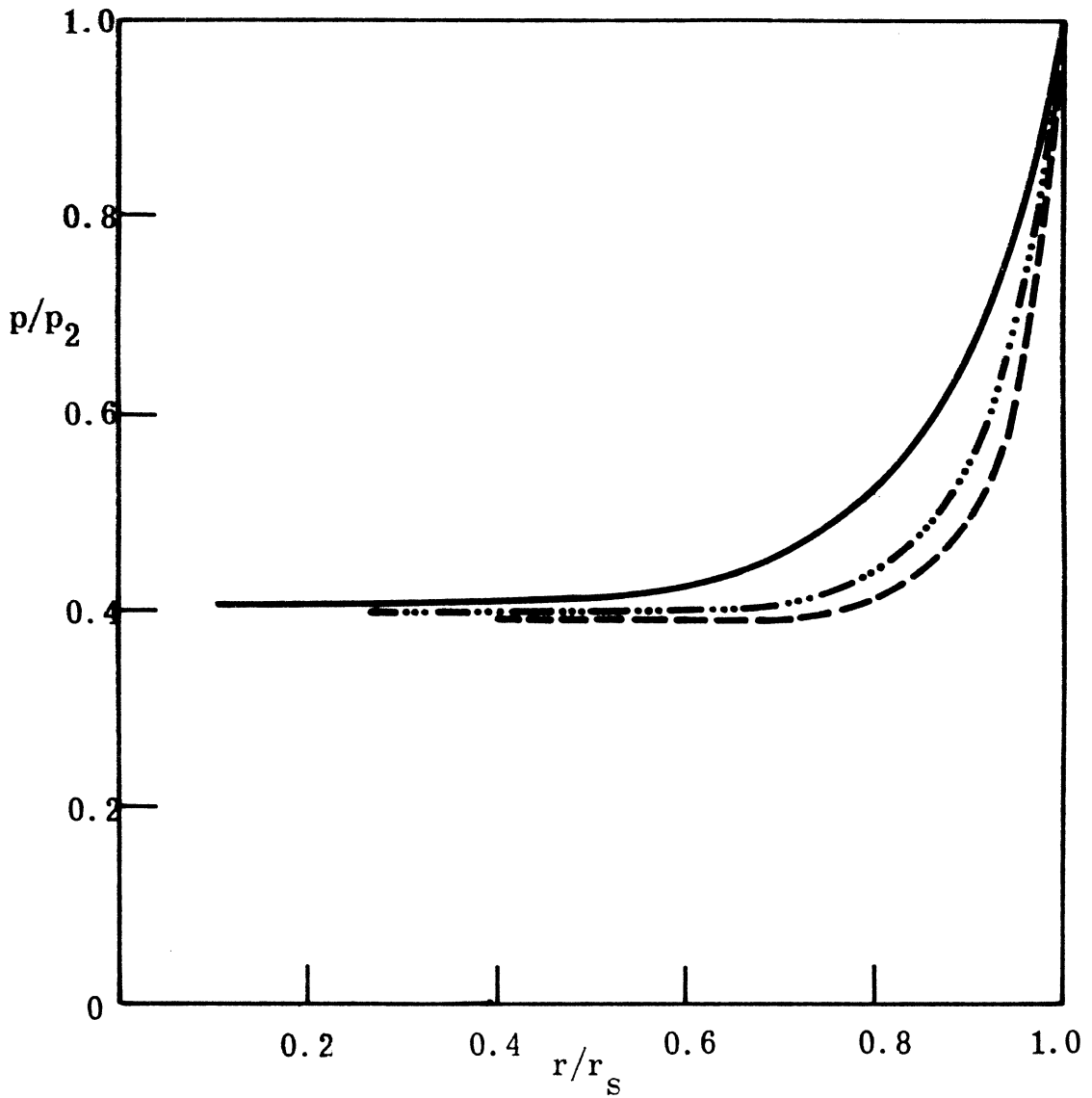
$$p_2 = \frac{8\rho_1}{(\nu + 2)^2 (\gamma + 1)}\left(\frac{E_o}{\alpha\rho_1}\right)^{2/\nu+2} t^{-2\nu/\nu+2}$$

$$r_s = \left(\frac{E_o}{\alpha\rho_1}\right)^{1/\nu+2} t^{2/\nu+2}$$

Figure I -4. Variation of Blast Wave Pressure with Geometry; $\gamma = 1.3$

121
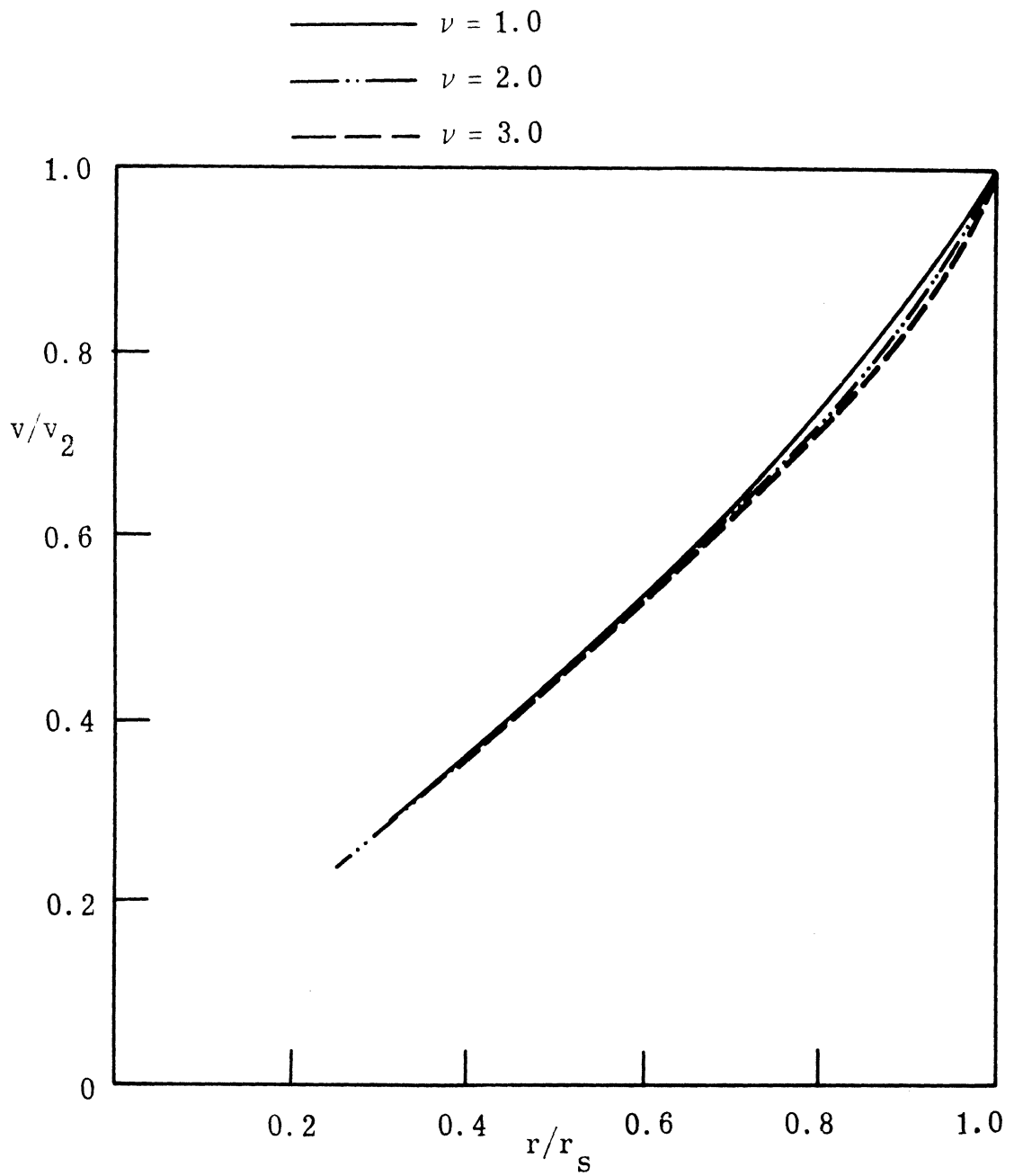
Figure I -5. Variation of Blast Wave Velocity with Geometry; $\gamma = 1.3$

122
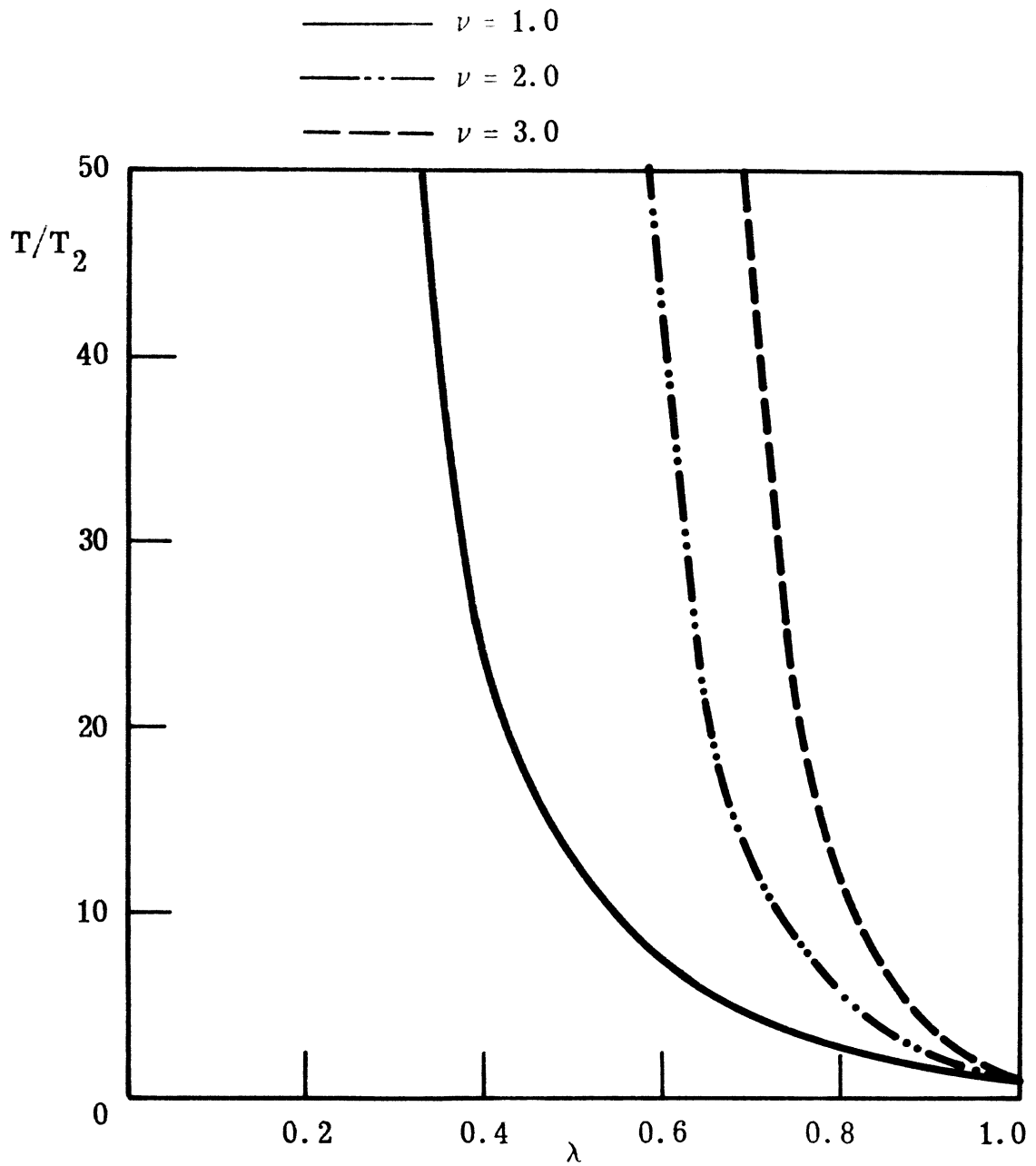
$$T_2 = \frac{8(\gamma - 1)}{(\nu + 2)^2 (\gamma + 1)^2} \left(\frac{E_o}{\alpha \rho_1}\right)^{2/\nu+2} t^{-2\nu/\nu+2}$$

$$r_s = \left(\frac{E_o}{\alpha \rho_1}\right)^{1/\nu+2} t^{2/\nu+2}$$

Figure I-6. Variation of Blast Wave Temperature
with Geometry, $\gamma = 1.3$

123

APPENDIX II

CALCULATION OF THE GROUND IMPULSE
FROM A CHAPMAN-JOUGUET DETONATION

As indicated in Reference 1 the conservation equations describing the self-similar flow behind a Chapman-Jouguet Detonation can be reduced to the single ordinary differential equation

$$\frac{dz}{dV} = \frac{z[2(V-1)^2 + (\nu - 1)(\gamma_2 - 1)V(V-1) - 2z]}{V[(V-1)^2 - \nu z]} \qquad \text{(II-1)}$$

where V is a dimensionless velocity defined by

$$\nu = \frac{r}{t}V \qquad \text{(II-2)}$$

and

$$z = \gamma \frac{P}{R} ; \qquad p = \rho_1(r^2/t^2)P$$

$$\rho = \rho_1 R \qquad \text{(II-3)}$$

γ_2 is the ratio of specific heats of the combustion products. Integration of Equation (II-1), which must be carried out numerically, is the key problem in determining the self-similar flow behind a C-J detonation. Once the relation between z and V is determined, the variation of V and z with the dimensionless radius $\lambda = (r/r_s)$ can be found by integrating the equation

$$\frac{d(\ln \lambda)}{dV} = \frac{z - (V-1)^2}{V[(V-1)^2 - \nu z]} \qquad \text{(II-4)}$$

124

The flow behind the detonation is assumed to be isentropic so that z and R are related by

$$\lambda^2 \frac{z}{\frac{(\gamma_2 - 1)}{R_2^2}} = \frac{z_2}{\frac{(\gamma_2 - 1)}{R_2^2}} \tag{II-5}$$

z_2 and R_2 are the values of z and R immediately behind the detonation front and for a C-J detonation are given by

$$R_2 = [\ \frac{\gamma_2}{\gamma_2 + 1}(1 + \frac{z_1}{\gamma_1})\ ]^{-1} \tag{II-6}$$

$$z_2 = \frac{\gamma_2^2}{(\gamma_2 + 1)^2}(1 + \frac{z_1}{\gamma_1})^2$$

z_1, the value of z immediately ahead of the detonation is given by

$$z_1 = \gamma_1 \frac{P_1}{R_1} = \frac{\gamma_1 [\ \frac{P_1}{\rho_1(r_s^2/t^2)}\ ]}{(1.0)} \tag{II-7}$$

since $R_1 = 1.0$. Since $r_s = Ct$ for a C-J detonation

$$z_1 = \frac{\gamma_1 \frac{P_1}{\rho_1}}{C^2} = \frac{1}{M_D^2} \tag{II-8}$$

The behavior of the C-J solution in the z-V plane as determined by Equation (II-1) has been discussed in Reference 1, and is also indicated in Figure (II-1) below. Ahead of the detonation front v and hence V = 0 while $p = p_1$ and $\rho = \rho_1$. Thus, the variable z becomes

125
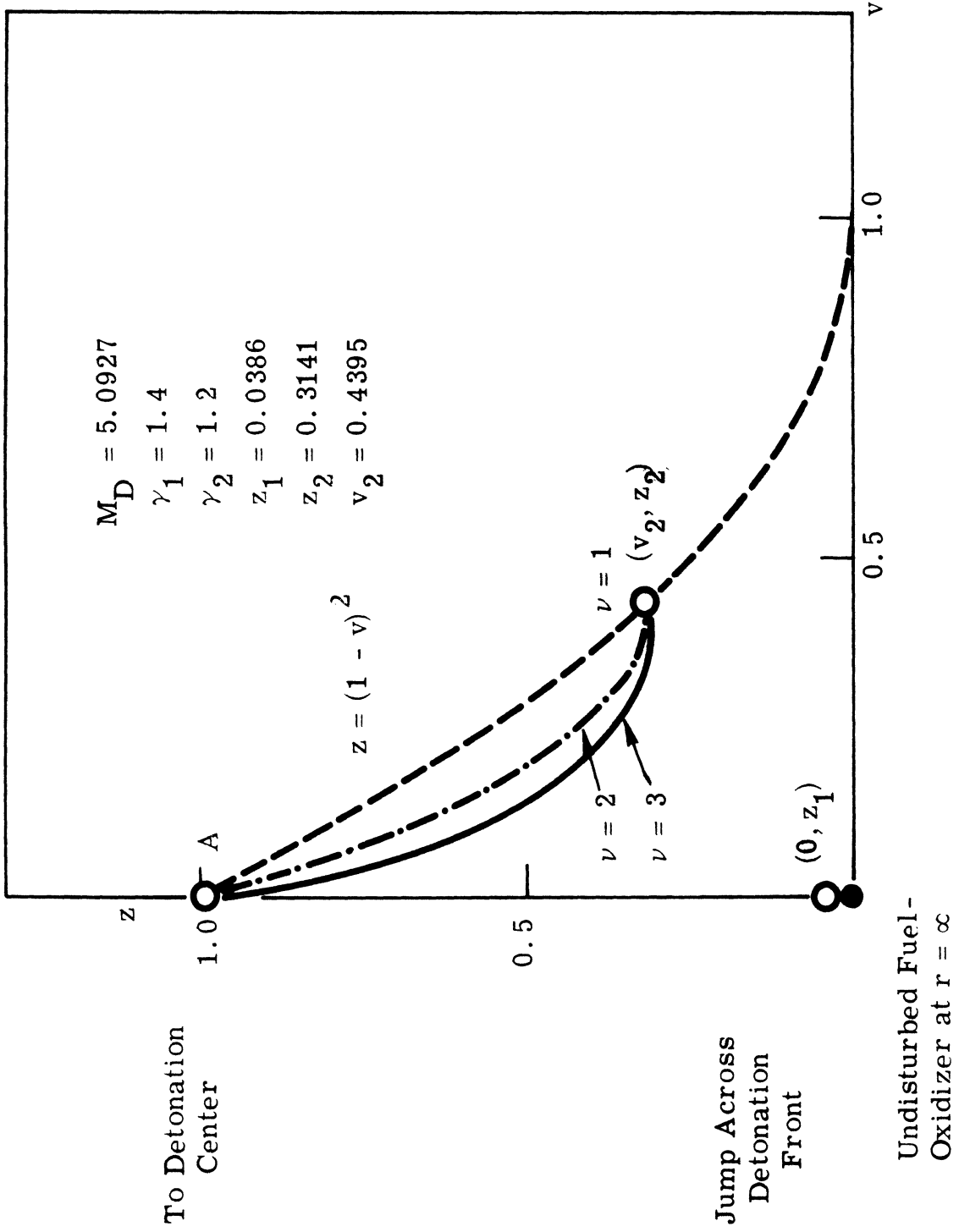
Figure II-1. The v-z Plane for a C-J Detonation.

$M_D = 5.0927$
$\gamma_1 = 1.4$
$\gamma_2 = 1.2$
$z_1 = 0.0386$
$z_2 = 0.3141$
$v_2 = 0.4395$

$z = (1-v)^2$

$\nu = 1$

(v_2, z_2)

$\nu = 2$

$\nu = 3$

$(0, z_1)$

To Detonation
Center

A

z

1.0

0.5

0.5

1.0

v

Jump Across
Detonation
Front

Undisturbed Fuel -
Oxidizer at $r = \infty$

126

$$z = \rho_1 \frac{P_1}{\rho_1 (r^2/t^2)} \tag{II-9}$$

The undisturbed fuel-oxidizer mixture at $r \rightarrow \infty$ thus corresponds to the point $z = 0$, $V = 0$, while the point immediately ahead of the detonation front corresponds to $z = z_1 = M_D^{-2}$; $V = 0$. There is then a discontinuous jump across the detonation front to the point (z_2, V_2) immediately downstream of the detonation. For a C-J detonation (z_2, V_2) lies on the parabola $z = (1-V)^2$ the locus of points where the velocity is sonic with respect to the detonative discontinuity.

The detonation front is followed by an isentropic expansion through which the velocity of the combustion products drops to zero at the boundary of a stationary core region, which corresponds to the point A: $z = 1$, $V = 0$. The point A is a singular point which can be shown to be a node, and it is the transition from (z_2, V_2) to A which must be determined by numerical integration of Equation (II-1). In the physical plane the point A moves radially outward with the speed of sound and corresponds to the characteristic separating the stationary core from the expansion behind the detonation. The stationary core is represented by the line $V = 0$ extending from $z = 1$ to $z = \infty$ which corresponds to the detonation center $r = 0$.

At the singularity A, Equation (II-1) becomes indeterminate since both the numerator and the denominator vanish. The behavior of the solution curve near A can, nevertheless, be established as indicated below. Letting $z = 1 + \zeta$ and keeping only the largest terms with ζ, $V \ll 1$, Equation (II-1) becomes

127

$$\frac{d\mathcal{L}}{dV} = \frac{[\,4 + (\nu-1)(\gamma-1)\,]\,V + 2}{(\nu-1)\,V} \tag{II-10}$$

with the singularity now at $\mathcal{L} = 0$, $V = 0$. Equation (II-10) is linear and

can be solved to determine the behavior of the solution near the nodal point A.

If $\mathcal{L} = -$ a when $V = V_r$, then in the cylindrical case with $\nu = 2$

$$\mathcal{L} = - a \, \frac{V^2}{V_r^2} + (\gamma + 3) V (\frac{V}{V_r} - 1) \tag{II-11}$$

and

$$\lim_{V \to 0} \frac{d\mathcal{L}}{dV} = - (\gamma + 3)$$

i.e., the solution approaches A with a finite slope. In the spherical case

with $\nu = 3$

$$\mathcal{L} = (\gamma+1) V \ln \frac{V}{V_r} - a \, \frac{V}{V_r} \tag{II-12}$$

and

$$\lim_{V \to 0} \frac{d\mathcal{L}}{dV} = - \infty$$

i.e., the solution approaches A with infinite slope.

Numerically, Equation (II-1) was integrated using a fourth order

Runge-Kutta Method. The integration was initiated at the point (z_2, V_2),

which is known once the C-J conditions have been determined. Because

of the singularity at A, the integration was only extended from V_2 to a

minimum value of 0.005 for V. This procedure provided an adequate repre-

sentation of z(V) even near the singular point A. Some typical solution

128

curves for $\nu = 2, 3$ are shown in Figure (II -1). The planar case $\nu=1$ is special since then the appropriate solution of Equation (II-1) is the singular solution

$$z = (1-V)^2 \tag{II-13}$$

representing a plane expansion behind the detonation front.

As indicated above, once the variations of z with V is determined, z and V can be related to $\lambda = r/r_s$ by integration of Equation (II-4). Then the density variation can be found from Equation (II-5). Since the flow behind the detonation front is isentropic the pressure ratio (p/p_2) is related to the density ratio (ρ/ρ_2) by

$$\frac{p}{p_2} = (\frac{\rho}{\rho_2})^{\gamma_2} \tag{II-14}$$

while the temperature ratio (T/T_2) is given by

$$\frac{T}{T_2} = (\frac{p}{p_2})(\frac{\rho_2}{\rho}) \tag{II-15}$$

Equations (II-14) and (II-15) are, of course, based on the assumption that the combustion products can be treated as a perfect gas with constant specific heats.

As a check on the computational technique described above, results for $\nu = 3$, $p_1 = 0$, $\gamma_1 = \gamma_2 = 5/3$, were compared with the results of Sedov[4] who also considered this case, and exact agreement was found. As a typical example pressure, velocity and temperature profiles for a methane air

detonation are shown in Figures (II-2), (II-3), and (II-4).

The impulse functions $\delta(\gamma_2, \nu)$ can be computed once the variation of p/p_2 with λ is known. From the definition of P in Equation (II-3), it follows that

$$P = \frac{p}{\rho_1 \left(\frac{r^2}{t^2}\right)} = \frac{p_2}{\rho_1 \frac{r^2}{t^2}} \frac{p}{p_2} = \frac{p_2}{\rho_1 C^2 \lambda^2} \left(\frac{p}{p_2}\right) \tag{II-16}$$

From the C-J conditions (Equation (II-6)), it can then be shown that

$$\frac{p_2}{\rho_1 C^2} = \frac{1}{\gamma_2 + 1}\left(1 + \frac{z_1}{\gamma_1}\right) \tag{II-17}$$

so that

$$P = \frac{1}{(\gamma_2+1)} \frac{1}{\lambda^2} \frac{p}{p_2}\left(1 + \frac{z_1}{\gamma_1}\right)$$

and from Equation (25)

$$\delta(\gamma_2, \nu) = \frac{\left(1 + \frac{z_1}{\gamma_1}\right)}{(\gamma_2 - 1)} \int_0^1 \frac{p}{p_2} \lambda^{\nu-1} d\lambda \; ; \qquad \nu = 1, 2$$

$$\tag{II-18}$$

$$\delta(\gamma_2, 3) = \frac{\left(1 + \frac{z_1}{\gamma_1}\right)}{(\gamma_2+1)} \int_0^1 \frac{p}{p_2} \lambda \; d\lambda; \quad \nu = 3$$
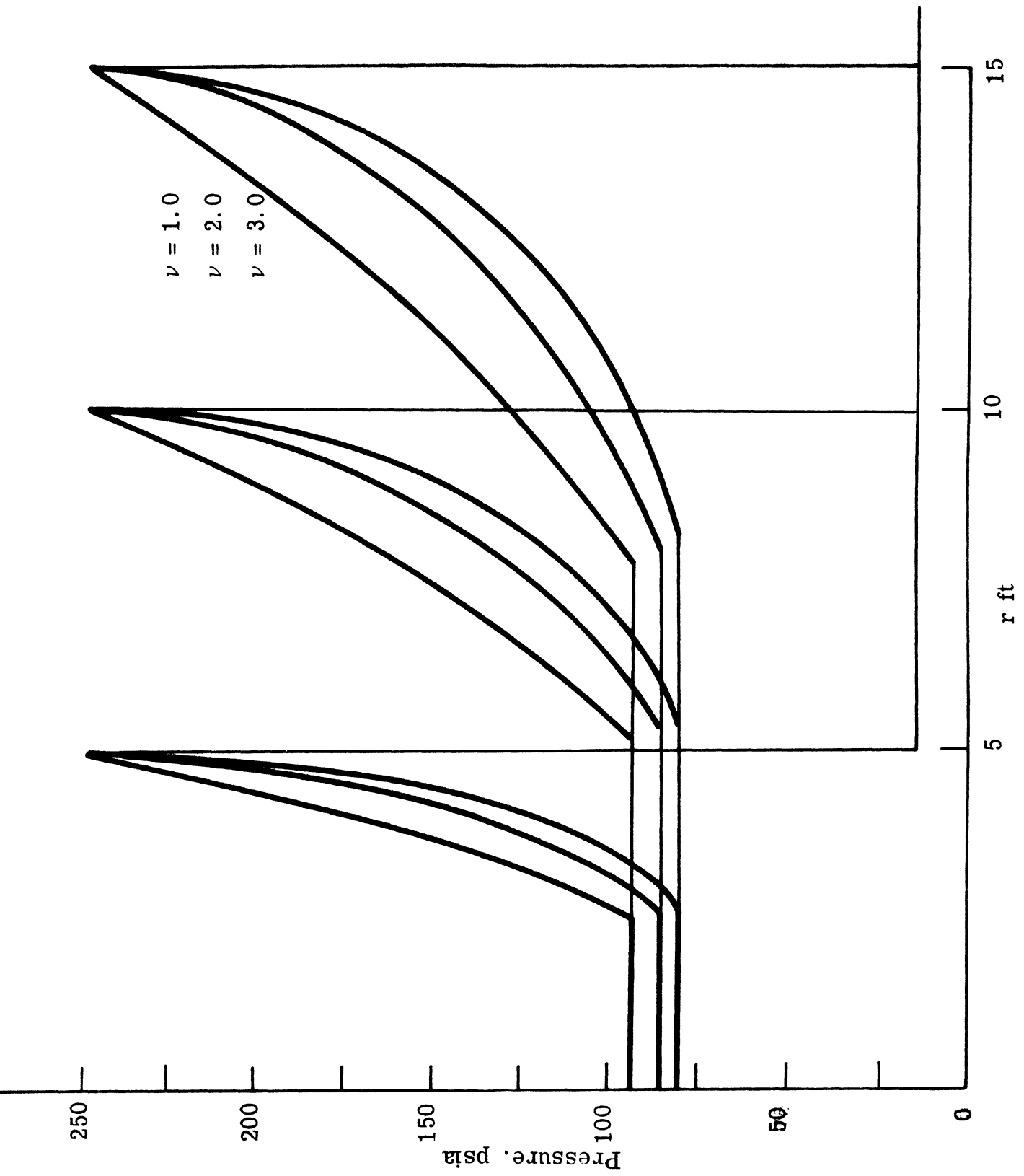
Figure II-2. Air-CH_4 C-J Detonation Variation of Pressure.
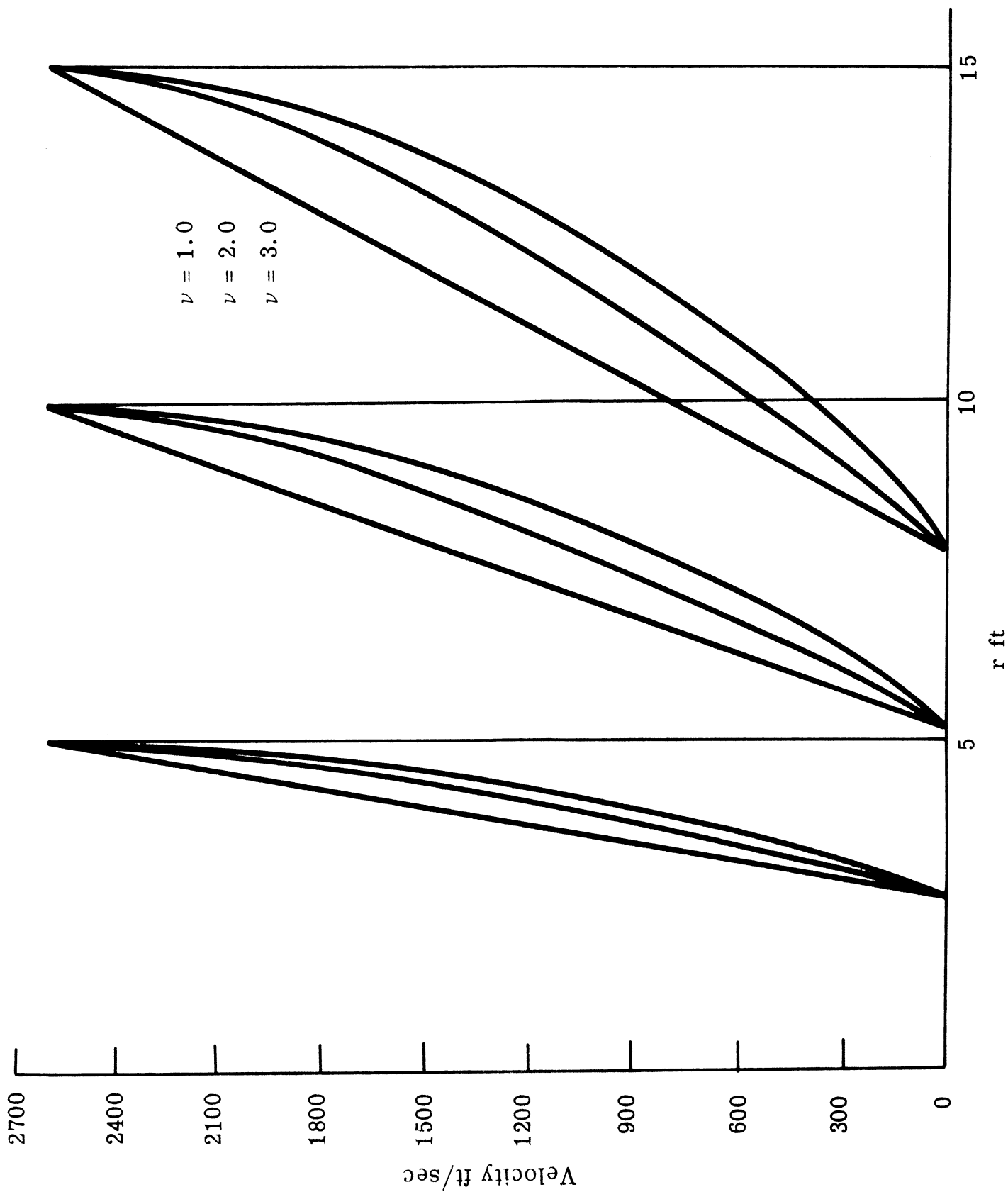
Figure II-3. Air-CH$_4$ C-J Detonation, Variation of Velocity
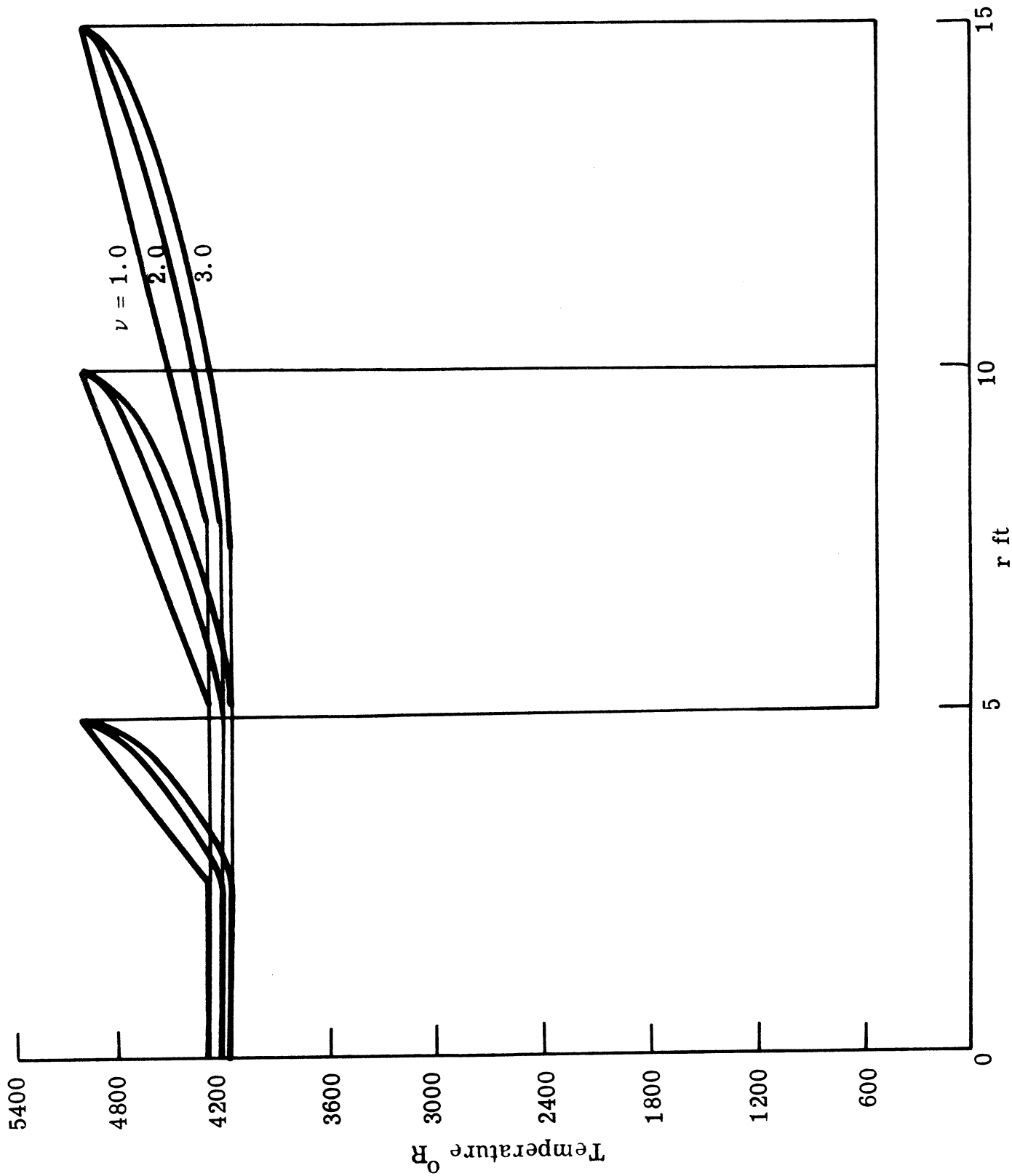
Figure II-4. Air-CH$_4$ C-J Detonation Variation of Temperature

As indicated in the main body of this report, for MAPP, air and methane-air detonations the variations of γ_2, γ_1 and z_1 are sufficiently small that $\delta(\gamma_2, \nu)$ essentially depends only on the geometric factor ν.

APPENDIX III

CALCULATIONS OF CHEMICAL EQUILIBRIUM IN CHAPMAN-JOUGUET CONDITIONS

The calculation of chemical equilibrium is the essential feature of the Gordon McBride Program (6). This calculation is carried out by iteratively minimizing the Gibbs or Helmholtz free energy as described in detail in Ref. 6. The program computes the equilibrium composition of gas mixtures with each component satisfying the perfect gas equation.

With the equilibrium calculation as a base the program can carry out the following calculations:

(1) Chemical equilibrium for assigned states $(T, P), (H, P), (S, P)$, $(T, V), (U, V)$ or (S, V).

(2) Theoretical rocket performance for both equilibrium and frozen compositions during expansion.

(3) Incident and reflected shock properties.

(4) Chapman-Jouguet detonation properties.

Condensed species as well as gaseous species can be considered.

The program includes thermodynamic data for 62 reactants and 421 reaction species in the form of coefficients for polynomials fit to the data by the method of least squares. The data is taken mainly from the JANAF tables (JANAF Thermochemical Tables. Dow Chemical Co., Midland, Mich., Dec. 31, 1960 to June 30, 1970. Also Ser. A, June 1963; Ser. B, Jan. 1964; Ser. C, April 1965; Ser. D, Mar. 1966; Ser. E, Jan. 1967.)

The program input specifies the oxidizer and fuel composition enthalpy and density in the case of the C-J option. Certain code words specifying which option is to be used must also be specified.

The output tabulates the properties of the burned and unburned gas and the detonation parameters p_2/p_1, T_2/T_1, m_2/m_1, ρ_2/ρ_1, and detonation velocity C. The program also provides the final equilibrium composition and a list of the products considered in the calculation.

A typical input and output for the calculation of the properties of a methane-air detonation is reproduced below. Detailed instructions for use of the program and sample inputs and outputs are presented in Ref. 6.

DETONATION PROPERTIES OF AN IDEAL REACTING GAS

CASE NO. 1

CHEMICAL FORMULA	WT FRACTION (SEE NOTE)	ENERGY CAL/MOL	STATE	TEMP DEG K	DENSITY G/CC
OXIDANT O 2.00000	0.23144	0.0	G	298.15	0.0
OXIDANT N 2.00000	0.75524	0.0	G	298.15	0.0
OXIDANT AR 1.00000	0.01286	0.0	G	298.15	0.0
OXIDANT C 1.00000 O 2.00000	0.00046	-94046.313	G	298.15	0.0
FUEL C 1.00000 H 4.00000	1.00000	-17895.828	G	298.15	0.0

O/F= 39.6795   PERCENT FUEL= 2.4582   EQUIVALENCE RATIO= 0.4352   REACTANT DENSITY= 0.0

UNBURNED GAS
P1,ATM   1.0000
T1,DEG K   298.15
H1,CAL/G   -28.38
M1,MOL WT   28.402

BURNED GAS
P, ATM   10.624
T, DEG K   1847
RHO, G/CC   1.9912-3
H, CAL/G   130.5
S, CAL/(G)(K) 2.0331

M, MOL WT   28.399
(DLV/DLP)T   -1.00004
(DLV/DLT)P   1.0013
CP, CAL/(G)(K)   0.3332
GAMMA (S)   1.2667
SON VEL,M/SEC   827.6

DETONATION PARAMETERS
P/P1   10.624
T/T1   6.194
M/M1   0.9999
RHO/RHO1   1.7151
DET VEL,M/SEC 1419.4

MOLE FRACTIONS
AR   0.00892
CO   0.00001
CO2   0.04379
H2   0.00001
H2O   0.08683
NO   0.00366
NO2   0.00002
N2   0.74498
O   0.00002
OH   0.00039
O2   0.11138

ADDITIONAL PRODUCTS WHICH WERE CONSIDERED BUT WHOSE MOLE FRACTIONS WERE LESS THAN 0.50000E-05 FOR ALL ASSIGNED CONDITIONS

C(S)	C	CH	CH2	CH2O	CH3	CH4	CN	CNN	CN2
C2	C2H	C2H2	C2H4	C2N	C2N2	C20	C3	C3O2	C4
C5	H	HCN	HCO	HNCO	HNO	HO2	H2O(S)	H2O(L)	H2O2
N	NCO	NH	NH2	NH3	N2H4	N20	N2O	N2O4	N3

NOTE. WEIGHT FRACTION OF FUEL IN TOTAL FUELS AND OF OXIDANT IN TOTAL OXIDANTS

137

```
REACTANTS
O    2.0000    0.0    0.0    0.0    0.0    0.231440    0.0    298.150  G   0.0    0.0
N    2.0000    0.0    0.0    0.0    0.0    0.752240    0.0    298.150  G   0.0    0.0
AR   1.0000    0.0    0.0    0.0    0.0    0.012860    0.0    298.150  G   0.0    0.0
O    1.0000    O    2.0000    0.0    0.0    0.000460    0.0    298.150  G   0.0    0.0
C    1.0000    H    4.0000    0.0    0.0    1.000000   -17895.00   298.150  G   0.0    0.0

NAMELISTS
&INPT2
KASE=        1,T= 0.0
   0.0          0.0    0.0    ,    0.0    ,    0.0    ,    0.0
   0.0          0.0    0.0    ,    0.0    ,    0.0    ,    0.0
   0.0          0.0    0.0    ,    0.0    ,    0.0    ,    0.0    ,PSIA
   0.0          0.0    0.0    ,    0.0    ,    0.0    ,    0.0
   0.0          0.0    0.0    ,    0.0    ,    0.0    ,KHO= 1.000000
   0.0          0.0    0.0    ,    0.0    ,    0.0    ,    0.0    ,    0.0
&END                   ,ERATIO=T,OF=F,FPCT=F,FA=F,MIX= 0.4351599b
              ,TP=F,HP=F,SP=F,TV=F,UV=F,SV=F,RKT=F,SHOCK=F,DETN=T,CTIO=F,CR= 0.0

SPECIES BEING CONSIDERED IN THIS SYSTEM
 J 6/66  AR        J 3/61  C(S)       J 3/61  C          J12/67  CH        J 6/69  CH2
 J 3/61  CH2O      J 6/69  CH3        J 3/61  CH4        J 6/69  CN        J 6/66  CNN
 J12/70  CN2       J 9/65  CO         J 9/65  CO2        J12/69  C2        J 3/67  C2H
 J 3/61  C2H2      J 9/65  C2H4       J 3/67  C2N        J 3/61  C2N2      J 9/66  C2O
 J12/69  C3        J 6/68  C3O2       J12/69  C4         J12/69  C5        J 9/65  H
 L12/69  HCN       J12/70  HCO        J12/70  HNCO       J 3/63  HNO       J 3/64  HO2
 L 3/61  H2        L11/65  H2O(S)     L11/65  H2O(L)     J 3/61  H2O       L 2/69  H2O2
 J 3/61  N         J12/70  NCO        J12/65  NH         J12/65  NH2       J 9/65  NH3
 J 6/63  NO        J 9/64  NO2        J 9/65  N2         J 6/02  O         J12/64  N2O
 J 9/64  N2O4      J12/70  N3                                                J 9/65  O2

OF =   39.679459

ENTHALPY                    EFFECTIVE FUEL       EFFECTIVE OXIDANT           MIXTURE
(KG-MOL)(DEG K)/KG            HPP(2)               HPP(1)                    HSUBO
                           -0.56134766E 03      -0.49467951E 00         -0.14281811E 02

KG-ATOMS/KG                  BOP(I,2)              BOP(I,1)                  BO(I)
 O           0.0            0.0                  0.14486443E-01           0.14130328E-01
 N           0.0            0.0                  0.53919919E-01           0.52594431E-01
 AR          0.0            0.0                  0.32151840E-03           0.31400472E-03
 C           0.62332422E-01 0.10452182E-04       0.15424767E-02
 H           0.24932969E 00 0.0                  0.61291270E-02
```

REFERENCES

1. Nicholls, J. A. , Fry, R. S. , Glass, D. R. , Sichel, M. , VanderSchaff, J. , Sternstein, A. J. , "Fundamental Aspects of Unconfined Explosions," Technical Report, AFATL-TR-72-49, March 1972.

2. Korobeinikov, V. P. , "The Problem of Point Explosion in a Detonating Gas," Astronautica Acta, 14, 1969, p. 411.

3. Bach, G. G. , Knystautas, R. , Lee, J. H. , "Initiation Criteria for Diverging Gaseous Detonations," Thirteenth Symposium (International) on Combustion, The Combustion Institute, 1971, p. 1097.

4. Sedov, L. I. , Similarity and Dimensional Methods in Mechanics, 4th ed. , Academic Press, New York, 1959.

5. Taylor, G. I. , "The Formation of a Blast Wave by a Very Intense Explosion," Proc. Roy. Soc. , A201, p. 159,175, 1950.

6. Gordon, S. and McBride, B. , "Computer Program for Calculation of Complex Chemical Equilibrium Compositions, Rocket Performance, Incident and Reflected Shocks, and Chapman-Jouguet Detonations," NASA SP 273, 1971.

7. Brode, H. L. , Glass, I. I. , and Oppenheim, A. K. , "Gas Dynamics of Explosions Today," Shock Tube Research, Proc. of the Eighth International Shock Tube Symposium, Imperial College, London, 5-8 July 1971. Stollery, J. L. , Gaydon, A. D. , and Owen, P. R. , editors.

8. Kiwan, A. R. , "Gas Flow During and After the Deflagration of a Spherical Cloud of Fuel-Air Mixture," BRL Report No. 1511, (U. S. Army), 1970.

9. Burgess, D. C. , Murphy, J. N. , Hanna, N. E. , and Dolah, R. W. , "Large-Scale Studies of Gas Detonations," Bureau of Mines Report of Investigations 7196 (1968).

10. Benedick, W. B. , Kennedy, J. D. , and Morosin, B. , "Detonation Limits of Unconfined Hydrocarbon-Air Mixtures," Combustion and Flame, 15, 83 (1970).

11. Collins, D. M. , "Critical Energy Threshold for Detonation Initiation in MAPP-Air Mixtures," AFATL-TR-72-192 (1972).

12. Huston, R. F., Barrios, C. A., and Hulleman, R. A., "Weathering and Stability of Methylacetylene-Propadiene-Hydrocarbon Mixtures," J. Chem. and Engr. Data, Vol. 15, No. 1, 1970.

13. Kuchta, J. M., Spolan, J., Zabetakis, M. G., J. Chem. Engr. Data, Vol. 9, 1964, p. 467.

14. Yoshimine, M., Kern, W. G., Belfit, R. W., Jr., J. Chem. Engr. Data, Vol. 12, 1967, p. 399.

AFSC (DLW)	2
AFSC (SDWM)	1
AFSC (IGFG)	1
AFSC/DPSL Tech Lib	1
Hq USAF/SAMI	1
Hq USAF/XOOWB	1
Hq USAF/XOOW	2
Hq USAF/RDPA	1
ASD/ENYS-Mr. Hartley	1
FTD/PDYF	1
AFOSR/NAE	1
Air University (AUL/LSE-70-239)	1
USNWC/Code 4563	1
USNWC/Code 456	2
Picatinny Ars/SMUPA-ET/Dr. Slagg	1
Picatinny Ars/SMUPA-aD-D-W-7, Mr. C. J. Kobialka	1
Picatinny Ars/SMUPA-FR-E, Dr. R. F. Walker	2
DDC	2
Sandia Lab (ATTN: R.P.Stromberg)	1
Univ of Mich (ATTN:Prof.Nicholls)	20
Univ of Cincinnati (ATTN: Prof. Kauffman)	1
Univ of Illinois (ATTN: Prof. Strehlow)	1
AFWL/Mr. R. Bunker)	1
USN Wpns Lab/GWW (A.R.Hales)	1
Ball Rsch Lab/Dr. Kiwan	1
Univ of Calif/Prof. Oppenheim	1
IIT Rsch Institute	1
USA Ball Rsch Lab/Dr. Freedman	1
USA Ball Rsch Lab/Mr. C. Kingery	1
Stanford Rsch Inst/Dr.Cowperthwaite	1
Univ of Conn/Prof.E.K.Dabora	1
McGill Univ/Dr.John Lee	1
TRADOC/ADTC/DO	1
AFATL/DL	1
AFATL/DLOSL	3
AFATL/DLI	1
AFATL/DLIF	5
AFATL/DLR/Mr. Strickland	1

(The reverse of this page is blank.)

DOCUMENT CONTROL DATA - R & D

(Security classification of title, body of abstract and indexing annotation must be entered when the overall report is classified)

1. ORIGINATING ACTIVITY *(Corporate author)*	2a. REPORT SECURITY CLASSIFICATION
The University of Michigan, Aerospace Engr. Dept., Gas Dynamics Laboratories, Ann Arbor, Mich. 48105	Unclassified
	2b. GROUP

3. REPORT TITLE

FUNDAMENTAL ASPECTS OF UNCONFINED EXPLOSIONS

4. DESCRIPTIVE NOTES *(Type of report and inclusive dates)*

Final Report - January 22, 1972 to January 21, 1973

5. AUTHOR(S) *(First name, middle initial, last name)*

J. A. Nicholls   C. Hu   K. Kearney
M. Sichel   D. R. Glass
R. S. Fry   R. De Saro

6. REPORT DATE	7a. TOTAL NO. OF PAGES	7b. NO. OF REFS
June 1973	154	14

8a. CONTRACT OR GRANT NO	9a. ORIGINATOR'S REPORT NUMBER(S)
F08635-71-C-0083	
b. PROJECT NO 2513	
c. Task No. 07	9b. OTHER REPORT NO(S) *(Any other numbers that may be assigned this report)*
d. Work Unit No. 001	AFATL-TR-73-125

10. DISTRIBUTION STATEMENT

Distribution limited to U.S. Government agencies only; this report documents test and evaluation; distribution limitation applied June 1973. Other requests for this document must be referred to the Air Force Armament Laboratory (DLIF), Eglin AFB, Fla. 32542

11. SUPPLEMENTARY NOTES	12. SPONSORING MILITARY ACTIVITY
Available in DDC	Air Force Armament Laboratory Air Force Systems Command Eglin Air Force Base, Florida 32542

13. ABSTRACT

This report covers progress made in the second year of the research program. The first part of the report is devoted to a generalized analytical prediction of the ground impulse that can be obtained from a blast wave, detonation wave, and an idealized fuel-air explosion. The latter consists of blast wave behavior for radius, r, less than a critical radius, r^*, and Chapman-Jouguet detonation for $r > r^*$. In all cases so far, the finite diameter of the cloud with the attendant shock wave propagation beyond the cloud has not been taken into account. The latter part of this report is devoted to the experimental aspects. Improvements in the facility for generating cylindrical shock waves and detonation waves are described. Controlled experiments on cylindrical blast waves with the associated data reduction techniques are discussed. The results are interpreted to yield a calibration on the effective energy release of the initiating charge of Detasheet. Two phase cylindrical detonation experiments were also conducted using a highly refined fraction of kerosene. The results indicate that at small radius blast wave behavior predominated whereas at larger radius a constant velocity detonation was realized when the initiation energy was sufficiently high. The experimentally determined transition radius between the two types of behavior agreed very well with theoretical values. Cylindrical detonations in gaseous MAPP-air mixtures were also studied. The variation in threshold energy required for initiation as well as rich and lean limits were established. The results agree very well with large scale field tests.

DD FORM 1473 (1 NOV 65)

14. KEY WORDS	LINK A		LINK B		LINK C	
	ROLE	WT	ROLE	WT	ROLE	
Unconfined explosions						
Chapman-Jouguet detonations						
Hydrocarbon fuels						
Detonation velocity						
Two-phase detonation						
Condensed explosive (Detasheet)						
Detonation propagation						